## AQRP Project 22-023

# Source-sector NOx emissions analysis with sub-kilometer scale airborne observations in Houston during TRACER-AQ

## Final Report

Prepared for:

Elena McDonald-Buller
Project Manager
Texas Air Quality Research Program

Prepared by:

Daniel Goldberg, M. Omar Nawaz
George Washington University
Washington, DC

Jeremiah Johnson, Greg Yarwood
Ramboll
Novato, California

Laura Judd
NASA Langley
Hampton, Virginia

Benjamin de Foy
Saint Louis University

August 31, 2023

# Contents

**Tables**



**Figures**

## ACKNOWLEDGEMENT

The preparation of this report (Project No. 22-023) was funded by a grant from the Texas Air Quality Research Program (AQRP) at The University of Texas at Austin through the Texas Emission Reduction Program (TERP) and the Texas Commission on Environmental Quality (TCEQ). The findings, opinions and conclusions are the work of the authors and do not necessarily represent findings, opinions, or conclusions of the AQRP or the TCEQ.

## LIST OF ACRONYMS AND ABBREVIATIONS

| | |
|---|---|
| AMPD | Air Markets Program Data |
| AQRP | Air Quality Research Program |
| CAMPD | Clean Air Markets Program Division |
| CAMS | Continuous Air Monitoring Station |
| CAMx | Comprehensive Air quality Model with extensions |
| CEMs | Continuous Emissions Monitoring systems |
| CST | Central Standard Time |
| DFW | Dallas – Fort Worth |
| ECMWF | European Centre for Medium-Range Weather Forecasts |
| EGU | Electric Generating Unit |
| EMG | Exponentially Modified Gaussian |
| EPA | Environmental Protection Agency |
| ERA5 | 5$^{th}$ generation ECMWF atmospheric reanalysis |
| ESA | European Space Agency |
| FD | Flux divergence |
| FINN | Fire INventory from NCAR |
| GCAS | GEO-CAPE Airborne Simulator |
| GDAS | GFS Data Assimilation System |
| GEOS-CF | Goddard Earth Observing System Composition Forecasting model |
| GFS | Global Forecasting System |
| G-V | Gulfstream Five aircraft |
| HCHO | Formaldehyde |
| HGB | Houston-Galveston-Brazoria Area |
| $HNO_3$ | Nitric acid |
| KHOU | Houston William P. Hobby airport |
| KIAH | Houston George Bush Intercontinental airport |
| km | kilometer |
| $LNO_X$ | Lightning NOx emissions |
| LSM | Land Surface Model |
| m | meter |
| MARINER | MARINe Emissions Resolver |
| mb | millibars |
| MB | Mean Bias |
| MDA8 | maximum daily average over 8-hours |
| ME | Mean Error |
| MEGAN | Model of Emissions of Gases and Aerosols from Nature |
| MINDS | Multi-Decadal Nitrogen Dioxide and Derived Products from Satellites |
| MLR | Multi-Linear Regression |
| MODIS | Moderate Resolution Imaging Spectroradiometer (satellite) |
| MOVES | EPA MOtor Vehicle Emissions Simulator |
| NAAQS | National Ambient Air Quality Standard |
| NASA | National Aeronautics and Space Administration |

| | |
|---|---|
| NCAR | National Center for Atmospheric Research |
| NMB | Normalized Mean Bias |
| NME | Normalized Mean Error |
| $NO_2$ | Nitrogen Dioxide |
| NOAA | National Oceanic and Atmospheric Administration |
| NOx | Oxides of Nitrogen |
| NRTEEM | Near-Real Time Exceptional Event Modeling |
| OMI | Ozone Monitoring Instrument (satellite) |
| PAN | Peroxyacyl nitrates |
| Pandora | Pandora Spectrometer System |
| PBL | Planetary Boundary Layer |
| ppb | parts per billion |
| RFP | Reasonable Further Progress |
| SAT | Source apportionment technology |
| SIP | State Implementation Plan (for the ozone NAAQS) |
| $SO_2$ | Sulfur dioxide |
| TEMPO | Tropospheric Emissions: Monitoring of POllution (satellite) |
| TexAER | Texas Air Emissions Repository |
| TexN | Texas NONROAD |
| TCEQ | Texas Commission on Environmental Quality |
| tpd | tons per day |
| TRACER-AQ | Tracking Aerosol Convection ExpeRiment – Air Quality |
| TROPOMI | Tropospheric Monitoring Instrument (satellite) |
| US | United States |
| VIIRS | Visible Infrared Imager-Radiometer Suite (satellite) |
| VOC | Volatile Organic Compound |
| VCD | Vertical Column Density |
| VMT | Vehicle Miles Traveled |
| WRF | Weather Research and Forecast model |

## EXECUTIVE SUMMARY

In this project we used column nitrogen dioxide ($NO_2$) information from the Geostationary Coastal and air pollution events Airborne Simulator (GCAS) instrument (250 × 560 $m^2$) (Janz et al., 2019; Nowlan et al., 2018), available during the September 2021 NASA/TCEQ Tracking Aerosol Convection ExpeRiment – Air Quality (TRACER-AQ) field campaign and the Tropospheric Monitoring Instrument (TROPOMI), to better understand the fine-scale structure of $NO_X$ emissions in the Houston metropolitan area including a sector-by-sector analysis.

Complementing the remote sensing observations, the Comprehensive Air Quality Model with Extensions (CAMx) was run with a fine spatial resolution (444 × 444 $m^2$) using the 2019 TCEQ emissions inventory. The model output was thoroughly compared to observations from the GCAS instrument, the Pandora instruments, and TROPOMI in order to identify gaps in our understanding of $NO_X$ emissions and $NO_2$ dispersion within CAMx.

This work mapped to four Research Priority Areas of the Texas Air Quality Research Program (AQRP), as shown in the table below.

**Table 1. How this project will respond to the AQRP Research Priority Areas**

| Research Priority Area | How this project addressed the Research Priority |
|---|---|
| Utilize TRACER-AQ and over-water measurements | The GCAS and Pandora measurements acquired during TRACER-AQ were used extensively in this project to infer sectorized $NO_X$ emissions addressing TRACER-AQ science objectives on Ozone Photochemistry and Model Evaluation |
| Improve emissions inventories | Satellite and aircraft measurements, aided by machine learning, were used to directly estimate instantaneous $NO_X$ emission rates, often from individual point sources or sectors of sources. |
| Improve accuracy of photochemical grid models | Model (CAMx) was tested against the GCAS and Pandora observations to identify where improvement is needed in $NO_X$ emissions by sector, therefore improving model performance. |
| Use of satellite and other remote sensing data | Utilized aircraft (GCAS) and satellite (TROPOMI) to better understand spatial patterns of $NO_2$ and its relationship to $NO_X$ emissions |

The primary objective of this work was to better understand the sector-by-sector $NO_X$ emissions in the Houston metropolitan area during September 2021 using a combination of chemical transport models, aircraft observations, ground measurements, and satellite datasets. The broader implications of this study were to achieve a better understanding of the spatial and temporal patterns of ozone precursor emissions. Lessons learned and techniques developed for this project could be applied to other areas within Texas and potentially other areas in the United States when data from the Tropospheric Emissions Monitoring of Pollution satellite (TEMPO) become available. The project also demonstrated the capability to: 1) estimate $NO_X$ emissions using the GCAS and 2) quantify sectorized $NO_X$ emissions from certain sources (non-CEMS point sources, airports, railyards, and commercial marine) that are difficult to constrain using typical "bottom-up" methodologies.

This project had six tasks to accomplish the primary objective of better understanding the fine-scale structure of Houston $NO_X$ emissions. Results from these six tasks will be summarized with brevity here and in more detail in Section 2.

**Task 1. Simulate $NO_2$, HCHO, $O_3$ at 444 × 444 $m^2$ spatial resolution using WRF-CAMx**

For this project, the WRF and CAMx models were run at 444 x 444 $m^2$ spatial resolution for September 1-11 and 22-27, 2021 which corresponded to GCAS flights during the TRACER-AQ field campaign. The 444 x 444 $m^2$ domain was nested inside 36/12/4/1.333 km modeling domains.

The near-surface CAMx model performance for MDA8 ozone was a NMB of –2.5%, a NME of 15.0%, and a mean bias of –1.3 ppb. The top decile of observed ozone values was consistently underestimated by the model, and the lowest decile of observed ozone values was consistently overestimated by the model.

Performance against the $NO_2$ CAMS monitors was notably worse. The near-surface model performance for $NO_2$ was a NMB of –59.1%, a NME of 62.3%, and a mean bias of –5.0 ppb. A portion of the disagreement could be due to a known positive interference of PAN and $HNO_3$ in chemiluminescence $NO_2$ monitors. In Task 5, modeled column $NO_2$ are evaluated in comparison to GCAS aircraft measurements, TROPOMI satellite measurements, and Pandora surface-based column measurements.

**Task 2. Process the GCAS measurements**

GCAS measurements were acquired from the NASA G-V aircraft from an altitude of 28,000 ft, with an on-ground pixel size of approximately 560 x 250 $m^2$. There were 12 flights days during TRACER-AQ and 10 of them were utilized in this project. Skies were mostly clear during the flight days – a summary of the daily meteorology is in Table 2.2.1 – and all measurements with cloud interference were screened out.

Originally, when using $NO_2$ vertical profile information from a 0.25° x 0.25° model to process the GCAS measurements, there was strong correlation of total column $NO_2$ ($r^2$ = 0.80) and a small NMB (+6.3%) in comparison to the Pandora instruments – which uses a similar measurement technique but is otherwise a completely independent instrument – deployed during TRACER-AQ. When using $NO_2$ vertical profile information from the 444 x 444 $m^2$ CAMx simulation developed in this project, the correlation and NMB further improved ($r^2$ = 0.81 and NMB of +3.2%).

**Task 3. Process the satellite $NO_2$ data**

Measurements of total and tropospheric vertical column $NO_2$ are available from TROPOMI daily between 1:30 – 3 PM over the Houston metropolitan area. Daily snapshots of tropospheric column $NO_2$ during September 2021 can be seen in Figure 2.3.1. When comparing the operational TROPOMI total column measurements to Pandora, correlation was $r^2 = 0.62$ and there was a small low NMB of –11.7%.

Similar to GCAS, $NO_2$ vertical profile information is needed to process the TROPOMI satellite data. Inclusion of $NO_2$ vertical profile information from CAMx increased the maximum observed values by +11% and decreased the mean value in the Houston domain by –8% (Figure 2.3.2). The correlation and NMB at the Pandora locations only modestly improved when the CAMx $NO_2$ vertical information was included, $r^2 = 0.62$ and NMB of –11.2%, despite larger changes elsewhere in domain as discussed above.

**Task 4. Calculating $NO_X$ from $NO_2$ airshed measurements**

In this project, two statistical-based methods were employed to infer $NO_X$ emissions from the GCAS measurements. The first method utilized an exponentially modified Gaussian (EMG) fit and was used exclusively for point source emissions. The second method utilized the flux divergence (FD) and has suitability for a wider range of sources while needing additional assumptions to derive $NO_X$ emissions rates.

The EMG method was successful in three areas with point sources: W. A. Parish power plant, Baytown, and Channelview. For the GCAS $NO_2$ measurements over the Parish power plant on September 24, 2021, we were able to calculate $NO_X$ emissions that matched the CAMPD reported $NO_X$ emissions to within 10%. When the method was then applied to the Baytown area on September 8, 2021, there appeared to be a 43% $NO_X$ underestimate in the inventory, which is at the cusp of the uncertainty in the method. There was better agreement between inventory and GCAS measurements in the Channelview area during a September 9, 2021 overpass.

The FD method was then able to evaluate the $NO_X$ emissions inventory over a wider spatial domain. The FD method was able to distinguish the linear shape of major highways, many of the large point sources, and the Galveston Bay ship track. When the method was applied to both the GCAS measurements and CAMx simulation independently, there were large discrepancies near the major highways – GCAS measurements were often much larger than CAMx in areas with high vehicle densities. There was generally good agreement near the point sources of the Ship Channel, and a potential inventory overestimate of $NO_X$ emission from marine vessels.

**Task 5. Comparison of $NO_2$ and HCHO between model, aircraft, and satellite**

When column $NO_2$ from the CAMx simulation were compared to Pandora measurements, we found low correlation ($r^2$ = 0.25) and a NMB of –20.2%. The relatively low correlation could be related to the difficulty in simulating wind direction and the Gulf/Bay breeze. We found a larger NMB between CAMx and Pandora on weekdays (–26.1%) than weekends (–5.8%), but better correlation on weekdays ($r^2$ = 0.29) than weekends ($r^2$ = 0.21).

When column $NO_2$ from the CAMx simulation were compared to the GCAS measurements, the NMB was larger (–37.0%) than the NMB of the CAMx vs. Pandora intercomparison, but the correlation between CAMx and GCAS was very strong ($r^2$ = 0.75). We find the largest difference between CAMx and GCAS to be in the downtown section of Houston (Figure 2.5.5)

*A culmination of the $NO_2$ intercomparison implicates a missing weekday source in the $NO_X$ emission inventory that is primarily collocated with highways, road density, and/or population density.*

When column HCHO from the CAMx simulation were compared to the GCAS and TROPOMI measurements, there seemed to be a low bias in the CAMx simulation. It is too early to know whether to implicate missing biogenic or anthropogenic VOCs in the simulation as the culprit for the disagreement.

**Task 6. Use of machine learning to estimate emission factors for individual sectors**

In the final task of this project, a multiple linear regression (MLR) model was used synergistically with simulated column $NO_2$ source apportionment information from CAMx and from the GCAS measurements to diagnose which $NO_X$ emission inventory sectors could have biases.

The results show that on-road, railyard, and KIAH airport $NO_X$ emissions may be underestimated in the CAMx simulation. In contrast, shipping $NO_X$ emissions may have a small overestimate. After the scaling factors were applied to account for these suspected biases, the MLR model replicated the GCAS measurements with no bias.

# 1.0 INTRODUCTION

This document provides the final report for the Texas Air Quality Research Program (AQRP) Project 22-023, "Source-sector NOx emissions analysis with sub-kilometer scale airborne observations in Houston during TRACER-AQ". The goal of Project 22-023 was to better understand the sector-by-sector $NO_X$ emissions in the Houston metropolitan area using a combination of chemical transport models, machine learning models, aircraft observations, ground measurements, and satellite datasets.

The project Principal Investigator is Dr. Daniel Goldberg (George Washington University) with co-Principal Investigator Mr. Jeremiah Johnson (Ramboll). Other personnel on the project team were: Dr. Laura Judd (NASA Langley), Dr. Greg Yarwood (Ramboll), Dr. Benjamin de Foy (Saint Louis University), and Dr. M. Omar Nawaz (George Washington University). The AQRP project manager is Dr. Elena McDonald-Buller at the University of Texas, Austin. The project liaison for the Texas Commission on Environmental Quality (TCEQ) is Sushil Gautam.

## 1.1 Background

While fossil fuel consumption is known on a national basis with a high-degree of certainty, the spatial and temporal patterns of its combustion have less certainty (McDonald et al., 2012, 2013). The location and timing of the combustion emissions can substantially affect air quality; emissions in a rural area are not the same as emissions in an urban area due to the ambient environmental conditions and the higher probability of human exposure in urban settings.

Typically, air pollutant emission rates for chemical species such as nitrogen oxides ($NO_X$) are estimated using a "bottom-up" approach, which uses fuel consumption information, spatial surrogates (e.g., road density, population density, locations of known stack emissions), temporal surrogates (e.g., traffic patterns, industrial work schedules) and emission factors (mass of pollutant per mass of fuel burned) to estimate the spatiotemporal patterns of emissions across regions. With investments in technology to better understand the spatiotemporal patterns of pollutants (e.g., incorporating real-time traffic data using speed and type of vehicle) and laboratory studies to better estimate the emission factors in a wide range of conditions, these "bottom-up" estimates can be improved. These new and improved estimates can then be incorporated into a chemical transport model and evaluated against observations from satellite data and the ground monitoring network acquiring concentrations. Based on this comparison, the emission estimates can be further adjusted and improved if necessary. However, because of the complexity of this cycle, "bottom-up" emission estimates typically take many years to compile by a large team of scientists, and subsequently, are delayed in time by several years from the actual emission time.

A complementary approach to estimate air pollutant emissions is in using a "top-down" approach. With this method, emissions are back-calculated from pollutant measurements acquired across an entire airshed. This is typically done with a remote sensing instrument – in orbit ((Goldberg et al., 2019b) or on an aircraft (Kuhlmann et al., 2022; Meier et al., 2017; Souri et al., 2018). The emission rates are inferred by analyzing the concentration maps over a large

region and incorporating the lifetime (chemical and dispersion lifetime) of the pollutant to back-calculate the emission rate at the source. The advantage of this technique is that it is completely independent of the complex datasets needed to estimate "bottom-up" emissions rates. Further, while setting the foundation to do a "top-down" emission analysis can take some time (months/years), once the foundation is in-place, it is feasible that near-real-time emission rates could be derived within hours of the remote sensing measurement (Goldberg, Lu, Streets, et al., 2019).

Prior work by scientists on this team, sponsored by AQRP (Holloway et al., 2021), demonstrated the capability to estimate $NO_X$ emissions for the Dallas – Fort Worth metropolitan region for the summer of 2019 using a "top-down" approach and the Tropospheric Monitoring Instrument (TROPOMI). The team has also conducted similar analyses for other North American cities (Goldberg, Lu, Oda, et al., 2019; Goldberg, Lu, Streets, et al., 2019), power plants (Benjamin de Foy et al., 2015), South Asia (Benjamin de Foy & Schauer, 2022), and global megacities (Goldberg et al., 2021) using TROPOMI and a complementary satellite instrument, the Ozone Monitoring Instrument (OMI). The team is also already funded to estimate near-real-time $NO_X$ emissions using TROPOMI for several North American cities as part of a NASA Health and Air Quality Science Team (HAQAST) project grant. "Top-down" emission estimates can be helpful, especially in areas with very uncertain emission inventories such as Africa or the Middle East. Typically, these aggregated "top-down" estimates agree with the "bottom-up" estimates within 20% in North American cities (well within the uncertainty associated with the 'top-down' method) (Goldberg et al., 2021). However, due to TROPOMI's spatial resolution ($3.5 \times 5.5$ km$^2$ at nadir) and temporal resolution (once daily), TROPOMI is most often used to calculate total emissions aggregated over the entire metropolitan area. Therefore, very limited, if any, sector-by-sector resolved information can be gleaned from an analysis using currently available satellite datasets.

## 1.2 Overview of Approach

The primary objective of this work is to support regional evaluation of emissions inventories with remote sensing data. However, emissions are not directly comparable with the column abundance detected by remote sensing instruments without further manipulation, as outlined above. And further, with the launch of TROPOMI (in 2017) and fine-scale measurements from GCAS (2021), more fine-scale information is available to the research community to evaluate $NO_X$ and $NO_2$ within urban areas.

## 1.3 Overview of Report

In Section 2, we provide a comprehensive overview of the results of all six tasks of this project including CAMx simulations, GCAS and satellite data processing, data comparisons, and results on emissions analysis. In Section 3, we present conclusions and recommendations for future work.

# 2.0 TASK RESULTS

## 2.1 Simulate $NO_2$, HCHO, $O_3$ at 444 × 444 $m^2$ spatial resolution using WRF-CAMx

We ran the WRF and CAMx models for September 2021 which corresponded to the TRACER-AQ timeframe. Ramboll developed a new high-resolution WRF and CAMx modeling platform for this study. The WRF model configuration is similar to that used for the TCEQ SIP modeling, while the CAMx model is updated to incorporate emissions changes. We provide a model performance evaluation against surface monitors at the end of this section.

### 2.1.1 Model Configuration

#### 2.1.1.1 WRF Model

The WRF model is a mesoscale numerical weather prediction system designed to serve both operational forecasting and atmospheric research needs (Skamarock et al., 2005, 2008). We used version 4.3.3 of the Advanced Research WRF (ARW) in this study (Skamarock et al., 2021).

We define the WRF 36/12/4/1.333/0.444-km modeling domains as slightly larger than the corresponding CAMx domains (Figure 2.1.1) to avoid possible numerical artifacts near domain boundaries in WRF transferring to CAMx. The 36 km CAMx domain (red) includes all of the continental US, Mexico and large areas of Central America and Canada. The 36 km, 12 km (blue) and East Texas 4 km (green) domains are also used by the TCEQ for State Implementation Plan (SIP) modeling. The CAMx 1.333/0.444-km domains (shown in Figure 2.1.2) were selected to include the most relevant GCAS flight tracks (overlaid in Figure 2.1.2) while considering computational demands.

Our WRF physics options and data sources (Table 2.1.1) are similar to those used by the TCEQ for SIP modeling. We used 0.25° Global Forecasting System (GFS) data assimilation system (GDAS) analysis data (https://www.ncdc.noaa.gov/data-access/model-data/model-datasets/global-data-assimilation-system-gdas) as initial conditions for the WRF meteorological model. This GDAS data is also used for boundary conditions and data assimilation. We configured WRF's output time steps to 15 minutes for the 1.333 and 0.444 km domains.

Table 2.1.2 presents the vertical layer mapping table from 44 WRF layers to 30 CAMx layers. This layer mapping is from the TCEQ SIP modeling.

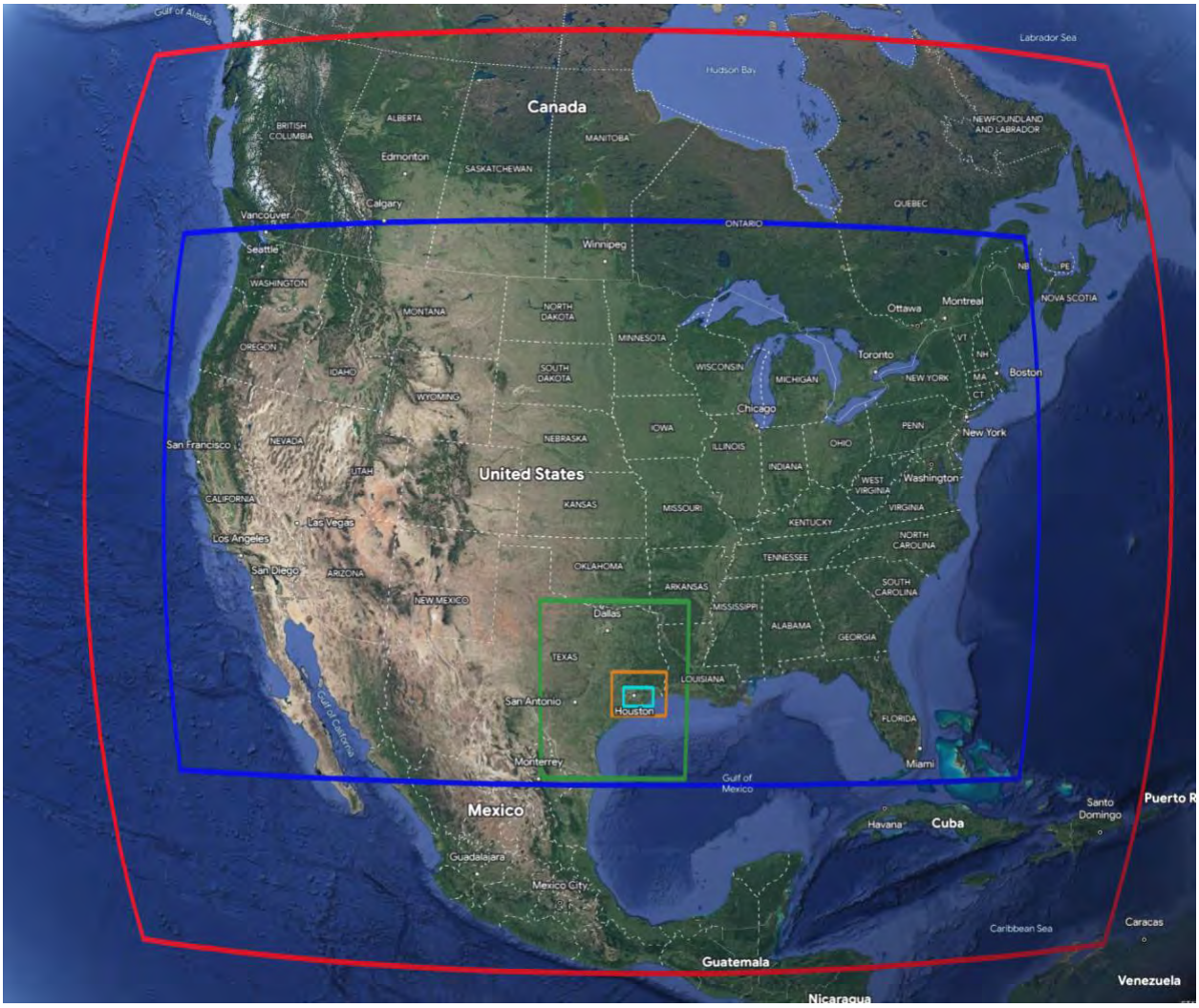


*Figure 2.1.1. CAMx 36/12/4/1.333/0.444 km modeling domains.*

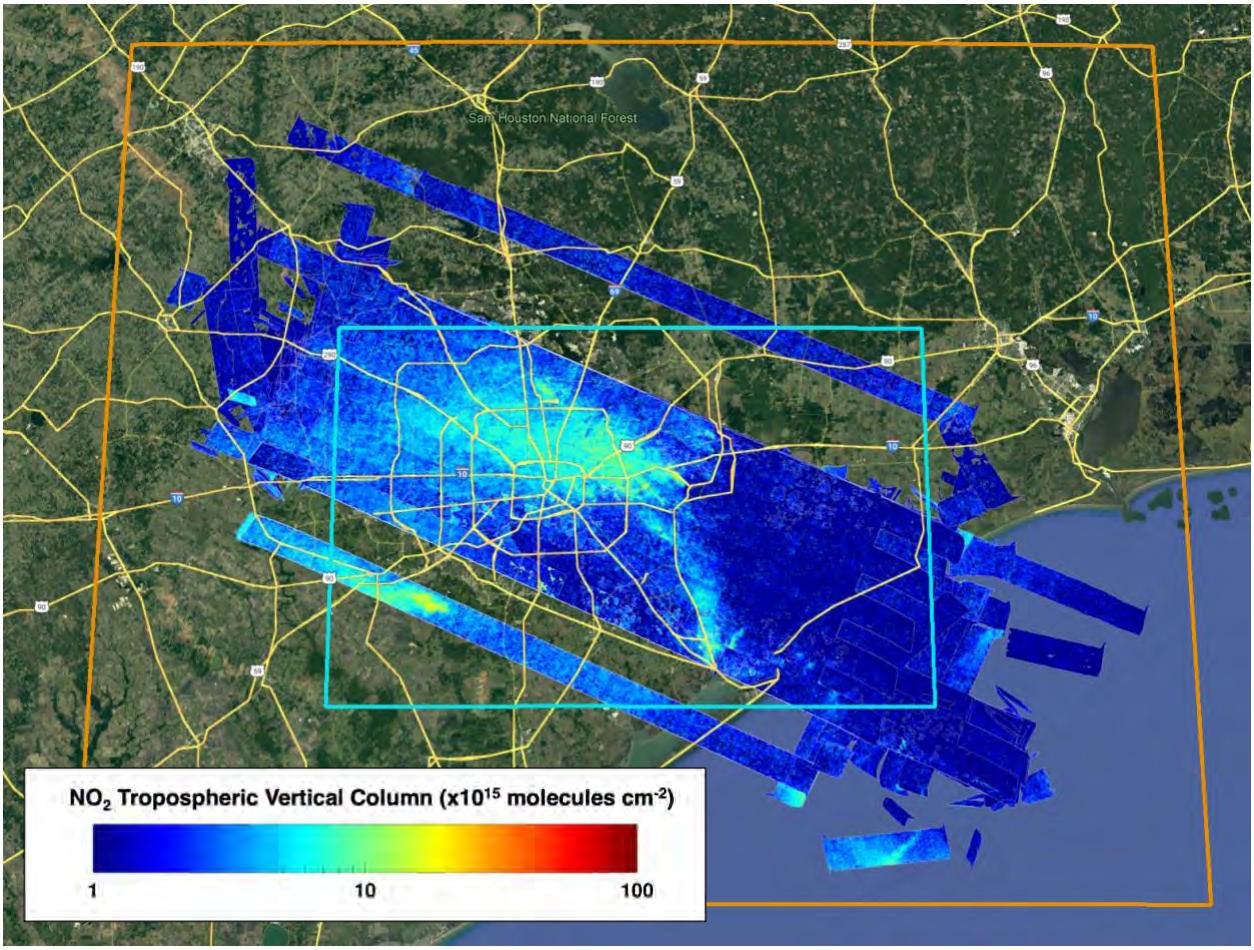


*Figure 2.1.2. CAMx 1.333/0.444 km modeling domains with GCAS $NO_2$ vertical column density measurement data from September 24, 2021 overlaid. Each flight day covered approximately the same area as represented here.*

*Table 2.1.1. WRF v4.3.3 physics options and data sources used in this study.*

| WRF Option | Option Selected |
|---|---|
| Analysis Data | 0.25° GDAS (IC/BCs and analysis nudging on the 36 and 12 km domains) |
| Microphysics | Thompson |
| Longwave Radiation | Rapid Radiative Transfer Model (RRTMG) |
| Shortwave Radiation | RRTMG |
| Surface Layer Physics | Revised MM5 surface layer scheme |
| LSM | Noah |
| PBL scheme | Yonsei University (YSU) |
| Cumulus scheme | Multi-Scale Kain-Fritsch (MSKF) on 36/12 km; none for 4/1.333/0.444 km |

*Table 2.1.2. Vertical layer mapping from 44 WRF layers to 30 CAMx layers.*

| WRF Layer No. | WRF Eta Level | WRF Layer Pressure (mb) | WRF Layer Top (m) | CAMx Layer No. | CAMx Layer Top (m) | CAMx Layer Thickness (m) |
|---|---|---|---|---|---|---|
| 44 | 0.000 | 50.00 | 20576 | | | |
| 43 | 0.010 | 59.63 | 19458 | | | |
| 42 | 0.025 | 74.08 | 18082 | 30 | 18082 | 3885 |
| 41 | 0.045 | 93.35 | 16616 | | | |
| 40 | 0.065 | 112.61 | 15427 | | | |
| 39 | 0.090 | 136.69 | 14198 | 29 | 14198 | 2977 |
| 38 | 0.115 | 160.77 | 13169 | | | |
| 37 | 0.145 | 189.67 | 12120 | | | |
| 36 | 0.175 | 218.57 | 11221 | 28 | 11221 | 1850 |
| 35 | 0.210 | 252.28 | 10304 | | | |
| 34 | 0.250 | 290.81 | 9372 | 27 | 9372 | 1599 |
| 33 | 0.290 | 329.34 | 8534 | | | |
| 32 | 0.330 | 367.87 | 7773 | 26 | 7773 | 1269 |
| 31 | 0.370 | 406.40 | 7073 | | | |
| 30 | 0.405 | 440.12 | 6504 | 25 | 6504 | 1040 |
| 29 | 0.440 | 473.83 | 5969 | | | |
| 28 | 0.475 | 507.54 | 5464 | 24 | 5464 | 870 |
| 27 | 0.510 | 541.26 | 4985 | | | |
| 26 | 0.540 | 570.16 | 4594 | 23 | 4594 | 737 |
| 25 | 0.570 | 599.05 | 4219 | | | |
| 24 | 0.600 | 627.95 | 3857 | 22 | 3857 | 684 |
| 23 | 0.630 | 656.85 | 3509 | | | |
| 22 | 0.660 | 685.75 | 3174 | 21 | 3174 | 325 |
| 21 | 0.690 | 714.64 | 2849 | 20 | 2849 | 314 |
| 20 | 0.720 | 743.54 | 2535 | 19 | 2535 | 304 |
| 19 | 0.750 | 772.44 | 2231 | 18 | 2231 | 247 |
| 18 | 0.775 | 796.52 | 1984 | 17 | 1984 | 241 |
| 17 | 0.800 | 820.60 | 1744 | 16 | 1744 | 235 |
| 16 | 0.825 | 844.68 | 1509 | 15 | 1509 | 230 |
| 15 | 0.850 | 868.76 | 1279 | 14 | 1279 | 135 |
| 14 | 0.865 | 883.21 | 1144 | 13 | 1144 | 134 |
| 13 | 0.880 | 897.66 | 1010 | 12 | 1010 | 132 |
| 12 | 0.895 | 912.11 | 878 | 11 | 878 | 130 |
| 11 | 0.910 | 926.56 | 748 | 10 | 748 | 86 |
| 10 | 0.920 | 936.19 | 662 | 9 | 662 | 85 |
| 9 | 0.930 | 945.82 | 577 | 8 | 577 | 84 |
| 8 | 0.940 | 955.46 | 493 | 7 | 493 | 84 |
| 7 | 0.950 | 965.09 | 409 | 6 | 409 | 83 |
| 6 | 0.960 | 974.72 | 326 | 5 | 326 | 82 |
| 5 | 0.970 | 984.35 | 243 | 4 | 243 | 82 |
| 4 | 0.980 | 993.99 | 162 | 3 | 162 | 81 |
| 3 | 0.990 | 1003.62 | 81 | 2 | 81 | 48 |
| 2 | 0.996 | 1009.40 | 32 | 1 | 32 | 32 |
| 1 | 0.998 | 1011.32 | 16 | | | |
| surface | 1.000 | 1013.25 | 0 | 0 | 0 | |

### 2.1.1.2 CAMx Model

The science options for our CAMx simulation (Table 2.1.3) are similar to the TCEQ's SIP modeling. We used CAMx v7.20 with the CB6r5 chemical mechanism. We first ran the model with TCEQ's 36/12/4-km SIP domains and then extracted initial and boundary conditions from the 4-km domain for our high-resolution 1.333/0.444 km $NO_2$ source apportionment technology (SAT) run focused on Houston.

*Table 2.1.3. Science options used for CAMx modeling.*

| Science Options | CAMx Configuration |
|---|---|
| Version | Version 7.20 |
| Time Zone | CST |
| Vertical Grid Mesh | 30 Layers with 32 m deep surface layer and 15 layers in the lowest 1.5 km |
| Horizontal Grids | 2-way nested grids with spacings of 1.333 and 0.444 km |
| Meteorology | 2021 WRF meteorology |
| Chemistry Mechanism | CB6r5 gas-phase mechanism |
| Chemistry Solver | EBI |
| Probing Tool | Ozone Source Apportionment Technology (OSAT) |
| Photolysis Rates | TUV version 4.8 with TOMS ozone column adjustment and in-line adjustment for clouds |
| Advection Scheme | Piecewise Parabolic Method (PPM) |
| Planetary Boundary Layer (PBL) mixing | K-theory with KV100 patch to enhance vertical mixing over urban areas within the lowest 100 m |
| In-line Ix Emissions On | Inorganic iodine (Ix) emissions from saltwater areas |
| Parallelization | MPI (18 threads) and OMP (6 threads) |

#### *2.1.1.2.1 CAMx $NO_2$ Source Apportionment Configuration*

We used the CAMx OSAT source apportionment tool to track $NO_2$ from several emission source sectors as listed in Table 2.1.4. To select individual electric generating units (EGUs) in our 0.444 km CAMx domain for $NO_2$ tracking we used a threshold of 0.8 tons per day (tpd) of NOx emissions. This threshold identified nine EGUs shown in the first nine rows of Table 2.1.4. Monthly total NOx emissions for each of these EGUs are shown in Table 2.1.7. We also selected on-road mobile, railyards, shipping and the George Bush Intercontinental (KIAH) and William P. Hobby (KHOU) airports for $NO_2$ tracking. All remaining NOx emissions were tracked together in the Other category.

*Table 2.1.4. CAMx Source Apportionment configuration.*

| Number | Emissions Source Sector |
|---|---|
| 1 | Air Liquide Bayport Complex |
| 2 | Cedar Bayou |
| 3 | W A Parish |
| 4 | Odyssey Energy Altura Cogen, LLC |
| 5 | Texas City Cogeneration |
| 6 | Pasadena Power Plant |

| Number | Emissions Source Sector |
|---|---|
| 7 | Channelview Cogeneration Facility |
| 8 | Deer Park Energy Center |
| 9 | South Houston Green Power Site |
| 10 | On-road mobile |
| 11 | Railyards |
| 12 | Shipping |
| 13 | KHOU airport |
| 14 | KIAH airport |
| 15 | Other |

#### *2.1.1.2.2 Modeling Emissions Inventory*

We updated the CAMx modeling emissions inventory from TCEQ's platform to incorporate 2021 hourly Continuous Emissions Monitoring Systems (CEMS) data for the nine EGUs listed in Table 2.1.4 plus two additional EGUs that were detected GCAS measurements. Table 2.1.5 summarizes NOx and VOC emissions for a September weekday across the CAMx 0.444 km domain. A pie chart shows in the same values in Figure 2.1.3.

*Table 2.1.5. CAMx 0.444 km domain-wide summary of average September weekday emissions (tons per day) by sector.*

| Emission Sector | NOx (tpd) | VOC (tpd) |
|---|---|---|
| EGUs | 25.5 | 0.2 |
| On-road mobile | 70.9 | 34.7 |
| Railyards | 4.2 | 0.3 |
| Shipping | 63.9 | 4.3 |
| KIAH airport | 6.4 | 0.8 |
| KHOU airport | 1.8 | 0.4 |
| Other | | |
| Off-road mobile* | 33.1 | 31.4 |
| Non-EGU Point Sources | 47.9 | 27.8 |
| Oil and Gas | 0.2 | 0.0 |
| Area | 92.8 | 623.2 |
| MEGAN biogenic | 25.9 | 319.7 |

* Includes non-road and railway emissions

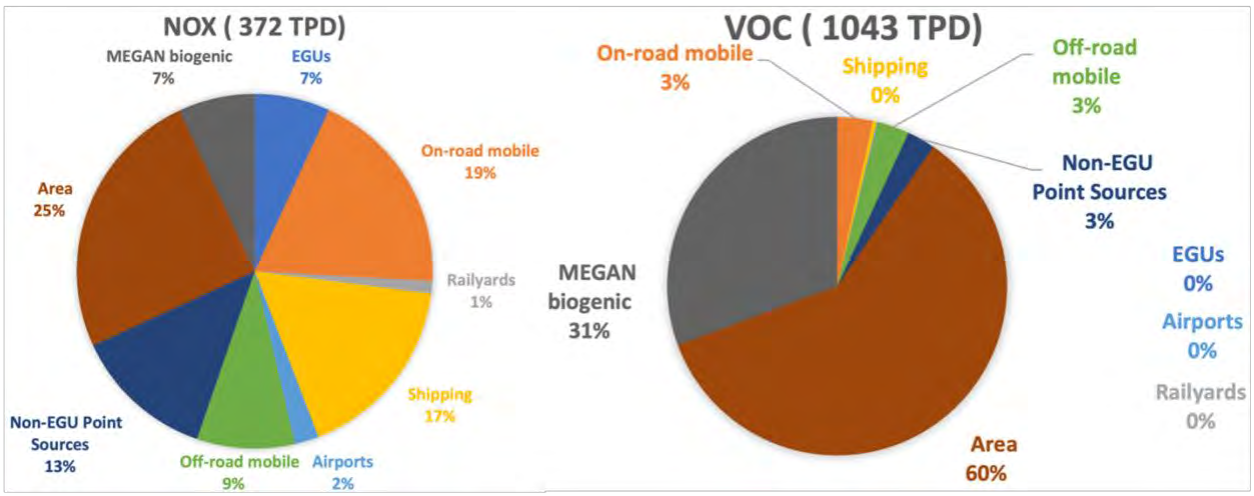


*Figure 2.1.3. Pie charts of NOx and VOC emissions data presented in Table 2.1.5.*

#### *2.1.1.2.3 Anthropogenic Emissions Inventory*

TCEQ developed the 2019 modeling emissions inventory for the Dallas-Fort Worth (DFW) and Houston-Galveston-Brazoria (HGB) Reasonable Further Progress (RFP) SIP revision. We identify data sources used in this inventory in Table 2.1.6. These tables are adapted from TCEQ's HGB and DFW RFP SIP revision. The changes that we implemented for this study are:

- Updating EGU point source emissions from 2019 to 2021 EPA Clean Air Markets Division (CAMPD) hourly data for the top NOx emitters
- Update shipping emissions using MARINER v2 supplied with 2021 AIS data for 1.333 and 0.444 km domains
- Re-process link-based on-road mobile emissions for 1.333 and 0.444 km domains with refined spatial resolution
- Use 2021 WRF meteorology for biogenic emissions and lightning NOx
- Reprocess all other gridded emissions from 4 km to 1.333 and 0.444 km grids without refining spatial resolution

*Table 2.1.6. Data sources for emissions inventory. Adapted from Table 3-4 of TCEQ's HGB and DFW RFP SIP Revision.*

| EI Source Category | Sector/Geographic area | Datasets/Models used for 2019 EI |
|---|---|---|
| Point | EGU | 2021 Clean Air Market Program Data for 11 Houston EGUs; TCEQ used 2019 CAMPD for other EGUs* |
| Point | Non-EGU, Texas | 2019 State of Texas Air Reporting System |
| Point | Non-EGU, Non-Texas | EPA 2016v1 Modeling Platform |
| Non-Point | Oil & Gas, Texas | 2019 Railroad Commission of Texas |
| Non-Point | Oil & Gas, Non-Texas | EPA 2017 Modeling Platform |
| Non-Point | Off-Shore | 2017 Bureau of Ocean Energy Management |
| Mobile | On-Road, Texas non-attainment areas | Motor Vehicle Emission Simulator (MOVES3) - link-based |
| Mobile | On-Road, other | MOVES3 - county based |
| Mobile | Non-Road, Texas | TexN2.2 |
| Mobile | Non-Road, Non-Texas | MOVES3 |
| Mobile | Off-Road Shipping, 4 km domain | 2019 Automatic Identification System and vessel characteristic IHS 2020; MARINER v1 |
| Mobile | Off-Road Shipping, 12 km domain | EPA 2016v1 Modeling Platform |
| Mobile | Off-Road Airports, Texas non-attainment areas | Texas Transportation Institute (TTI) 2020 data |
| Mobile | Off-Road Airports, other | EPA 2016v1 Modeling Platform |
| Mobile | Off-Road Locomotives, Texas nonattainment areas | TTI 2019 data |
| Mobile | Off-Road Locomotives, other | EPA 2016v1 Modeling Platform |
| Area | Area, Texas | 2020 Air Emissions Reporting Requirements |
| Area | Area, Non-Texas | EPA 2017 Modeling Platform |
| Other | International EI | 2019 Community Emission Data System; SMOKEv4.7_CEDS |
| Natural | Biogenic | MEGAN3.2 using 2021 WRF meteorology |
| Natural | Lightning NOx | Using 2021 WRF meteorology |
| Natural | Fires | 2019 MODIS and VIIRS; FINN v2.2 |

* TCEQ's 2019 modeling emission inventory used 2019 EPA CAMD AMPD hourly data for EGUs

Examples of the spatial distributions of on-road mobile and shipping NOx emissions can be seen in Figure 2.1.4.

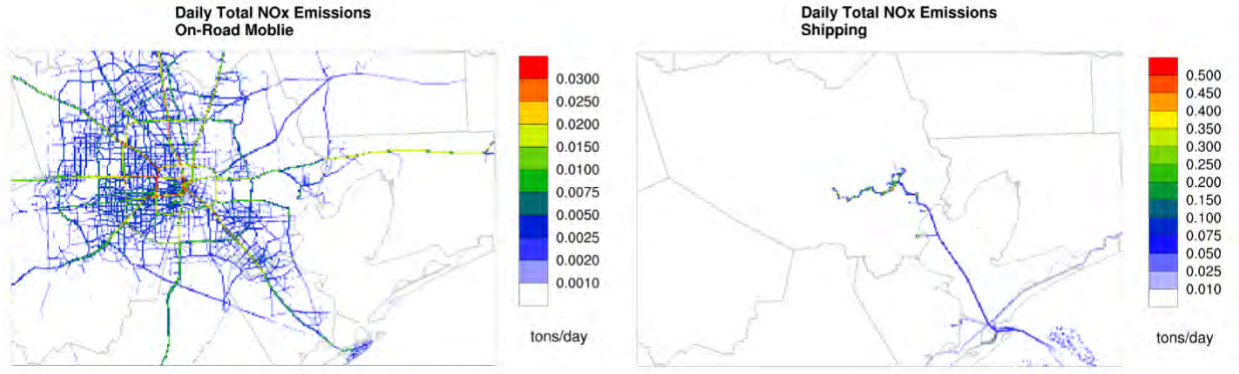


*Figure 2.1.4. Spatial distribution of (Left) on-road mobile and (Right) shipping daily total NOx emissions (tons per day) during September 2021 weekdays for 0.444 km domain.*

#### *2.1.1.2.4 2021 EGU Emissions Based on CEMS*

We developed hourly-specific EGU emissions using hourly CEMS data from CAMPD. Most EGUs use CEMS to report emissions under the Clean Air Act, including emissions of sulfur dioxide ($SO_2$), NOx, and $CO_2$, along with other parameters such as heat input. The EPA's CAMPD quality controls the reported raw hourly measurements which they provide on the CAMPD website[1]. We downloaded hourly data from EPA's CAMPD website for the eleven EGUs shown in Table 2.1.7 for the August 30-Sep 27, 2021 period. Stack parameters were based on TCEQ's 2019 emissions platform. Table 2.1.7 provides September 2021 total monthly CEMS NOx emissions for the eleven power plants examined in detail in this study. Comparison of initial CAMx results against GCAS column measurements revealed erroneous $NO_2$ signals from Greens Bayou and T H Wharton (last two rows in Table 2.1.7) that were caused by using old inventory data for these facilities. Our final CAMx simulation replaced emissions for these two power plants with September 2021 CEM data, resulting in a better agreement with GCAS measurements.

*Table 2.1.7. September 2021 monthly total $NO_x$ emissions for the eleven power plants examined in this study.*

| Station | NOx (tons/month) |
|---|---|
| W A Parish | 570.7 |
| Cedar Bayou | 73.0 |
| Pasadena Power Plant | 34.7 |
| Texas City Cogeneration | 34.6 |
| Odyssey Energy Altura Cogen, LLC | 30.8 |
| Deer Park Energy Center | 27.4 |
| South Houston Green Power Site | 25.9 |
| Air Liquide Bayport Complex | 25.0 |
| Channelview Cogeneration Facility | 25.0 |
| T H Wharton | 18.1 |
| Greens Bayou | 11.6 |

#### *2.1.1.2.5 Natural Emissions*

We estimated biogenic emissions for September 2021 using the Model of Emissions of Gases and Aerosols from Nature v3.2 developed by Ramboll in AQRP project 20-007; (MEGAN; (Guenther et al., 2012)). TCEQ estimated fire emissions from Fire INventory of NCAR (FINN) version 1 (Wiedinmyer et al., 2011). Ramboll developed lightning NOx emissions with the CAMx LNOx processor[2] using the 2021 WRF meteorological data. Considering the limited extent of the high-resolution CAMx domains and large degree of uncertainty with both the fire and LNOx emissions, we excluded these two emission sources from the 1.333/0.444 km CAMx simulation.

[1] https://campd.epa.gov/

[2] Available at https://www.camx.com/download/support-software/

### 2.1.2 Near-Surface Model Performance Evaluation

We evaluated CAMx $NO_2$ and ozone surface concentrations using data collected at TCEQ Continuous Air Monitoring Stations (CAMS) at all Houston CAMS within the 0.444 km CAMx domain. $NO_x$ monitors deployed for routine monitoring, e.g., at TCEQ CAMS, have limitations for $NO_2$. These monitors measure NO and consequently $NO_2$ is chemically converted to NO for measurement. The converter in these instruments could potentially capture other compounds including peroxyacyl nitrate (PAN) and a portion of nitric acid ($HNO_3$). However, a recent study comparing measurements from a high-sensitivity NOx instrument with photolytic converter (no interference of other species with $NO_2$) adjacent to TCEQ's NOx instrument at Tyler Airport (CAMS 82) in Northeast Texas found no evidence for substantial interference from these compounds (UH and Ramboll, 2021). However, this study also found that routinely operated NOx monitors can display considerable noise below about 5 ppb. For this study, we applied a cut-off value of 1 ppb. Our evaluation suggests that the model results are not sensitive to cut-off values between 1 and 5 ppb.

The scatter plot in Figure 2.1.5 shows hourly (7 AM-5 PM CST to correspond with GCAS flight measurement times) measurements and model pollutant concentrations at all Houston TCEQ CAMs located within the CAMx 0.444 km domain. Overall, the model displays a low $NO_2$ bias (mean bias, MB: -5.0 ppb; normalized mean bias, NMB: -59.1%) that is more pronounced when monitored $NO_2$ is high (e.g., morning rush hour). Figure 2.1.5 shows a map of the mean bias across the entire modeling episode at each TCEQ CAMS $NO_2$ monitor. CAMx shows a negative $NO_2$ bias at all sites. In general, monitors away from large emissions sources (e.g., Northwest Harris County CAMS 26) as well as monitors adjacent to Galveston Bay (e.g., Galveston 99$^{th}$ Street CAMS 1034) show the smallest $NO_2$ biases. In contrast, the monitors with the largest $NO_2$ biases are all located within the Houston core near large emission sources (e.g., roadways and industrial sources). For example, the largest $NO_2$ bias is at Houston SW Freeway C1066 (-13.9 ppb), and the CAMS is less than 50 m from the freeway. This suggests that even 444 m resolution is not enough to resolve the near-roadway $NO_2$ at this location.

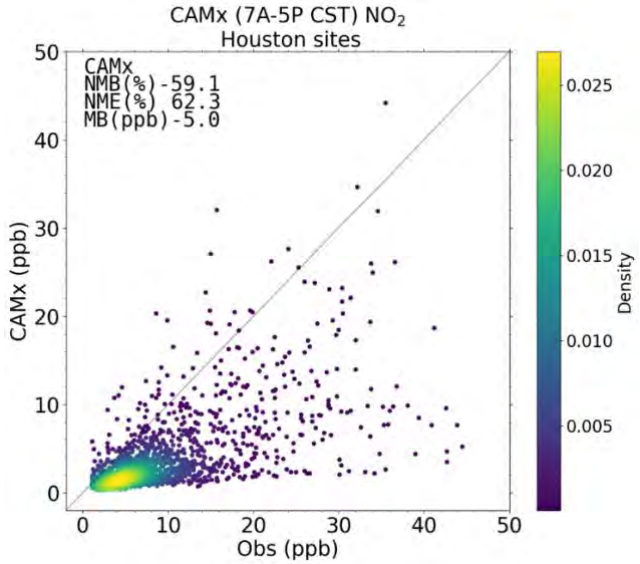


*Figure 2.1.5. Hourly CAMx (7 AM-5 PM CST) $NO_2$ plotted against observed $NO_2$ across all TCEQ CAMS sites within Houston for all days with GCAS flight measurements during the August 30-September 27, 2021 modeling period.*

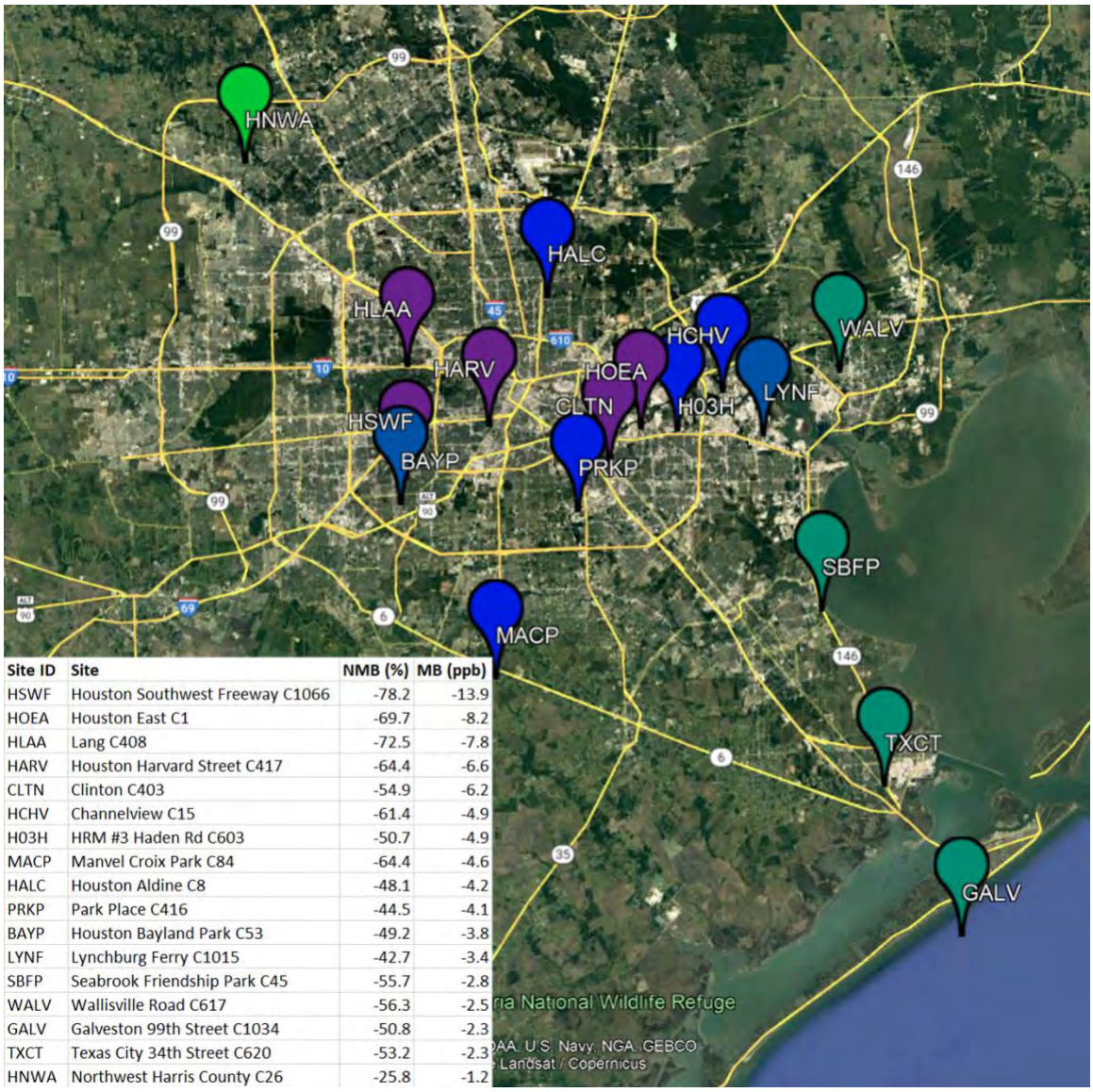


| Site ID | Site | NMB (%) | MB (ppb) |
|---|---|---|---|
| HSWF | Houston Southwest Freeway C1066 | -78.2 | -13.9 |
| HOEA | Houston East C1 | -69.7 | -8.2 |
| HLAA | Lang C408 | -72.5 | -7.8 |
| HARV | Houston Harvard Street C417 | -64.4 | -6.6 |
| CLTN | Clinton C403 | -54.9 | -6.2 |
| HCHV | Channelview C15 | -61.4 | -4.9 |
| H03H | HRM #3 Haden Rd C603 | -50.7 | -4.9 |
| MACP | Manvel Croix Park C84 | -64.4 | -4.6 |
| HALC | Houston Aldine C8 | -48.1 | -4.2 |
| PRKP | Park Place C416 | -44.5 | -4.1 |
| BAYP | Houston Bayland Park C53 | -49.2 | -3.8 |
| LYNF | Lynchburg Ferry C1015 | -42.7 | -3.4 |
| SBFP | Seabrook Friendship Park C45 | -55.7 | -2.8 |
| WALV | Wallisville Road C617 | -56.3 | -2.5 |
| GALV | Galveston 99th Street C1034 | -50.8 | -2.3 |
| TXCT | Texas City 34th Street C620 | -53.2 | -2.3 |
| HNWA | Northwest Harris County C26 | -25.8 | -1.2 |

*Figure 2.1.6. CAMx (7 AM-5 PM CST) $NO_2$ mean bias (ppb) at each Houston TCEQ CAMS site across all days with GCAS flight measurements during the August 30-September 27, 2021 modeling period.*

We present a similar scatter plot for CAMx maximum daily 8-hour average (MDA8) ozone compared to ozone observations at Houston CAMS in Figure 2.1.7. CAMx displays a small positive bias when observed ozone is below about 50 ppb and a small negative bias for higher observed ozone concentrations. Emery et al. (2017) defines the goal benchmark for MDA8 ozone as ± 5% for normalized mean bias (NMB) and < 15% for normalized mean error (NME). CAMx achieves the goal benchmark for NMB (-2.5%), while the NME (15.0%) is just outside the goal benchmark.

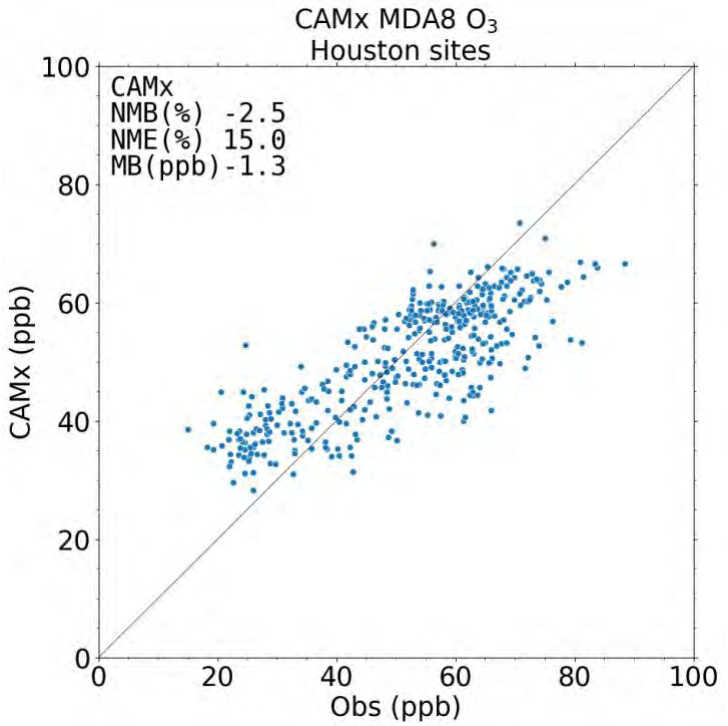


*Figure 2.1.7. CAMx and observed MDA8 ozone across all TCEQ CAMS sites within Houston for all days with GCAS flight measurements during the August 30-September 27, 2021 modeling period.*

## 2.2 Process the GCAS measurements

GCAS $NO_2$ and HCHO column measurements were acquired during NASA G-V flights on 12 different days over the Houston metropolitan area during late August and September 2021 (https://www-air.larc.nasa.gov/missions/tracer-aq/docs/TRACERAQ_SciencePlan_v1.pdf) as part of the NASA / TCEQ TRACER-AQ field campaign. All GCAS data are publicly available at the NASA Langley data archive: https://www-air.larc.nasa.gov/cgi-bin/ArcView/traceraq.2021. Table 2.2.1 shows the 10 flight days used in this project, as well as the meteorological conditions during the days. There were two flights – a test flight on August 30, and a flight over the Gulf of Mexico on September 27 – that were not used for this project. Figure 2.2.1 shows the GCAS $NO_2$ measurements from September 8, 2021, a code red ozone day in the Houston metropolitan area demonstrating the granularity of information provided. Distinct $NO_2$ plumes are clearly seen from the areas of Mont Belvieu, Baytown, Deer Park, and Texas City.

*Table 2.2.1. Flight days of the NASA G-V during September 2021 and associated meteorological conditions.*

| Day of Sept 2021 | Day of the Week | High Temp | Wind direction | Additional comments |
|---|---|---|---|---|
| 1 | Wed | 96 F | Weak SW winds | Thunderstorms from S to N, 11 AM to 4 PM |
| 3 | Fri | 93 F | Weak S winds | Scattered thunderstorms 12 PM to 4 PM |
| 8 | Wed | 94 F | N turning NE | Clear skies and no rain |
| 9 | Thurs | 95 F | N turning NE | Afternoon fair weather clouds, no rain |
| 10 | Fri | 93 F | NE turning E | Clear skies, no rain, some long-range smoke aloft |
| 11 | Sat | 93 F | E winds | Afternoon fair weather clouds, no rain |
| 23 | Thurs | 83 F | E winds | Clear skies, no rain, cold font overnight Sept 21 |
| 24 | Fri | 84 F | E turning SE | Clear skies, no rain |
| 25 | Sat | 87 F | NE turning E | Clear skies, no rain |
| 26 | Sun | 83 F | Calm then SE | Clear skies, afternoon fair weather clouds |

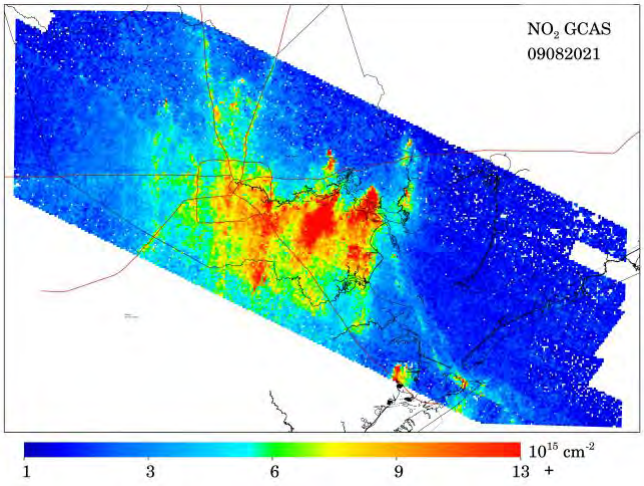


*Figure 2.2.1. GCAS measurements acquired during all daylight hours on Wednesday September 8, 2021.*

In this Task, the GCAS measurements were re-processed in two different stages. In the first stage, the data were re-processed to better account for missing data (R1 in the TRACER-AQ dataset archive). This stage was a data re-formatting change, and almost no measurements were altered during this re-processing. Second, the data were re-processed to include $NO_2$ vertical profile estimates from the CAMx simulation. Vertical profile information is needed to process the GCAS measurements because remote sensing instruments have different sensitivities at different altitudes above the surface (less sensitive near the surface) and this needs to be accounted for. Upon original release of this dataset, a global model – GEOS-CF – with 0.25° × 0.25° spatial resolution was used to process the GCAS measurements, but in this project 444 × 444 $m^2$ spatial resolution information was used instead.

To determine the accuracy and precision of the GCAS data, we compare to Pandora measurements of total column $NO_2$. Measurements are collocated to within 15 minutes of the GCAS measurement. For comparisons between Pandora and GCAS, there is a substantial but predictable "above aircraft" column that is not reflected in the GCAS measurements but is reflected in the Pandora measurements. This is caused primarily by $NO_2$ in the stratosphere. To account for this, we approximate the above aircraft component of the GCAS $NO_2$ column based on TROPOMI stratospheric values and add this correction factor.

As shown in Figure 2.2.2, the GCAS measurements had a very strong correlation of $r^2$ = 0.79 and small normalized mean bias of +5.6% compared with the Pandora. We found that re-processing the GCAS measurements with 444 × 444 $m^2$ spatial resolution model information had a beneficial effect, but less than we originally suspected. Using the 444 × 444 $m^2$ spatial information to re-process the GCAS measurements, increased the $r^2$ correlation from $r^2$ = 0.80 to $r^2$ = 0.81 and reduced the normalized mean bias from +6.3% to +3.2%. *The strong correlation and low normalized bias of the GCAS measurements indicates the high fidelity of these measurements in polluted areas such as Houston.* However, the Pandora instruments were sited at polluted locations, and the performance of the GCAS at less polluted sites is still unclear.

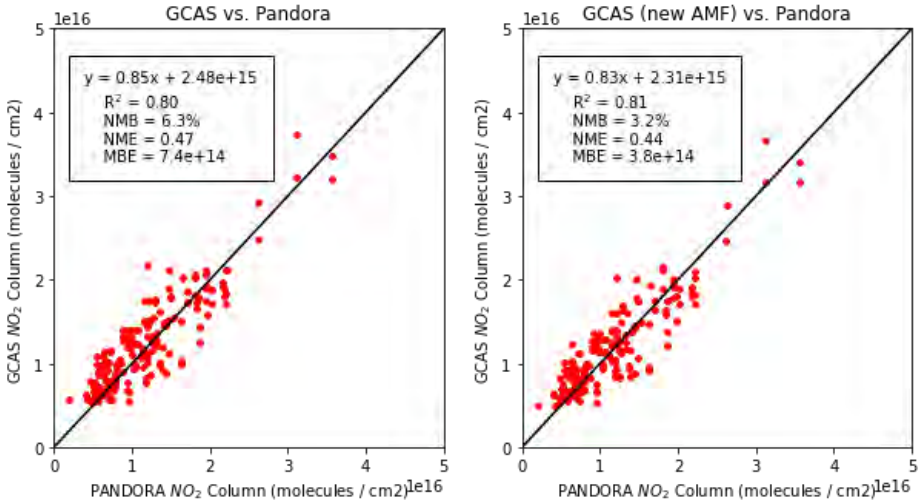


*Figure 2.2.2. Evaluation of GCAS $NO_2$ columns compared to Pandora with (Left) the GEOS-CF air mass factor and (Right) with a CAMx-based air mass factor developed in this project. GCAS observations were mapped to the CAMx grid and compared in the single grid cell that contained the Pandora site. The Pandora measurements closest in time with the GCAS overpasses were used for comparison; however, Pandora observations beyond +/- 15 minutes of a GCAS overpass were not considered.*

To determine whether GCAS performance was better at very polluted sites or moderately polluted sites, we performed the analysis for each of the three Pandora measurement sites individually (La Porte, Aldine, and University of Houston). Of the three measurements sites, the University of Houston site was the most polluted location for $NO_2$, but all three typically measured $NO_2$ values indicative of a polluted urban environment. Figure 2.2.3 shows excellent agreement at the Aldine ($r^2$=0.81 and NMB=+16.4%) and the University of Houston ($r^2$=0.85 and NMB=–1.5%) measurement sites, and only marginally degraded correlation and comparable bias at the La Porte site ($r^2$=0.45 and NMB=–4.6%). Correlation at the LaPorte site may be lower because Pandora and GCAS observed a smaller dynamic range in values. Interestingly, there were two Pandoras co-stationed at the University of Houston Moody Tower site – Pandora 188 located on top of the roof of the building and Pandora 25 located at ground-level – and there is larger column $NO_2$ observed by Pandora 25 at ground-level, which is a real difference.

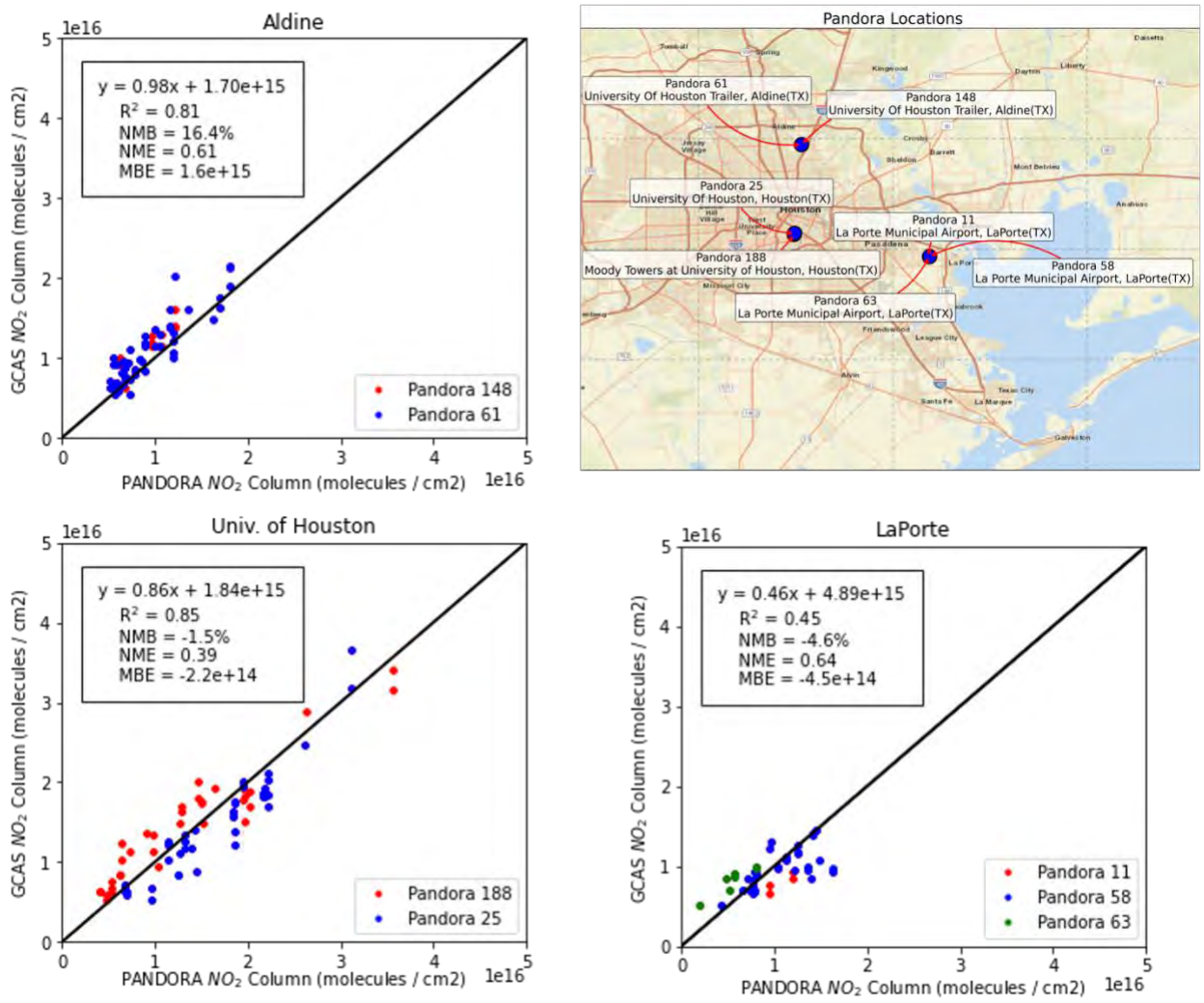


*Figure 2.2.3. Locations of the Pandora instruments and their correlation with GCAS within +/- 15 minutes*

Comparing GCAS HCHO to Pandora shows strong correlation – albeit less than $NO_2$ – and a strong linear relationship. We suspect that Pandora MAX-DOAS might have a low bias, but we are still working with the Pandora team to determine the cause. While the GCAS HCHO measurements are noisy, they do seem to capture the dynamic range observed by Pandora.

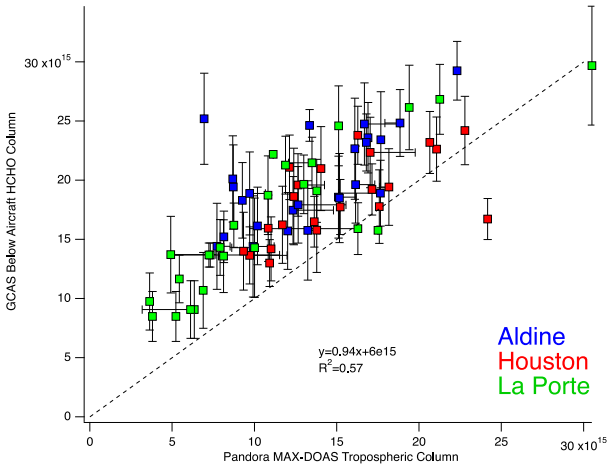


*Figure 2.2.4. GCAS HCHO measurement compared to the nearest Pandora MAX-DOAS observation in time (within +/- 15 minutes). The horizontal bars represent the max/min of Pandora in that time frame.*

## 2.3 Process the satellite $NO_2$ measurements

Measurements of tropospheric vertical column $NO_2$ from TROPOMI are available daily between 1:30 PM – 3:00 PM local time over the Houston metropolitan area every day since April 30, 2018. For this project, we used measurements from the version 2.3.1 algorithm released in December 2021. We screened the TROPOMI data for clouds and erroneous data using the recommended qa_flag > 0.75 filter. The TROPOMI $NO_2$ version 2.3.1 data are publicly available at: https://data-portal.s5p-pal.com/products/no2.html. Daily snapshots of TROPOMI $NO_2$ as well as the September 2021 monthly average are shown in Figure 2.3.1.

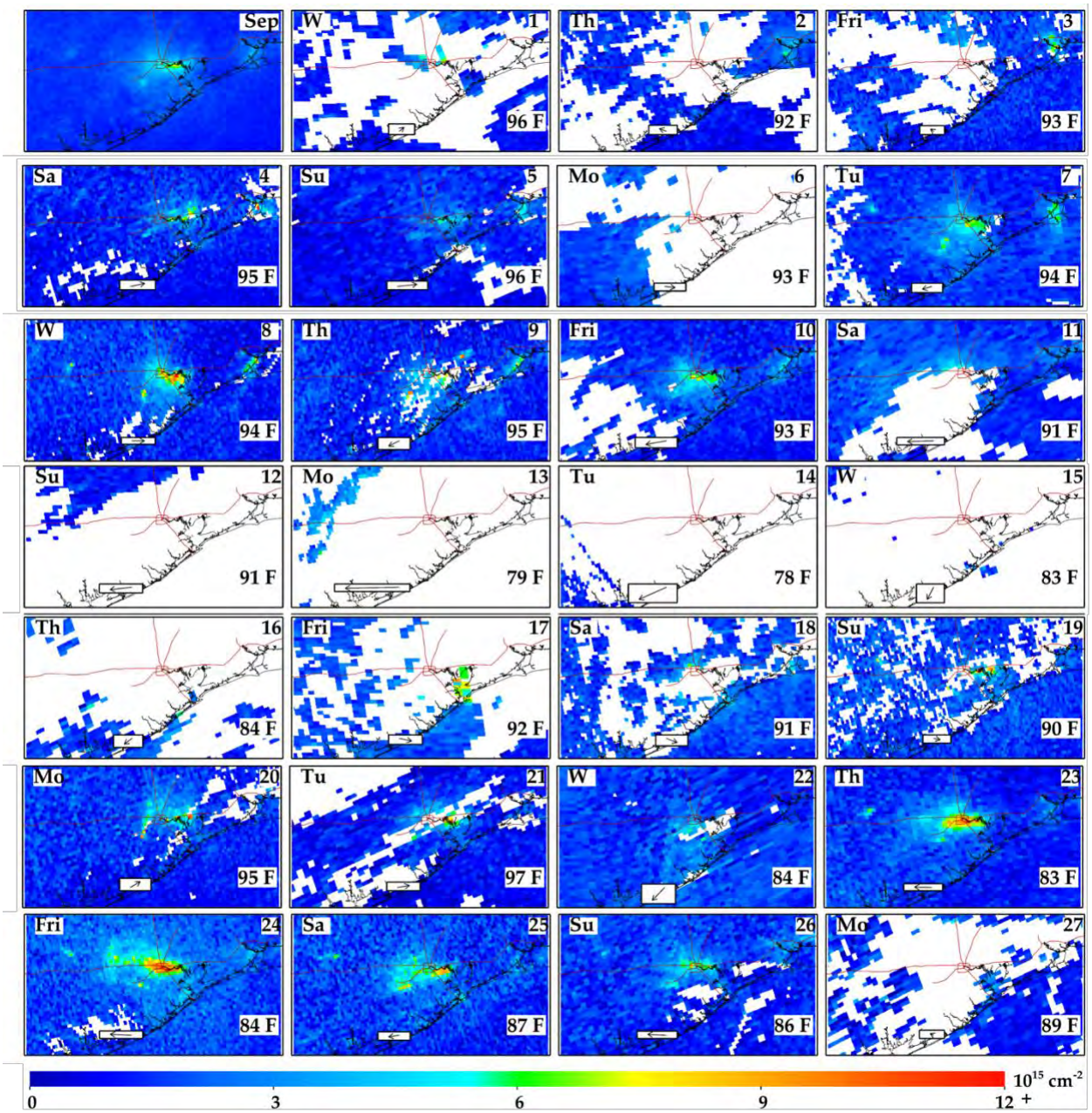


*Figure 2.3.1. TROPOMI $NO_2$ v2.3.1 tropospheric column measurements over the Houston metropolitan area. Information about the day-of-the-week, maximum daily high temperature, and predominant wind direction in the early afternoon are overlaid.*

We then re-gridded the $NO_2$ column information onto the 444 × 444 $m^2$ CAMx grid and re-calculated the $NO_2$ vertical columns using the CAMx simulated $NO_2$ vertical profiles. Inclusion of the $NO_2$ vertical profiles estimates from the CAMx simulation – similar to the GCAS – increased TROPOMI values in the urban polluted areas and decreased the values in the suburban and rural areas. The max value of the monthly tropospheric column $NO_2$ average increased by +11 % from 7.9 x $10^{15}$ molecules/$cm^2$ to 8.8 x $10^{15}$ molecules/$cm^2$, while the mean value decreased by –8% from 2.5 x $10^{15}$ molecules/$cm^2$ to 2.3 x $10^{15}$ molecules/$cm^2$. This is consistent with other literature showing an increase in the values in the most polluted areas when higher resolution model information is included.

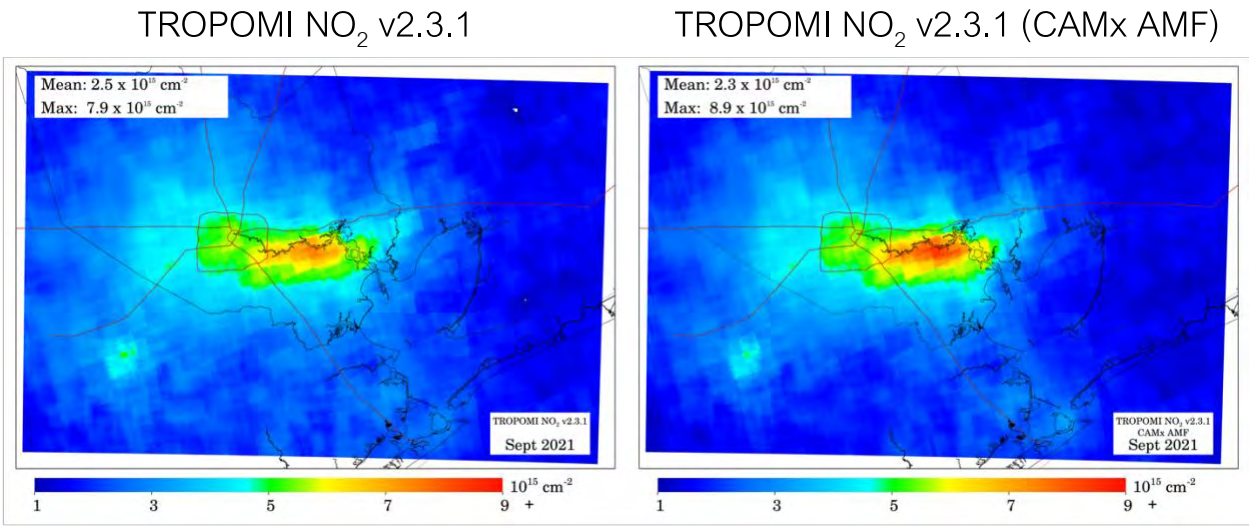


*Figure 2.3.2. TROPOMI $NO_2$ v2.3.1 tropospheric column measurements over the Houston metropolitan area. (Left) Using the operational air mass factor and (Right) using a CAMx-based air mass factor*

*Measurements from TROPOMI $NO_2$ version 2.3.1 show very good correlation $r^2$ = 0.62 and a small but systematic –11.7% NMB when compared to the Pandora instruments.* Updating the air mass factor had almost no effect on the correlation or bias at the Pandora measurement sites. The underestimated normalized mean bias may be due to satellite pixel size which cannot resolve individual plumes and neighborhood-scale features.

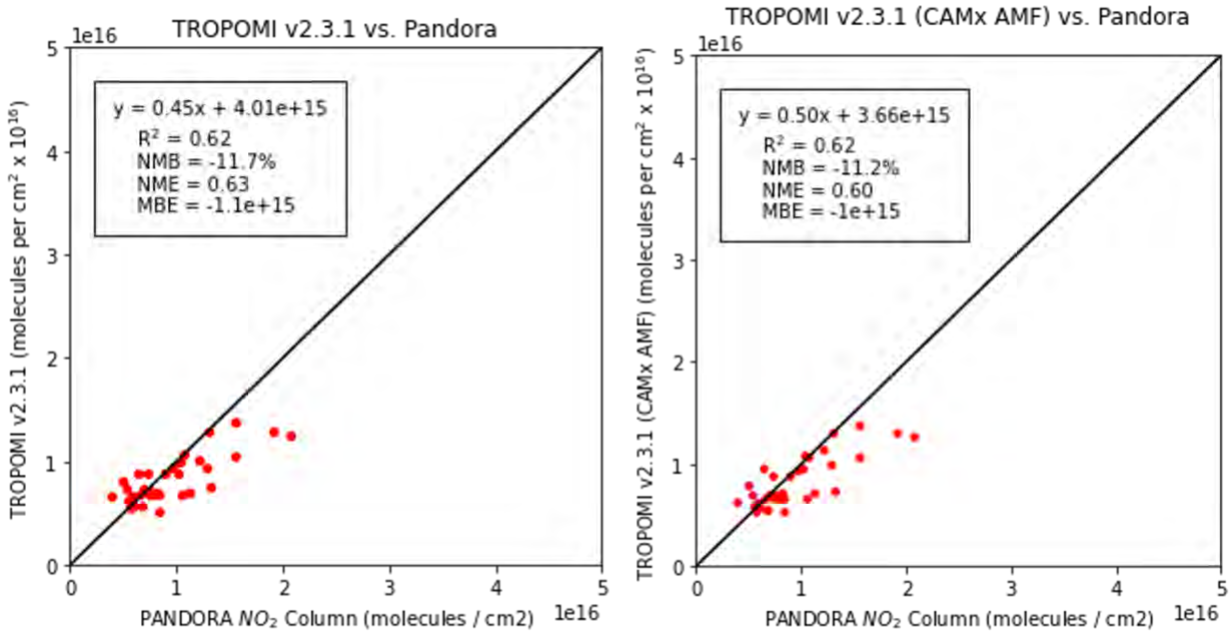


*Figure 2.3.3. TROPOMI $NO_2$ v2.3.1 total column measurements with the (Left) operational AMF and (Right) re-processed CAMx AMF. Pandora observations that are closest in time to the TROPOMI overpass time are matched to the value of the TROPOMI grid cell which includes the Pandora site. Measurements that are beyond +/- 15 minutes of the overpass time are excluded.*

To facilitate a direct comparison between GCAS and TROPOMI we average both to a 0.1° × 0.1° grid; this coarser grid is more appropriate since we cannot expect TROPOMI – with a native resolution of approximately 5 km – to capture the fine-scale $NO_2$ features that GCAS can measure. When doing a direct comparison between $NO_2$ columns from GCAS and TROPOMI during all collocations (Figure 2.3.4), TROPOMI has a normalized mean bias of –27.3%. The correlation between the two measurements, however, was very strong ($r^2 = 0.93$).

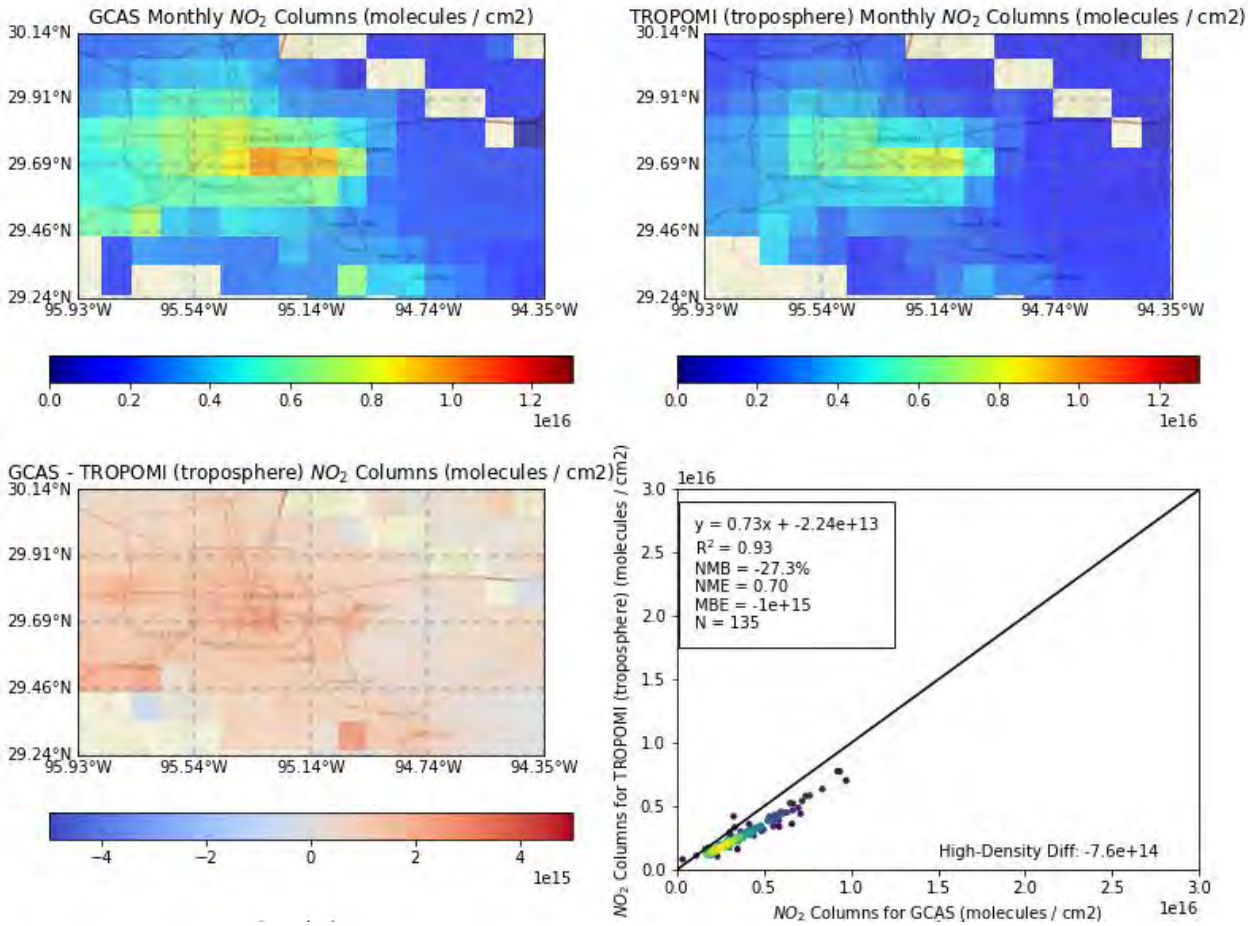


*Figure 2.3.4 (Top Left) GCAS monthly column $NO_2$ for all measurements within a +/- 1.5 hour time window of each day's TROPOMI mid-afternoon overpass time compared to (Top Right) $NO_2$ from TROPOMI. (Bottom Left) Difference between GCAS and TROPOMI. (Bottom Right) Scatterplot of CAMx vs. TROPOMI; yellow points indicate that there are a high number of other points close to it.*

A new version of the TROPOMI $NO_2$ algorithm – version 2.4 – was released by the European Space Agency on March 30, 2023. This version of the algorithm had adjustments to the surface reflectivities used to calculate the air mass factor and tropospheric vertical column; the slant column measurement was not modified in the new version 2.4 algorithm.

In Figure 2.3.5, measurements from the TROPOMI $NO_2$ version 2.3.1 and version 2.4 algorithms are compared to each other. In bottom row of Figure 2.3.5, the performance of the version 2.3.1 and version 2.4 algorithms are compared to the Pandora measurements in a similar manner as Figure 2.3.3. In most cases, the version 2.4 algorithm has smaller values in the Houston metropolitan area. This resulted in slightly degraded performance at the Pandora measurements sites. The version 2.4 has a worse normalized mean bias (V2.4: –15.0%, V2.3.1: –11.7%) and modestly reduced correlation (V2.4: $r^2 = 0.60$, V2.3.1: $r^2 = 0.62$). Future work will compare to the NASA MINDS TROPOMI $NO_2$ algorithm, which was released in Fall 2022 (https://disc.gsfc.nasa.gov/datasets/TROPOMI_MINDS_NO2_1.1/).

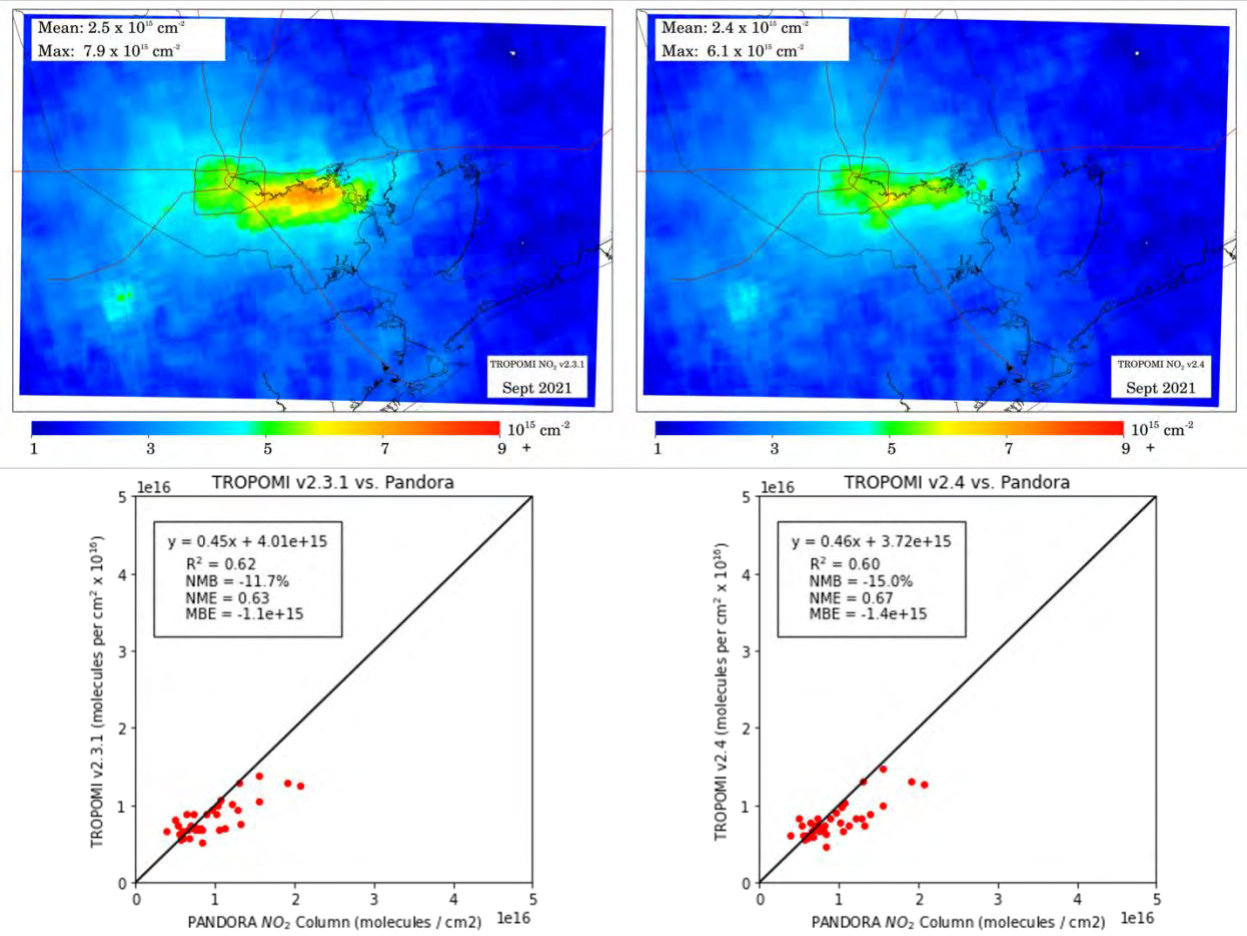


*Figure 2.3.5. TROPOMI $NO_2$ (Left) v2.3.1 total column measurements and (Right) v2.4 total column measurements. (Top row) The September 2021 monthly average during clear skies. (Bottom row) Pandora observations that are closest in time to the TROPOMI overpass time are matched to the value of the TROPOMI grid cell which includes the Pandora site. Measurements that are beyond +/- 15 minutes of the overpass time are excluded.*

## 2.4 Calculating $NO_X$ from GCAS $NO_2$ airshed measurements

$NO_X$ emission rates can be inferred from $NO_2$ using a combination of spatially continuous $NO_2$ airshed measurements, wind data, and statistical inversion techniques. By tracking the $NO_2$ plume decay since origination, the $NO_X$ emissions at the source can be inferred. In this project, we use two methods to estimate $NO_X$ emissions: 1) Exponentially modified Gaussian (EMG) fit (Beirle et al., 2011) for several of the point sources and 2) Flux divergence (Beirle et al., 2019) for a more spatially complete estimate. Method 1 has applicability to only point sources or pseudo point sources (e.g., an airport), whereas Method 2 has suitability for a wider range of sources but needs additional assumptions to derive $NO_X$ emissions rates.

### 2.4.1 EMG fit to estimate $NO_X$ emissions from point sources

#### 2.4.1.1 Background

In this Task, we used the EMG fit to estimate the $NO_X$ emissions from several point sources in the Houston metropolitan area. Briefly, a point source $NO_2$ plume is integrated perpendicularly across its width to create a 1-dimensional line density. This 1-D line density has a Gaussian shape at the plume source and an exponential plume decay downwind as $NO_2$ is converted into other chemical species. An illustrative example of this is shown in Figure 2.4.1.

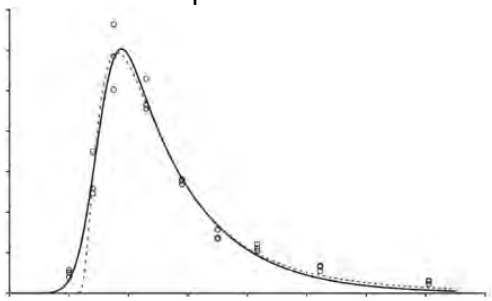

*Figure 2.4.1. Illustrative example of a Gaussian plume with exponential decay. Scatter points are the integrations across the plume width, while the solid/dotted lines are best fits of the data using an Exponentially Modified Gaussian fit.*

The EMG fit equation is shown below:

$$NO_2\ Line\ Density = \alpha\left[\frac{1}{x_o} exp\left(\frac{\mu}{x_o} + \frac{\sigma^2}{2x_o^2} - \frac{x}{x_o}\right)\Phi\left(\frac{x-\mu}{\sigma} - \frac{\sigma}{x_o}\right)\right] + \beta \qquad (1)$$

where $\alpha$ is the total number of $NO_2$ molecules observed near the emission source, excluding the effect of background $NO_2$, $\beta$; $x_o$ is the e-folding distance downwind, representing the length scale of the $NO_2$ decay; $\mu$ is the location of the apparent source relative to the assumed pollution source center; $\sigma$ is the standard deviation of the Gaussian function, representing the Gaussian smoothing length scale; $\Phi$ is the Gaussian cumulative distribution function.

$NO_X$ emissions (Equation 2) can be inferred from four variables: two variables from the fit – α ($NO_2$ at the source) and $x_o$ (decay distance) – and two additional variables – $NO_X/NO_2$ ratio and w (horizontal wind speed). The $NO_X/NO_2$ ratio is assumed to be 1.32 (Beirle et al., 2019) and horizontal wind speed is obtained from the 100-m height of the ERA5 re-analysis.

$$NO_x\ Emissions = \frac{NO_X}{NO_2}\left(\frac{\alpha * w}{x_o}\right) \qquad (2)$$

#### 2.4.1.2 EMG fit applied to several point sources in Houston

The first part of this Task was to apply the EMG fit to the GCAS measurements overpassing the W.A. Parish Power Plant $NO_2$ plume at 3 PM local time on September 24, 2021 to determine whether the method is able to replicate the stack-measured CAMPD hourly emissions. Table 2.4.1 shows the hourly $NO_X$ emission rates in units of kmol per hour – originally reported as lbs per hour – between 9 AM and 9 PM local time on September 24, 2021. $NO_X$ emission rates were relatively constant during this time frame, between 12.5 – 14.7 kmol per hour. At 3 PM local time, the hourly $NO_X$ emissions rate was 13.6 kmol per hour.

*Table 2.4.1 Hourly CAMPD $NO_X$ emissions on September 24, 2021 from the W. A. Parish Power Plant.*

| Local time | NOx (lbs) | NOx (kmol) |
|---|---|---|
| 9:00 AM | 1262 | 12.4 |
| 10:00 AM | 1246 | 12.3 |
| 11:00 AM | 1204 | 11.9 |
| 12:00 PM | 1489 | 14.7 |
| 1:00 PM | 1470 | 14.5 |
| 2:00 PM | 1421 | 14.0 |
| 3:00 PM | 1383 | 13.6 |
| 4:00 PM | 1350 | 13.3 |
| 5:00 PM | 1401 | 13.8 |
| 6:00 PM | 1318 | 13.0 |
| 7:00 PM | 1309 | 12.9 |
| 8:00 PM | 1324 | 13.1 |
| 9:00 PM | 1268 | 12.5 |

In Figure 2.4.2, we apply the EMG fit to the GCAS measurements over the W.A. Parish Power Plant $NO_2$ plume and derive a rate of 13 kmol per hour. The same method is applied to the CAMx simulation, which ingests the CAMPD hourly measurements, and derive a rate of 18 kmol per hour. The uncertainty of the EMG fit method has been reported to be between 40 – 60% (Lu et al., 2015; Verstraeten et al., 2018). Both GCAS and CAMx are able to replicate the CAMPD emissions within appropriate uncertainty bounds. The disagreements between the CAMPD stack measurements and the EMG fit on both the GCAS measurements and CAMx simulation are likely related to the assumed $NO_X/NO_2$ ratio and wind speed. The $NO_X/NO_2$ has variation at these fine spatial scales, which we do not account for. The wind speed also has uncertainty – if a higher vertical level is assumed – then wind speed would increase and so would the inferred $NO_X$ emissions rate.

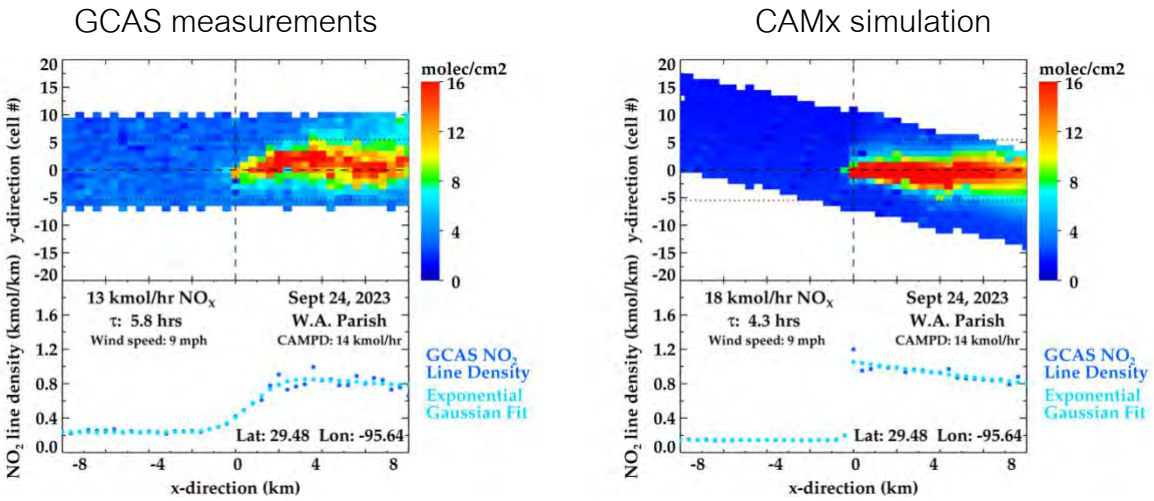


*Figure 2.4.2. EMG fit applied to the (Left) GCAS column $NO_2$ measurements and (Right) CAMx column $NO_2$ simulation at the W.A. Parish Power Plant at 3 PM local time on September 24, 2021.*

The EMG fit was then applied to five additional areas with points source $NO_X$ emissions in the Houston metropolitan area including Baytown, Channelview, Mont Belvieu, Texas City, and the IAH international airport.

Estimates for two point sources in the Houston area are shown in Figure 2.4.3 (Baytown), and Figure 2.4.4 (Channelview). In the Baytown area, we find a large discrepancy between the GCAS measurements and the CAMx simulation. Using the GCAS measurements, we find a $NO_X$ emissions rate of 14 kmol per hour, while the CAMx simulation had an estimate of 8 kmol per hour. The difference between GCAS and CAMx exceeds the 40 – 60% uncertainty of the method giving us some confidence that there is an underestimate of $NO_X$ emissions in the Baytown area. In the Channelview area, we find better agreement: 3.2 kmol per hour from GCAS and 2.6 kmol per hour from CAMx. The method did not work at Mont Belvieu, Texas City, and IAH. This is because plumes at these locations were not isolated enough from nearby sources to garner a good fit. However, as we note in Section 2.5, we did not see large discrepancies at any of these locations in the $NO_2$ comparison.

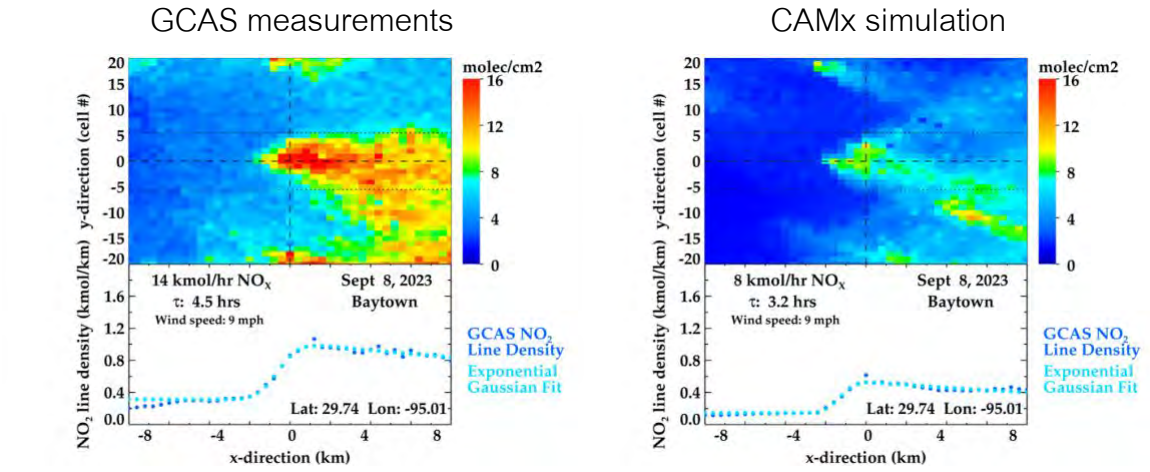


*Figure 2.4.3. EMG fit applied to the (Left) GCAS column $NO_2$ measurements and (Right) CAMx column $NO_2$ simulation at the Baytown area at 1 PM local time on September 8, 2021.*

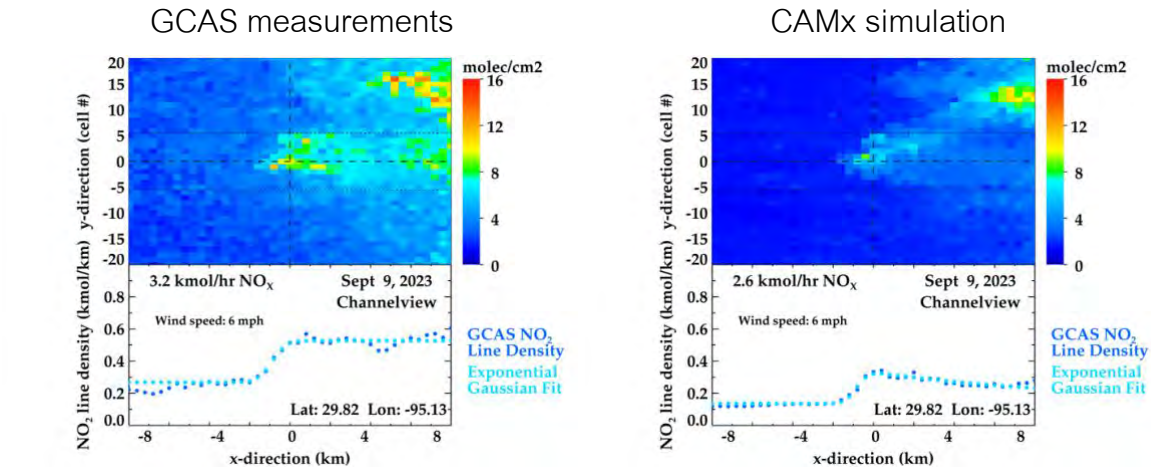


*Figure 2.4.4. EMG fit applied to the (Left) GCAS column $NO_2$ measurements and (Right) CAMx column $NO_2$ simulation at the Channelview area at 1 PM local time on September 9, 2021.*

### 2.4.2 Flux divergence to estimate NOx emissions

#### 2.4.2.1 Background

The flux divergence method has been shown to identify point sources in the TROPOMI $NO_2$ retrievals with higher resolution than averaged vertical column densities. Initially, the method was applied over Riyadh, Germany and South Africa and was used to estimate NOx emissions from large point sources (Beirle et al., 2019). The method was subsequently used to develop a global catalog of NOx point sources (Beirle et al., 2021, 2023). Due to TROPOMI's higher resolution compared with OMI, the flux divergence method can identify emissions within individual urban areas (Benjamin de Foy & Schauer, 2022). This method was applied over the U.S. and identified some of the largest highways in the country (Sun, 2022). Goldberg et al. (2022) used the flux divergence method to evaluate SIP modelling emission inventories in Texas.

#### 2.4.2.2 Flux divergence applied in Houston metropolitan area

The flux divergence method works best with long temporal averages. For TROPOMI analysis, annual or multi-year averages are used. We adapted the method for the current project to handle GCAS data from 27 individual scenes spanning 10 days. We found that the method worked best when the GCAS data was oversampled to the 444 × 444 $m^2$ CAMx grid. Only pixels with an aircraft roll angle below 0.5 degrees were used. We interpolated the WRF-CAMx winds to the time of the GCAS overpass. We used second-order differences and performed the flux divergences along the x/y axes (i.e., using the cells to the north, south, east, and west of the central cell). We also calculated the flux divergence for the cross-terms (i.e., using the cells to the north-east, south-east, south-west and north-west of the central cell). Averaging both the x/y estimate and the cross-estimate led to smoother divergence fields with less noise.

The method was initially performed using the GCAS standard retrievals and the ERA5 wind reanalysis product (https://www.ecmwf.int/en/forecasts/dataset/ecmwf-reanalysis-v5). While this gave good results, we found that the level of noise was reduced and the known sources were better identified when we used the GCAS retrievals that were corrected using the CAMx air mass factors, and when we used the WRF-CAMx meteorology. These sensitivity tests revealed that CAMx simulations can be used to yield clear improvements in the flux divergence method.

The flux divergence method was able to identify the main point sources in the Houston CAMx domain: power plants and refineries (see Figure 2.4.5), as well as the IAH international airport. In addition, the method identified the area of the ship channel as well as the route of the ships sailing through the Galveston Bay. Finally, the method clearly identified the major highways in the region.

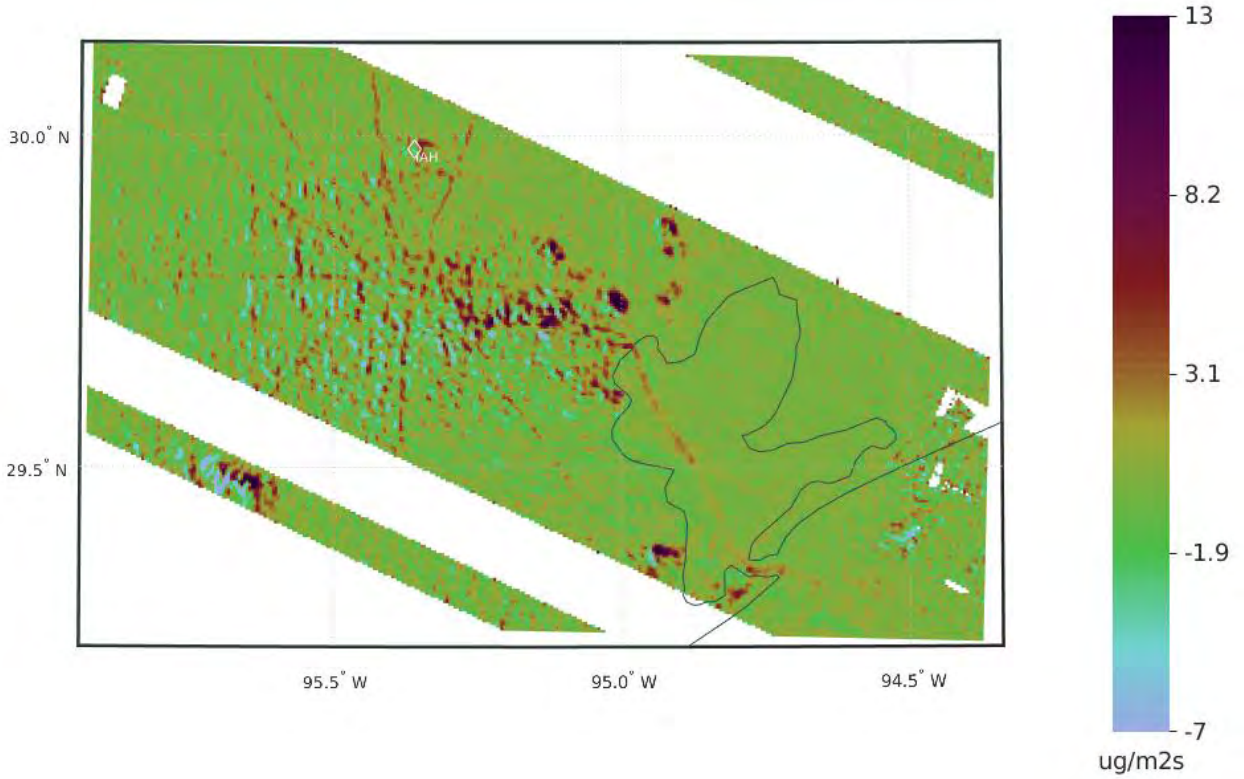


*Figure 2.4.5: Average flux divergence of GCAS $NO_2$ retrievals using CAMx air mass factors over Houston. White diamond shows the international airport (IAH).*

Figure 2.4.6 shows the flux divergence method applied to the CAMx simulations. In this case, the sources are known and so these simulations serve to evaluate the accuracy of the method. As can be seen, the method clearly recovers the main point and line sources used in the CAMx simulations.

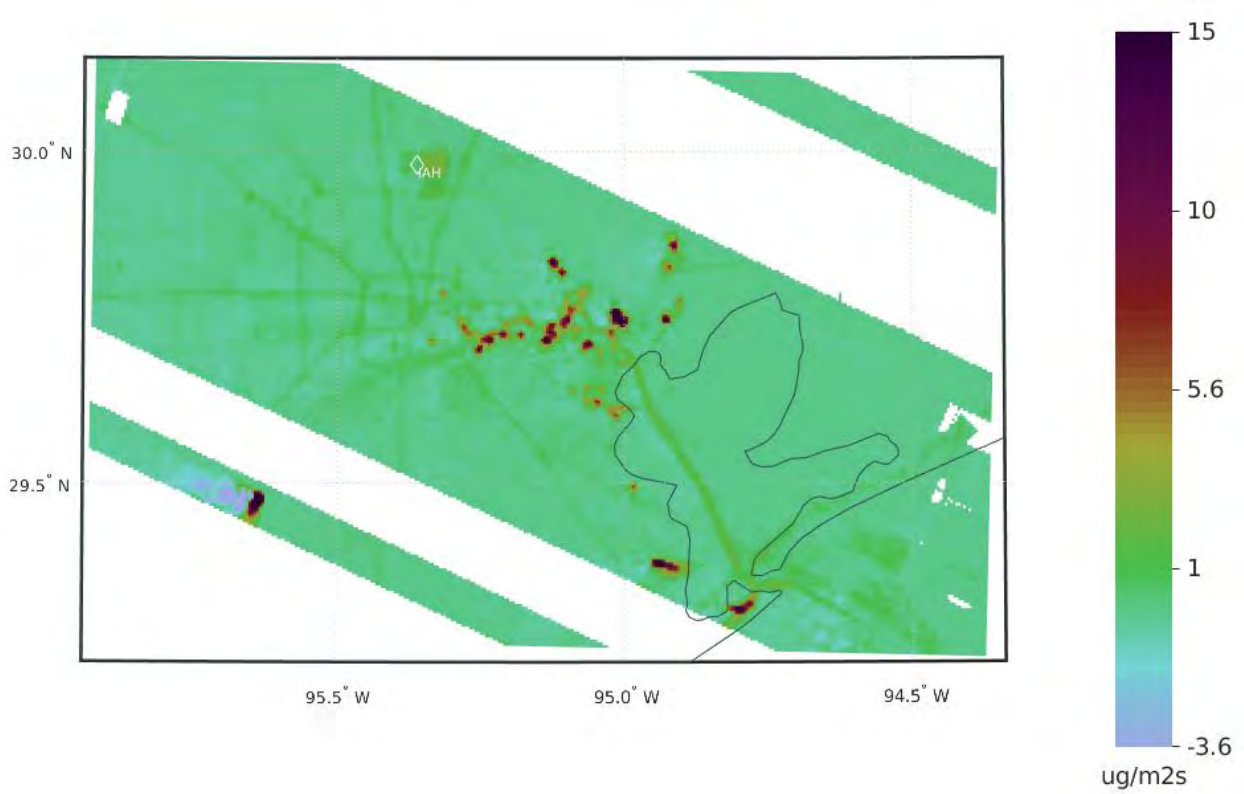


*Figure 2.4.6: Average flux divergence applied to CAMx $NO_2$ vertical column densities. White diamond shows the international airport.*

Figure 2.4.7 shows the ratio of the flux divergence using GCAS and using CAMx for the grid cells exceeding 0.2 ug-$m^2$-$s^{-1}$. Over the large point sources near the ship channel, the values are a mix of positive and negative values suggesting that the emissions inventory is relatively accurate in this location. Over highways, the values are large and positive suggesting that actual on-road emissions may be higher than in the current inventory. Over the ship paths, especially closer to the Gulf of Mexico, the values are negative suggesting that some of the ship $NO_X$ emissions may be overestimated in the inventory.

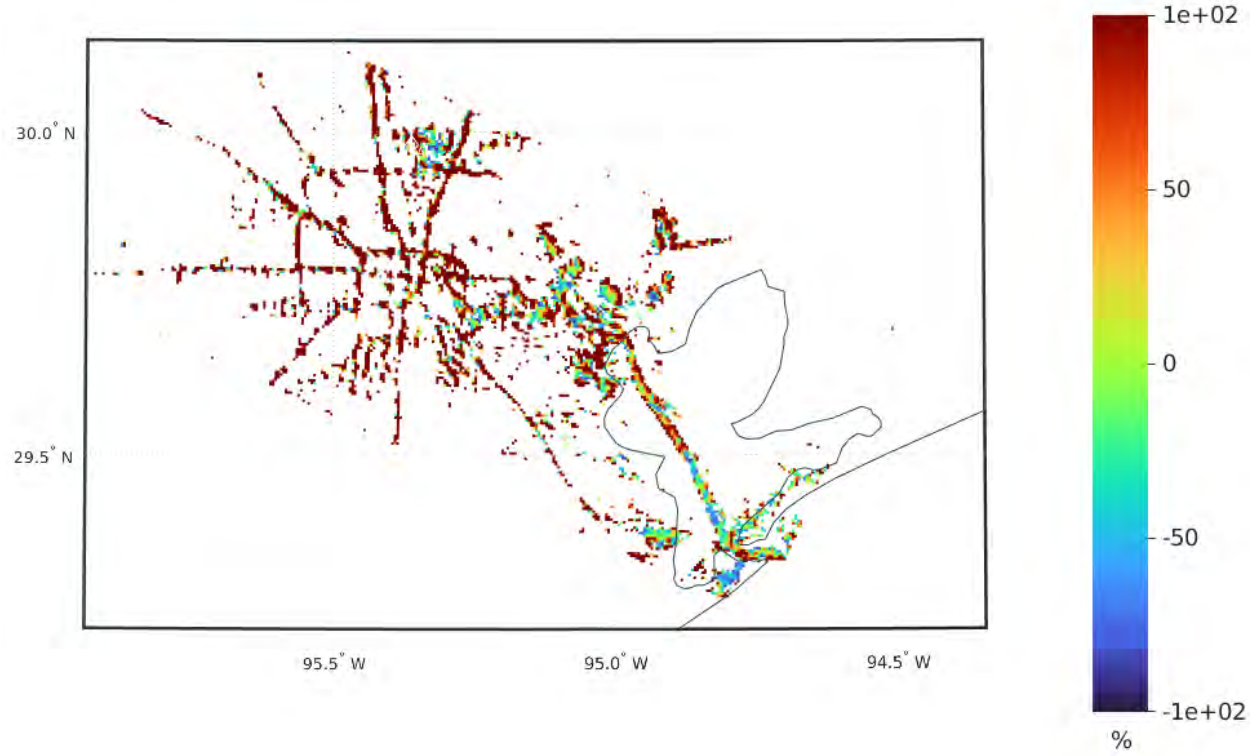


*Figure 2.4.7: Ratio of flux divergence of GCAS $NO_2$ columns and CAMx columns.*

## 2.5 Comparison of $NO_2$ and HCHO between model, aircraft, and satellite

### 2.5.1 Comparison of $NO_2$ between model, aircraft, and satellite

In this Task, we rigorously compared the CAMx model simulation to the variety of $NO_2$ observations available to better understand $NO_X$ emissions and modelled $NO_2$ dispersion. For comparisons of total column $NO_2$ between Pandora and CAMx, we apply a stratospheric component – originally from the TROPOMI measurements – to the CAMx simulation.

CAMx total vertical column $NO_2$ had the worst agreement ($r^2 = 0.25$) with the Pandora $NO_2$ column measurements and a normalized mean bias of –20.2%. The relatively low correlation could be related to the difficulty of identically simulating plume dispersion, especially dispersion related to the Gulf/Bay breeze. We found that small errors in the simulated wind direction (errors of 10° – 30°) could be responsible for the majority of the low correlation. On many of the days, the wind veered slightly over time usually less than 45° over the course of the daylight hours, but occasionally more than that. A 10° difference in the wind direction could be the difference between whether the Pandora measurement site was "hit" by a narrow $NO_2$ plume or avoided it altogether.

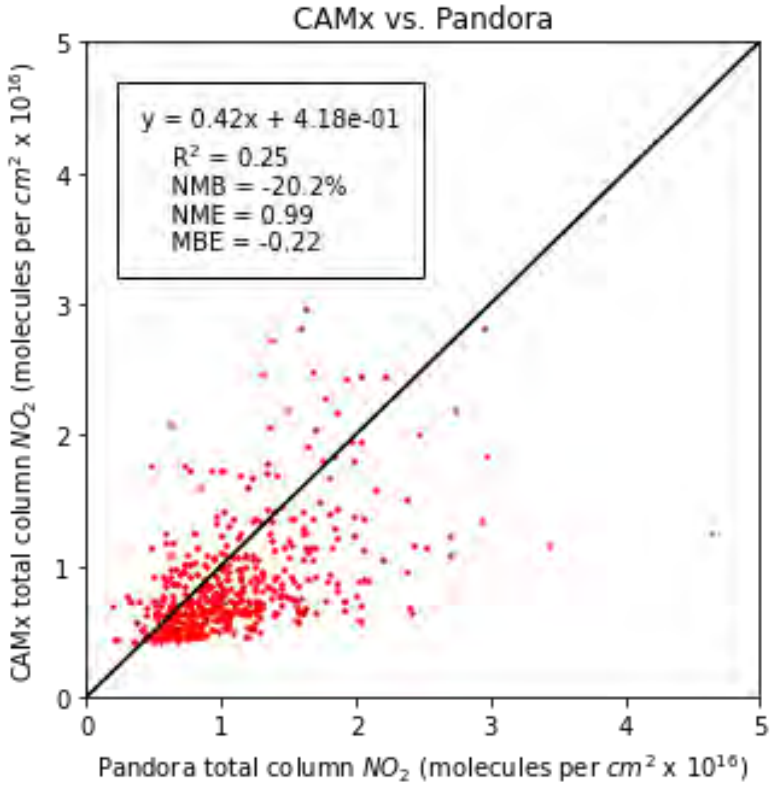


*Figure 2.5.1. CAMx total column $NO_2$ (stratospheric component added) vs. Pandora total column $NO_2$ matched to nearest hour.*

Some of the $NO_2$ low bias between CAMx and Pandora may be related to background $NO_2$, but since the background $NO_2$ in the Houston urban environment is a small fraction of the total column (an error of ~0.5 x $10^{15}$ molecules/$cm^2$, which is <10% in most cases), we do not think this is having a meaningful impact. Instead, we believe that a low CAMx $NO_2$ bias may be related to a $NO_X$ emissions underestimate from certain sectors of emissions. We further found that the bias between CAMx and Pandora is better on weekends (–5.8%) than during weekdays (–26.1%), suggesting that day of week emission profiles may need further investigation.

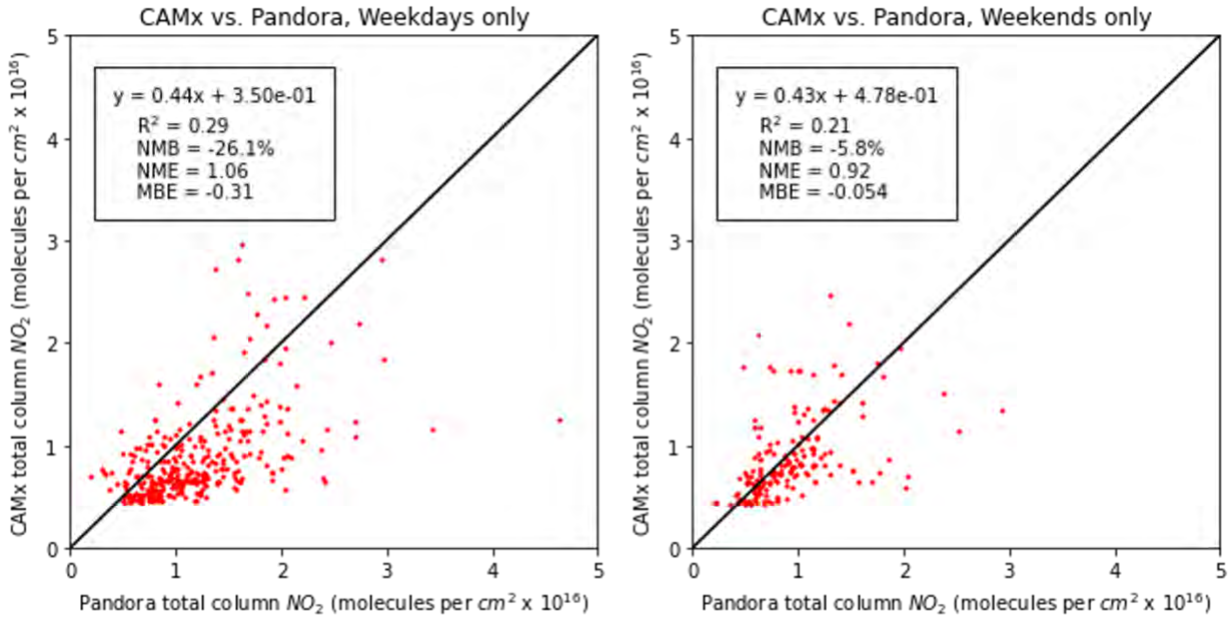


*Figure 2.5.2. CAMx total column $NO_2$ (stratospheric component added) vs. Pandora total column $NO_2$ matched to nearest hour, for (Left) weekdays and (Right) weekends.*

When doing a direct comparison between $NO_2$ columns from GCAS and CAMx during all collocations, CAMx has a normalized mean bias of –37.0%. The disagreements were largest in the downtown Houston area as shown in Figure 2.5.3.

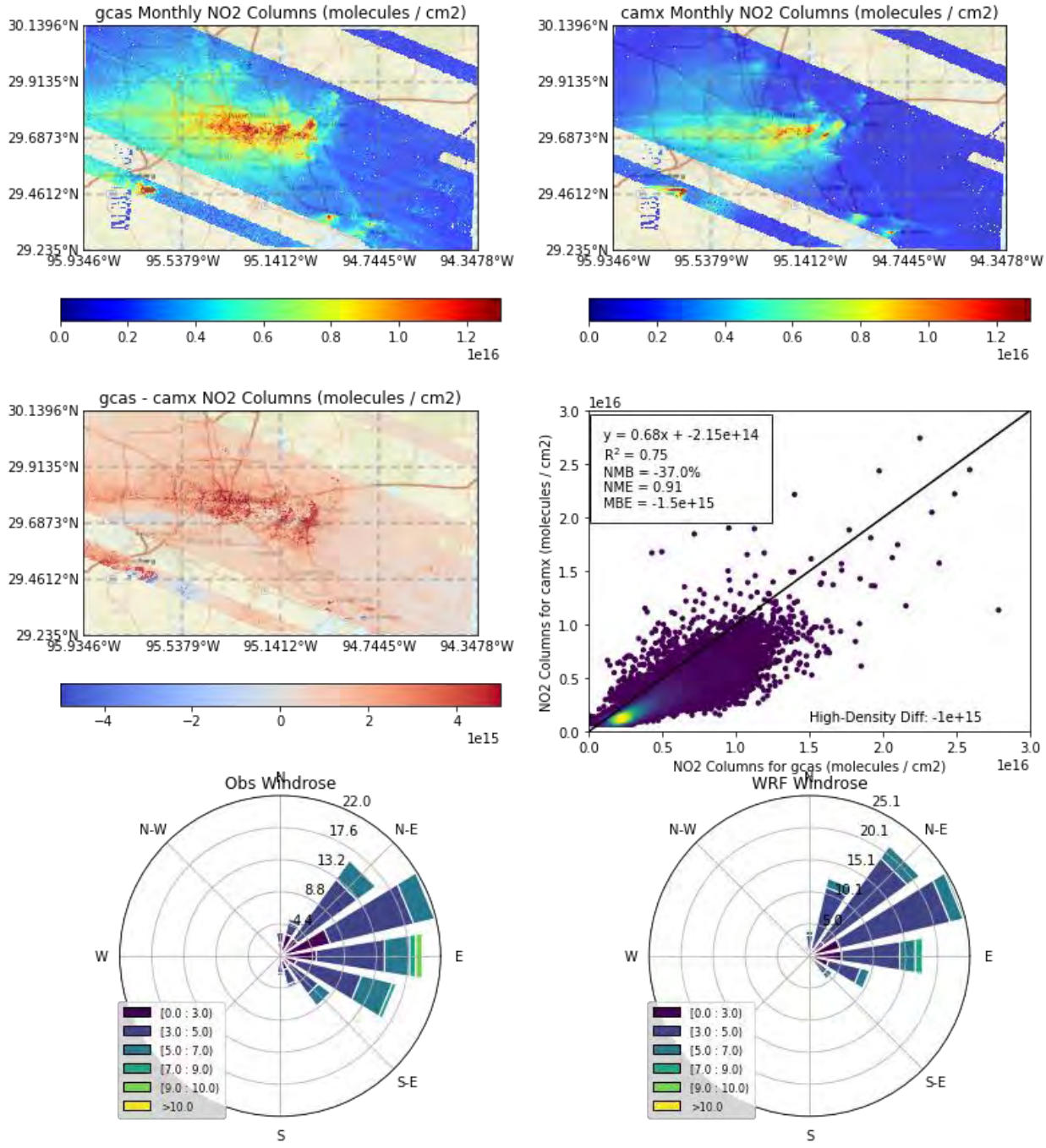


*Figure 2.5.3. (Top Left) GCAS monthly column $NO_2$ for all measurements compared to (Top Right) coincident $NO_2$ from CAMx. (Middle Left) Difference between GCAS and CAMx. (Middle Right) Scatterplot of CAMx vs. GCAS. (Bottom Left) Wind rose of NOAA surface observations compared to (Bottom Right) Wind rose from WRF at the same locations.*

In Appendix A, we show the daily comparisons for all 10 flight days. $NO_2$ column disagreements between GCAS and CAMx were largest on Wednesday September 8 and Thursday September 23, while agreement was best on Sunday September 26. The disagreements on September 8 and September 23 seem to further implicate missing $NO_X$ emissions in the downtown area as both days had northerly winds, and the point source plumes located on the east side of the metropolitan area did not overlap.

Further, the daily intercomparisons show that point source plumes tend to diffuse into wider plumes than simulated by CAMx. Addressing this shortcoming is beyond the scope of this project, but could be addressed by future work.

Next, we compare GCAS to CAMx in certain sections of the Houston metropolitan area. We compare GCAS to CAMx outside of the most $NO_2$ polluted zones of Houston. We find that there is a small but systematic low $NO_2$ bias in the CAMx simulation of -27.7%. This may be related to lightning $NO_X$ or some other long-range transport of $NO_2$. This systematic bias is often less than 10% of the total $NO_2$ column in the downtown Houston area.

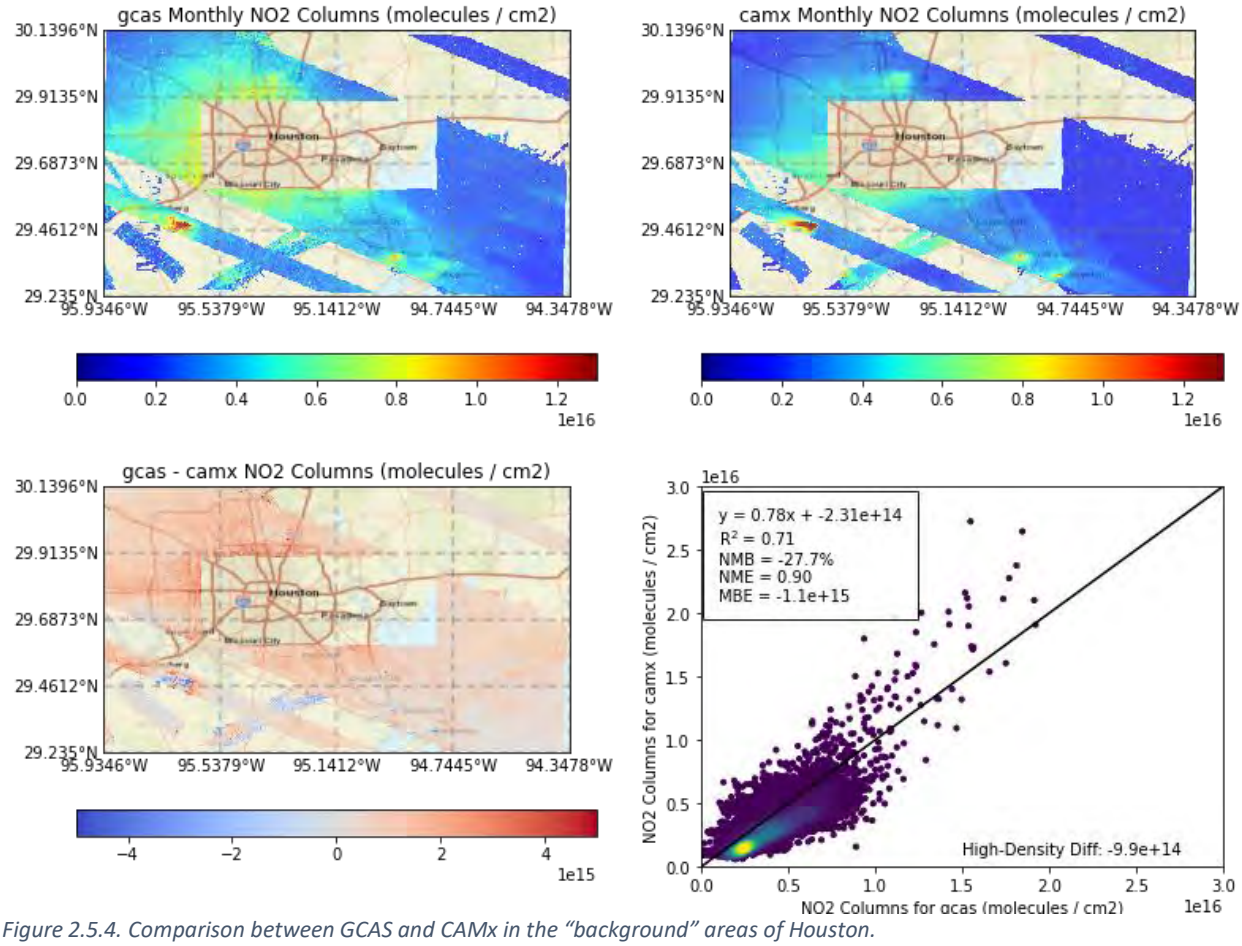


*Figure 2.5.4. Comparison between GCAS and CAMx in the "background" areas of Houston.*

We then compare GCAS and CAMx in the downtown area, while also filtering out $NO_2$ plumes from the point sources on the east side of the city. For this intercomparison, we find a large difference: GCAS is significantly larger than CAMx near downtown. This once again implicates missing $NO_X$ emission sources in the downtown area.

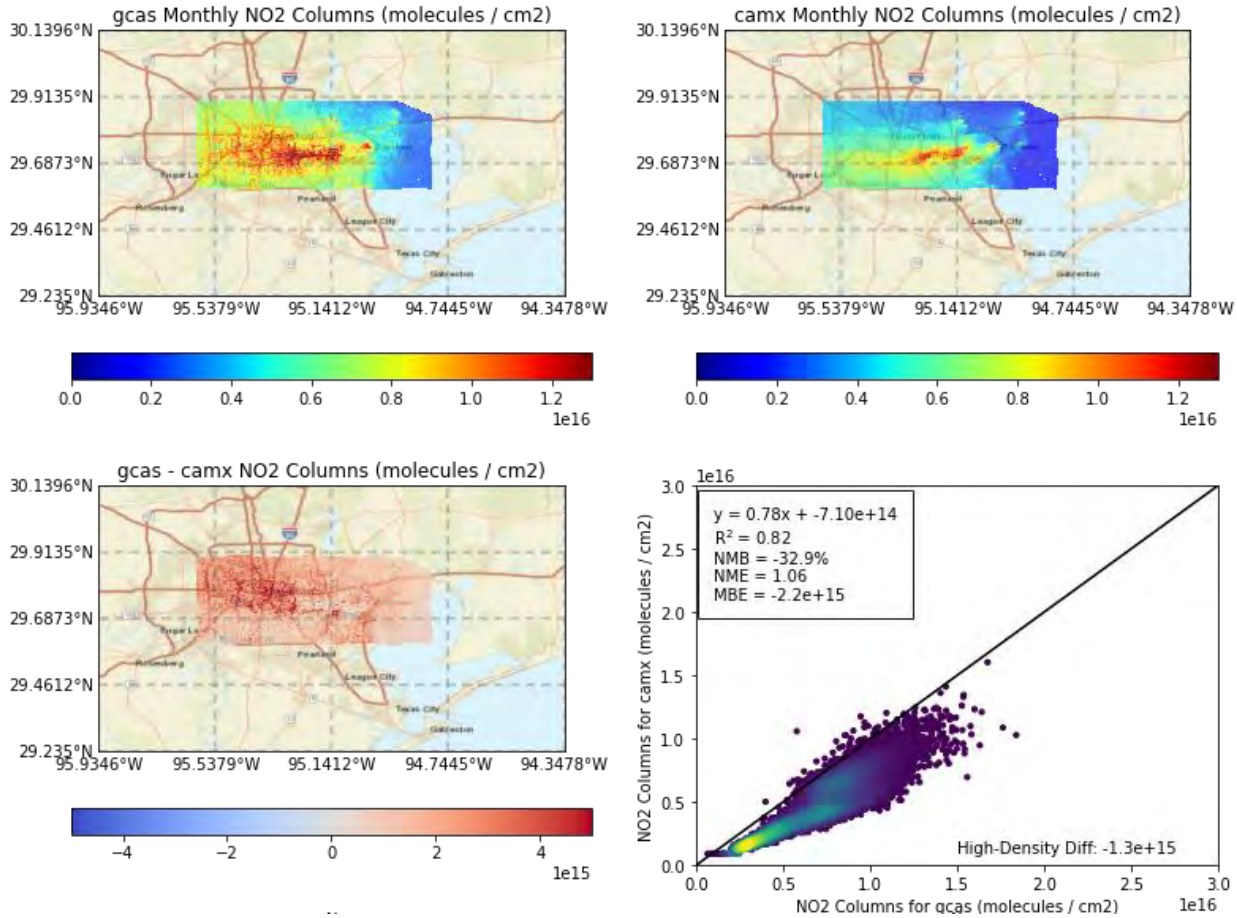


*Figure 2.5.5. Comparison between GCAS and CAMx in the "urban" areas of Houston.*

### 2.5.2 Comparison of HCHO between model, aircraft, and satellite

HCHO can be a good indicator of primary VOC emissions, and secondary ozone production. In this project, we qualitatively compared TROPOMI and CAMx to each other. CAMx outputs a "background" value of approximately 8 x $10^{15}$ molecules per $cm^2$ and a further ~1.5 x $10^{15}$ enhancement over the Houston metropolitan area. Qualitatively comparing to Pandora and TROPOMI – which is observing HCHO in the range of 10 – 20 x $10^{15}$ molecules per $cm^2$ – the CAMx HCHO values in the Houston metropolitan area seem marginally low and warrant further investigation. It is too early to determine whether the source of this difference would be biogenic or anthropogenic.

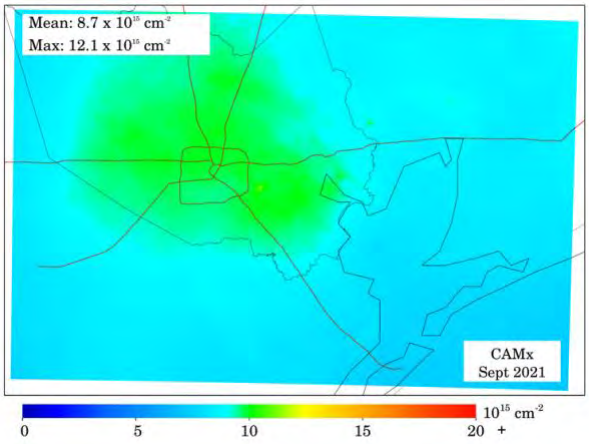


*Figure 2.5.6. CAMx column HCHO during September 2021.*

Unfortunately, TROPOMI cannot capture an urban HCHO enhancement which is likely originating from the Houston area. Quite simply, the TROPOMI HCHO measurement has too much instrument noise to be useful at the urban scale and over short timeframes, such as a single month. Instead TROPOMI HCHO is more useful for evaluating regional scale VOC emissions, such as those across all of eastern Texas and over seasonal timeframes (Goldberg et al., 2022). Future work could evaluate TROPOMI HCHO over longer timeframes.

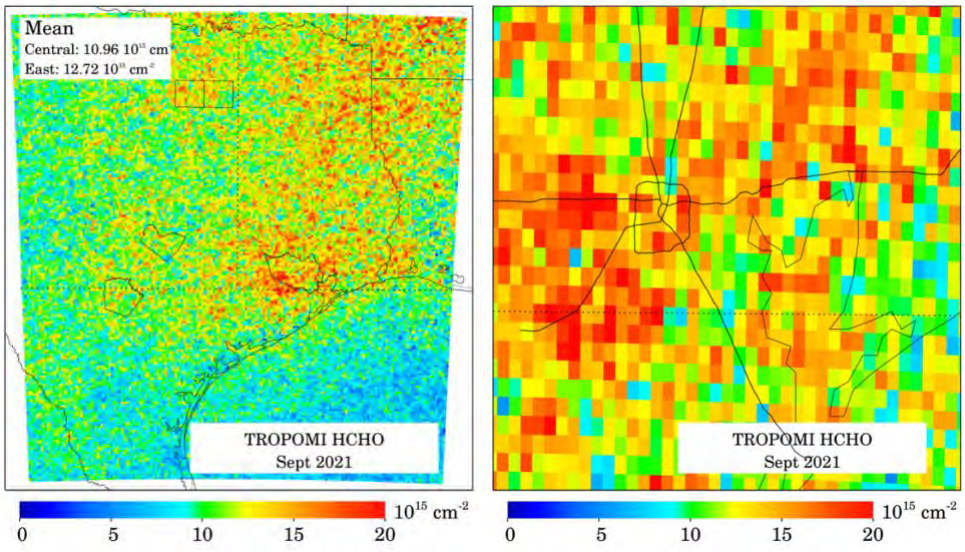


*Figure 2.5.7. TROPOMI HCHO during September 2021 for (Left) Texas and (Right) zoomed in to the Houston metropolitan area.*

## 2.6 Use of machine learning to estimate emission factors for individual sectors

Machine learning algorithms are being widely applied to estimate scaling factors for emission inventories. CAMx simulations were made in Source Apportionment mode to separate the $NO_2$ Vertical Column Densities associated with each of 17 sectors. The CAMx model configuration is described in Section 2.1.

A Multi-Linear Regression (MLR) model was built to estimate the optimal combination of individual CAMx sectors that would best match the GCAS $NO_2$ retrievals. In practice, some of the emission sources in OSAT are too close together to be able to be clearly distinguished form each other. We therefore merged the following: 1. Channelview Cogeneration Facility and Odyssey Energy Altura Cogen, LLC; 2. Deer Park Energy Center and Pasadena Power Plant; 3. Texas City Cogeneration, South Houston Green Power Site, and the "Other" category. We applied the MLR model to the entire field campaign, and we also performed simulations separately for weekdays and for weekends.

In seeking an optimal match to the GCAS columns, it is important to apply a regularization term to prevent unphysical results (de Foy et al., 2015). The regularization term imposes a cost on the departure of the posterior emissions from the prior emissions. The algorithm then balances the cost in the change of the emissions with the cost of the mismatch between the GCAS retrievals and the sum of the scaled fields from the source apportionment simulations. We assume as a prior that all scaling factors are 1.

Our first sensitivity test is on the value of the regularization term, as shown in Figure 2.6.1. The top panel shows the variation of the estimated scaling factors. The bottom panel shows the cost function and the change in the correlation factor between the GCAS retrievals and the MLR model results. When the regularization term is 1000 (or higher), the cost of departing from the prior is too high and the model returns only scaling factors of 1. This is the "do nothing" model. When the regularization term is 1 or lower, the cost on the scaling factors is irrelevant and the model scaling factors grow so long as they make even the tiniest increase in the correlation. This is the "do anything at any cost" model. In between these two extremes, we have smoothly varying scaling factors, and we need to identify criteria for selecting the appropriate regularization factor. In this work, we chose a value of 25, shown in Figure 2.6.1, which balances the desire to maximize the improvements in the model (lower Grid Residuals) while minimizing the departure from the prior (lower Emission Residuals). By selecting this value, we achieve most of the improvements in the correlation coefficient of the model without ending up with unrealistic scaling factors.

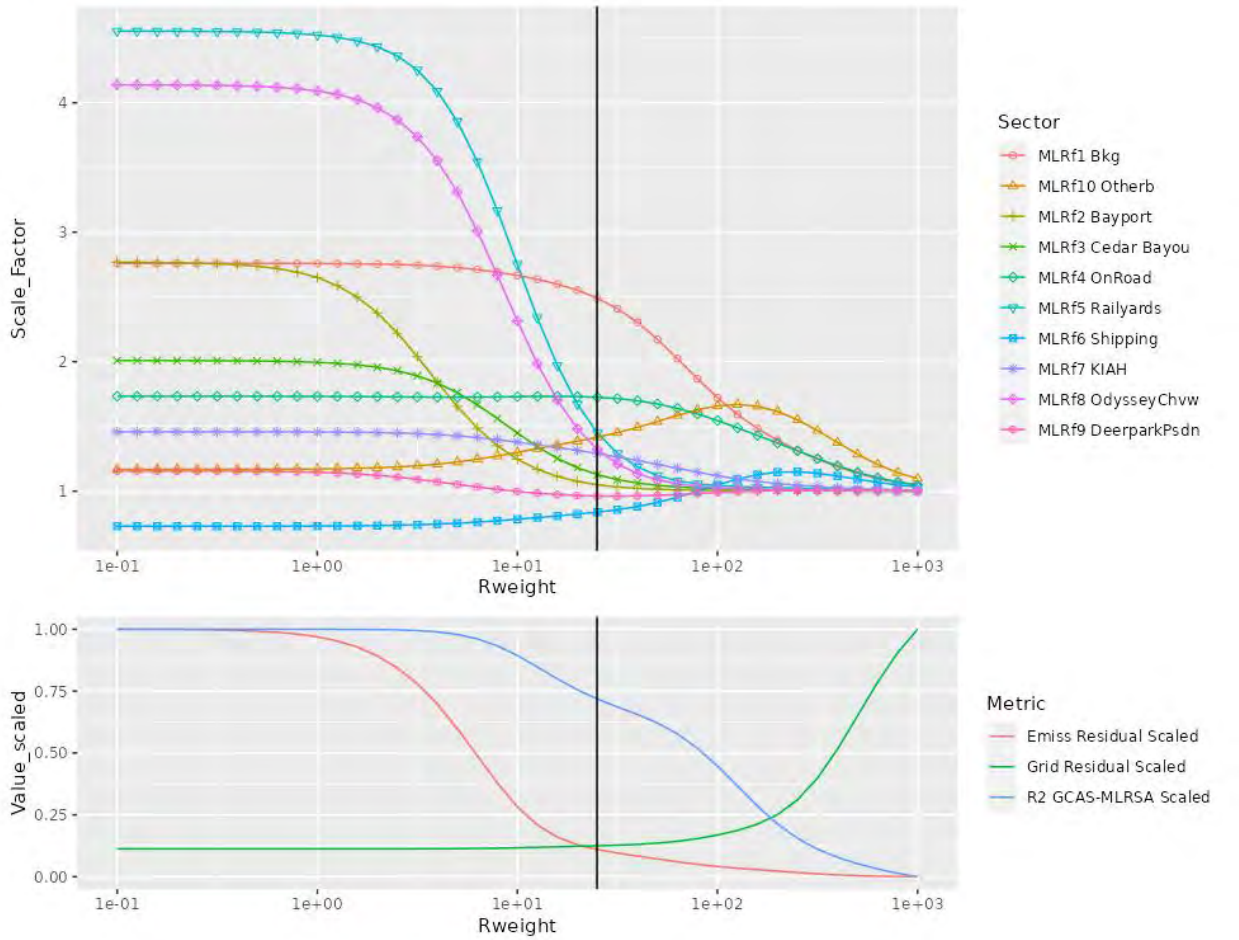


*Figure 2.6.1. Top: Scaling factors on CAMx source sectors as a function of the regularization term (Rweight). Bottom: Cost function of the emission term and the gridded residual, along with scaled $r^2$ value of the GCAS retrievals with the reconstituted Multi Linear Regression model. The black vertical line indicates the regularization term selected for this study.*

We performed an uncertainty analysis using bootstrapping on two different levels. The most important level for bootstrapping was randomly selecting, with replacement, the GCAS rasters included in the optimization. For the full time series, there were 27 rasters. In addition to performing the simulations for these 27 rasters, we performed 100 simulations with random selections of the 27 rasters. The second level for bootstrapping was to randomly select grid blocks for use in the analysis. We randomly select 7 x 7 blocks of cells within the CAMx grid cells and include them until we have the same number of points as in the initial grid. We did this 100 times for each selection of rasters, leading to a total of 10,000 simulations.

The scaling factors for each source sector are shown as boxplots in Figure 2.6.2 for weekdays and for weekends. There were 19 rasters on weekdays and 8 rasters on weekends, which explains the somewhat larger uncertainty on weekends: any particular raster would have a larger influence and therefore its absence, or conversely its multiple inclusion, would have a larger impact on the scaling factors.

The boxplot suggests that the $NO_2$ background concentration is underestimated by CAMx and is consistent with findings in Task 5. The boxplot also shows that on-road mobile emissions may be underestimated in the model. This may also be true for railyard emissions. In contrast, the shipping emissions may be overestimated, though it should be noted from Figure 2.6.1 that the sign of the shipping adjustment changes with the regularization factor. The EGU point sources are close to a scale factor of one, especially Bayport and Cedar Bayou, which is expected given the use of emissions obtained from CAMPD measurements. The "Other" sources are underestimated, although this factor is particularly sensitive to the regularization factor.

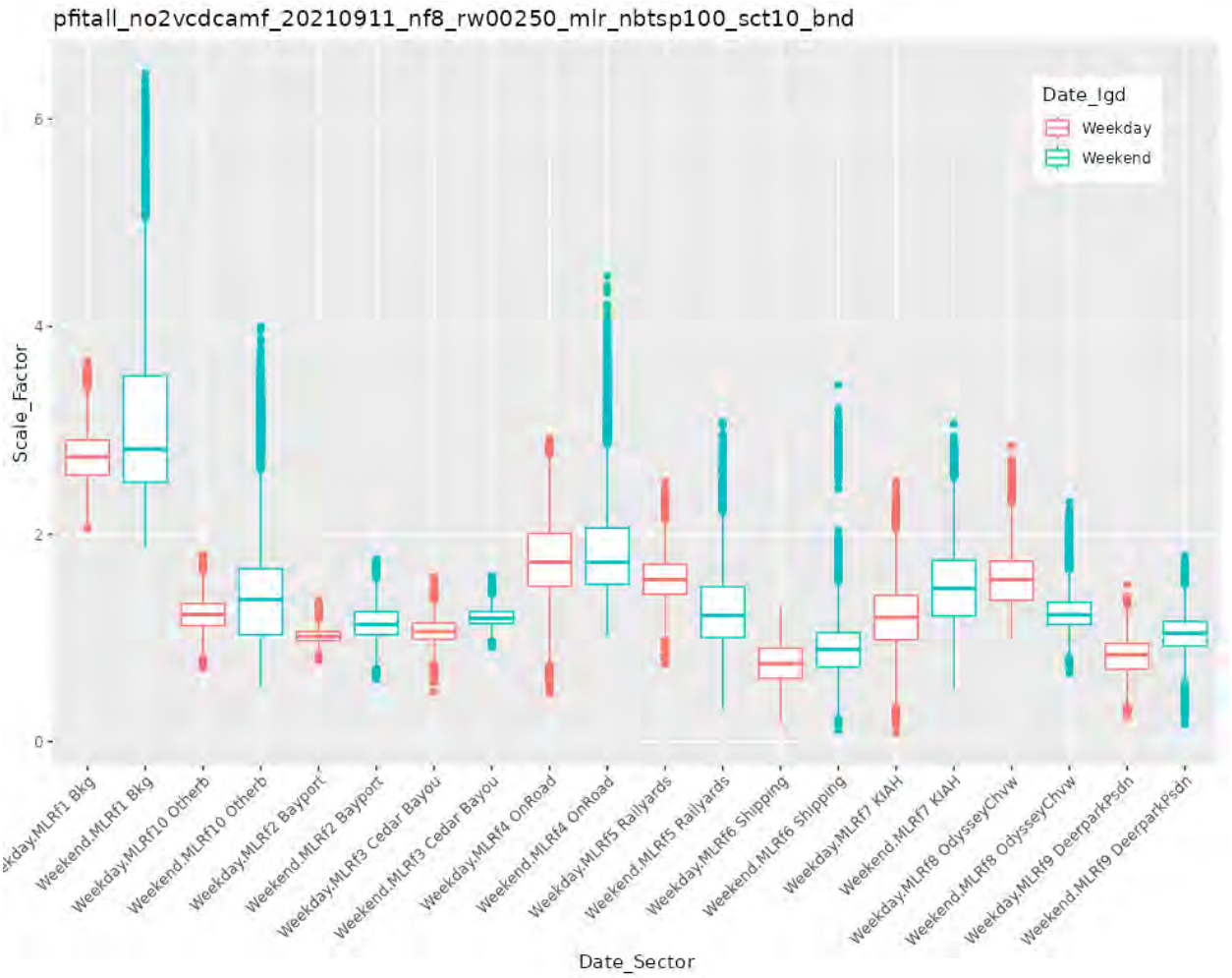


*Figure 2.6.2: Boxplot of scaling factors obtained from the Multi Linear Regression Model with 100 bootstrapped selection of rasters and 100 bootstrapped selection of grid blocks to include in the analysis.*

Figures 2.6.3 and 2.6.4 show the CAMx column $NO_2$ as well as the adjusted MLR Source Apportionment column $NO_2$. The latter has a better representation of the sources over the Houston urban area. The top row in each figure shows the total $NO_2$ VCDs, while the remaining rows display the sectoral components. In Figure 2.6.3, we show the following emission sectors: on-road mobile, railyards and shipping emissions. In Figure 2.6.4, we show "Points" (sum of all sectors not plotted separately: Bayport, Cedar Bayou, KIAH, Odyssey and Channelview, Deer Park and Pasadena), background, other). This shows how each sector contributes to the total column $NO_2$ and gives an impression of how the spatial distributions of the different sectors contribute to the overall distribution of $NO_2$ columns over Houston.

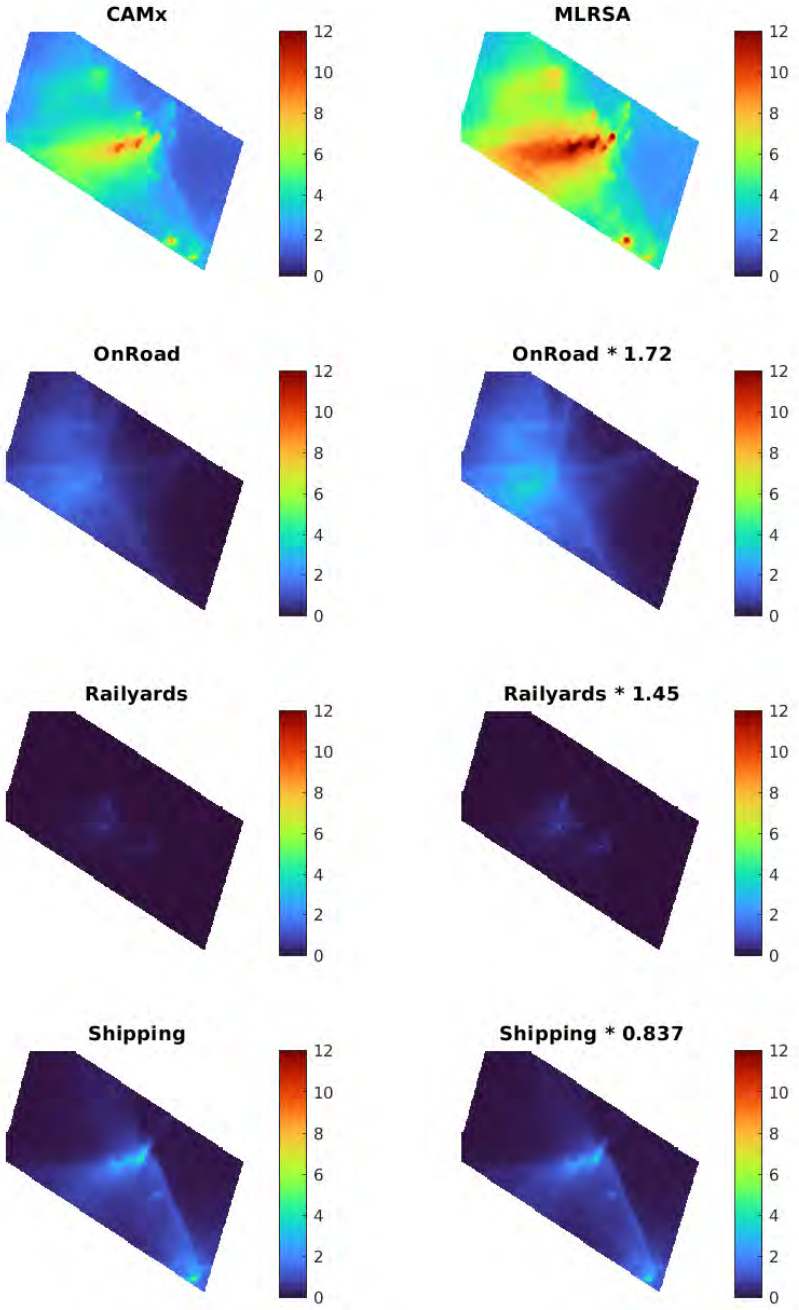


*Figure 2.6.3: CAMx and MLR Source Apportionment $NO_2$ Vertical Column Densities (VCD) along with contribution from different sectors: Left: CAMx default, Right: MLR Adjusted values.*

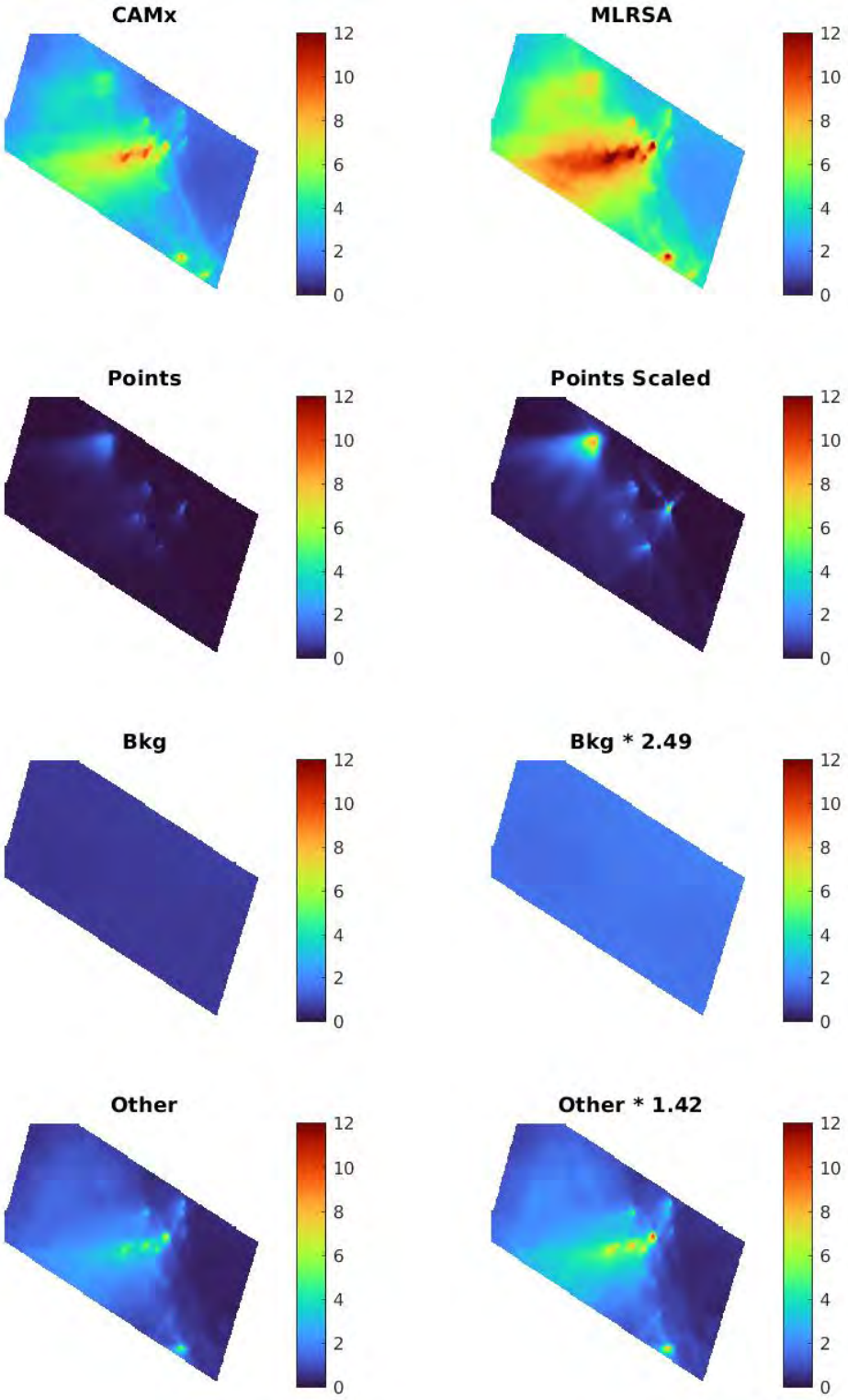


*Figure 2.6.4: CAMx and MLR Source Apportionment $NO_2$ Vertical Column Densities (VCD) along with contribution from different sectors: Left: CAMx default, Right: MLR Adjusted values. (Same as previous figure but for different sectors. "Points" is the sum of all sectors not plotted separately: Bayport, Cedar Bayou, KIAH, Odyssey and Channelview, Deer Park and Pasadena.*

The spatial data in Figures 2.6.3 and 2.6.4 can be summed over different domains to get a more quantitative measure of the contribution of each sector, as shown in Figure 2.6.5 for both the CAMx simulations and the MLR Source Apportionment model. The first 3 sets of bars are for the entire domain, with the contributions for the grid cells that have $NO_2$ VCD below average (prc-50), all grid cells (prc0) and the grid cells above average only (prc50). The other domains are calculated as the grid cells where the NO2 VCD contribution of each sector is 90% of the 99% percentile (i.e., to get the threshold, you calculate the 99% of the columns from that sector alone and multiply by 0.90). As an example, consider IAH: The algorithm selects only the grid cells above the airport. For those cells, the airport itself contributes around 30% of the $NO_2$ columns. This shows that overall, the background and "Other" term are the main contributors to the $NO_2$ columns, with shipping and on-road mobile emissions contributing somewhat smaller amounts. Point sources have relatively low impacts, even for the cells close to the sources.

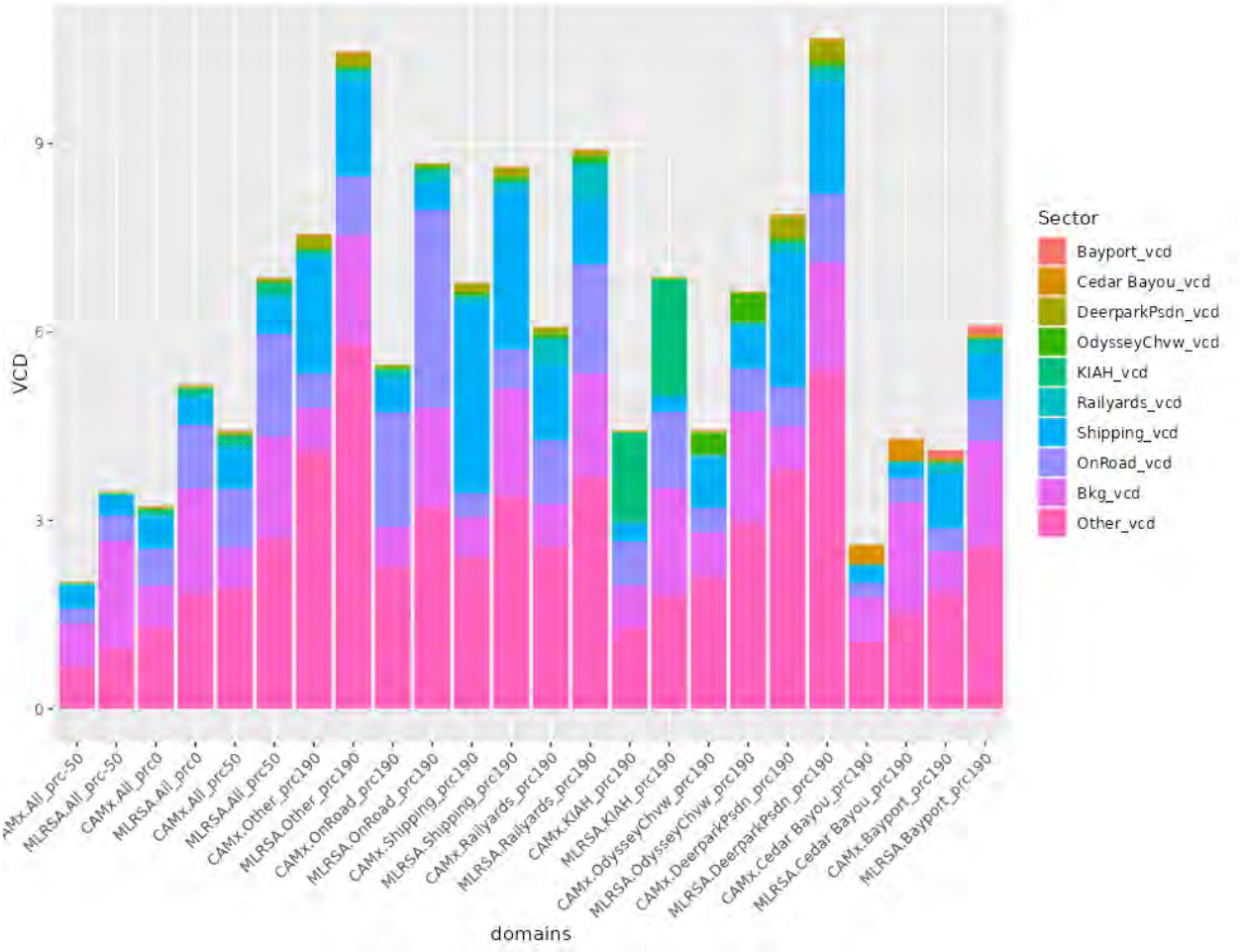


*Figure 2.6.5. Sector contribution to $NO_2$ Vertical Column Densities of the Multi Linear Regression model for domains of each sector.*

# 3.0 CONCLUSIONS AND RECOMMENDATIONS FOR FUTURE WORK

The TRACER-AQ field campaign provided an unprecedented opportunity to compare and validate multiple observation platforms and model simulations. In this project, we take a close look at $NO_2$ observations and simulations during this campaign to better understand where there may be shortcomings in the $NO_X$ modeling emissions inventory.

## 3.1 Summary of Findings

In this project, we were able to conduct a thorough analysis of $NO_2$ during the TRACER-AQ campaign. We found column $NO_2$ from GCAS to have excellent agreement with Pandora measurements ($r^2$=0.81 and NMB of +2.4%). Column $NO_2$ from TROPOMI had good correlation with Pandora ($r^2$=0.62), but there was a low bias that was not resolved when a CAMx-based air mass factor was used (–11%). When comparing TROPOMI to GCAS, it appears that the TROPOMI low bias might be worse than indicated by the Pandora comparison (–37%); future TROPOMI algorithm updates and future satellite missions with smaller pixel sizes may resolve this low bias. Column $NO_2$ from CAMx showed a substantial low bias when compared with Pandora (–20%) and GCAS measurements (–37%). Through a machine learning model, we were able to isolate on-road, railyard, and "other" $NO_X$ emissions as the likeliest cause of this low bias; agreement between model and measurements on the weekend days was better. Our analyses were primarily conducted using column $NO_2$ instead of surface $NO_2$ to diagnose $NO_X$ emissions since vertical mixing can be a source of error in a surface-only comparison. Summary of findings separated by task are described below:

Task 1:

- WRF and CAMx have been run at high spatial resolution (444 × 444 $m^2$)
- CAMx achieves the goal benchmark for MDA8 ozone NMB (-2.5%), while the NME (15.0%) is just outside the goal benchmark.
- CAMx surface $NO_2$ disagreements at CAMS monitors (NMB of –59.1% and NME of 62.3%), which we partially attribute to the difficulty of capturing hourly and near-road variability.

Task 2:

- GCAS aircraft-based measurements acquired fine-scale structure of urban $NO_2$; $NO_2$ plumes from highways, ships, point sources can be seen in isolation.
- GCAS column $NO_2$ has excellent agreement with Pandora $NO_2$ ($r^2$=0.80 and NMB of +6.3%)
- Using CAMx to re-process the AMF for GCAS gave marginal improvement to already excellent agreement (now $r^2$=0.81 and NMB of +3.2%)

Task 3:

- Satellite $NO_2$ has great correlation with Pandora measurements ($r^2$=0.62) and a small but important low bias (–11.7%). Low bias was not appreciably improved when using a CAMx-based air mass factor (–11.2%).
- Satellite $NO_2$ has a more substantial low bias when compared to GCAS (–37%) – that may improve with future algorithm updates, and possibly will only be improved with higher resolution pixels, such as TEMPO.

Task 4:

- EMG fit matched CAMPD $NO_X$ emissions for the W.A. Parish Power Plant within reasonable uncertainty (+/-20%).
- $NO_X$ emissions appear to be underestimated by –45% in Baytown on September 8, 2021; no conclusive evidence of whether this extends to other days.
- The FD method was able to distinguish the linear shape of major highways, many of the large point sources, and the Galveston Bay ship track.
- $NO_2$ Flux divergence comparison between CAMx and GCAS shows underestimates at highway locations.

Task 5:

- CAMx versus Pandora column $NO_2$ intercomparison showed a low bias in CAMx (–20.2%)
- CAMx versus GCAS column $NO_2$ intercomparison, which has a larger spatial footprint, showed larger $NO_2$ underestimates (–37%) and especially in downtown Houston.
- $NO_2$ model performance was worse on weekdays than weekends, implicating a weekday emissions source as the source of the disagreement.
- GCAS HCHO and Pandora HCHO have strong correlation. May be a low HCHO bias in CAMx but cannot disentangle whether source of disagreement is biogenic or anthropogenic.

Task 6:

- MLR confirms that on-road mobile and railyard $NO_X$ during weekdays may be underestimated, followed by weekend KIAH airport sources.

## 3.2 Recommendations for Future Work

- Investigate biases found for on-road and port (rail, airport, shipping) NOx emissions in a new CAMx simulation, while also accounting for the different weekday/weekend biases. Is there better agreement between observations and CAMx when $NO_X$ emissions are increased?
- Investigating the cause of the low bias in TROPOMI over Houston. Is this related to pixel size or something else? Are biases less in the NASA algorithm? Does TEMPO observe the same patterns as GCAS and TROPOMI? It will be important to fully account for the TROPOMI low bias in any future model/TROPOMI intercomparisons.
- Use TROPOMI to investigate $NO_2$ over longer timeframes. Are similar patterns seen? Are spatial $NO_2$ trends consistent with the $NO_X$ inventory trends?
- More upper tropospheric measurements and measurements outside of urban locations are needed to better constrain GCAS and TROPOMI in the less polluted areas of Texas. Performance of GCAS outside of urban areas is largely unvalidated.
- Further analysis of HCHO. Do anthropogenic VOC emissions need to be increased? If VOC emissions need to be modified, how does this affect the $NO_2$ lifetime, model $NO_2$ intercomparison, and $O_3$ model performance?

# 4.0 AUDITS OF DATA QUALITY

We performed Quality Assurance/Quality Control (QA/QC) procedures in accordance with the Quality Assurance Project Plan (QAPP) completed at the beginning of this project. Per requirements for Category III projects, we performed data audits on at least 10% of the data sets. In this section, we report the results of our QA/QC.

## 4.1 CAMx simulations

The WRF-CAMx model was run by Ramboll. Validation of WRF-CAMx modeling with the NRTEEM platform is described by Johnson et al. (2020) and subsequently used in Goldberg et al. (2022). Ambient $NO_2$ concentrations simulated by the WRF-CAMx modeling were compared with all available ground-based observations of $NO_2$ during the modeling time period, as detailed in Section 2.1.

## 4.2 GCAS screening

We used all GCAS data where the cloud glint flag did not equal 1.0. This screened out pixels with optically thick clouds.

## 4.3 TROPOMI screening

We used all TROPOMI data where the quality assurance flag was greater than 0.75. This screened out pixels with optically thick clouds.

## 4.4 EMG Analysis

The EMG technique (Goldberg et al., 2022; Goldberg, Lu, Streets, et al., 2019) was selected for its ability to produce emission estimates directly from TROPOMI data with minimal additional data. Calculation of parameters in the EMG approach are based on wind speed and direction, which were taken from the Ramboll WRF simulations at 444 x 444 $m^2$. We also applied the EMG technique using widely available re-analysis data, the ECMWF ERA-5 (Hersbach et al., 2020) for the purpose of anticipating how using re-analysis data (rather than WRF simulations) may influence the EMG analysis in the future if WRF simulations are not available. We focused on the meteorological parameter that EMG uses, wind speed. We found the $NO_X$ emissions that resulted from using the two different wind speed datasets were within 20%. Therefore, wind speed may contribute up to a third of the total uncertainty of the EMG method (~60%).

**References**


Beirle, S., Boersma, K. F., Platt, U., Lawrence, M. G., & Wagner, T. (2011). Megacity Emissions and Lifetimes of Nitrogen Oxides Probed from Space. *Science*, *333*(6050), 1737–1739. https://doi.org/10.1126/science.1207824

Beirle, S., Borger, C., Dörner, S., Li, A., Hu, Z., Liu, F., et al. (2019). Pinpointing nitrogen oxide emissions from space. *Science Advances*, *5*(11), eaax9800. https://doi.org/10.1126/sciadv.aax9800

Beirle, S., Borger, C., Dörner, S., Eskes, H. J., Kumar, V., De Laat, A., & Wagner, T. (2021). Catalog of NOx emissions from point sources as derived from the divergence of the NO2 flux for TROPOMI. *Earth Syst. Sci. Data*, *13*, 2995–3012. https://doi.org/10.5194/essd-13-2995-2021

Beirle, S., Borger, C., Jost, A., & Wagner, T. (2023). Improved catalog of NOx point source emissions (version 2). *Earth System Science Data*, *15*(7), 3051–3073. https://doi.org/10.5194/essd-15-3051-2023

Emery, C., Liu, Z., Russell, A. G., Odman, M. T., Yarwood, G., & Kumar, N. (2017). Recommendations on statistics and benchmarks to assess photochemical model performance. *Journal of the Air and Waste Management Association*, *67*(5), 582–598. https://doi.org/10.1080/10962247.2016.1265027

de Foy, B., Cui, Y. Y., Schauer, J. J., Janssen, M., Turne, J. R., & Wiedinmyer, C. (2015). Estimating sources of elemental and organic carbon and their temporal emission patterns using a least squares inverse model and hourly measurements from the St. Louis-Midwest supersite. *Atmospheric Chemistry and Physics*, *15*(5), 2405–2427. https://doi.org/10.5194/acp-15-2405-2015

de Foy, Benjamin, & Schauer, J. J. (2022). An improved understanding of NOx emissions in South Asian megacities using TROPOMI NO2 retrievals. *Environmental Research Letters*, *17*(2), 024006. https://doi.org/10.1088/1748-9326/ac48b4

de Foy, Benjamin, Lu, Z., Streets, D. G., Lamsal, L. N., & Duncan, B. N. (2015). Estimates of power plant NOx emissions and lifetimes from OMI NO2 satellite retrievals. *Atmospheric Environment*, *116*(2), 1–11. https://doi.org/10.1016/j.atmosenv.2015.05.056

Goldberg, D. L., Lu, Z., Streets, D. G., de Foy, B., Griffin, D., McLinden, C. A., et al. (2019). Enhanced Capabilities of TROPOMI NO2: Estimating NOx from North American Cities and Power Plants. *Environmental Science & Technology*, *53*(21), 12594–12601. https://doi.org/10.1021/acs.est.9b04488

Goldberg, D. L., Lu, Z., Oda, T., Lamsal, L. N., Liu, F., Griffin, D., et al. (2019). Exploiting OMI NO2 satellite observations to infer fossil-fuel CO2 emissions from U.S. megacities. *Science of The Total Environment*, *695*, 133805. https://doi.org/10.1016/j.scitotenv.2019.133805

Goldberg, D. L., Anenberg, S. C., Lu, Z., Streets, D. G., Lamsal, L. N., E McDuffie, E., & Smith, S. J. (2021). Urban NOx emissions around the world declined faster than anticipated between 2005 and 2019. *Environmental Research Letters*, *16*(11), 115004. https://doi.org/10.1088/1748-9326/ac2c34

Goldberg, D. L., Harkey, M., de Foy, B., Judd, L., Johnson, J., Yarwood, G., & Holloway, T. (2022). Evaluating NOx emissions and their effect on O3 production in Texas using TROPOMI NO2

and HCHO. *Atmospheric Chemistry and Physics*, *22*(16), 10875–10900. https://doi.org/10.5194/acp-22-10875-2022

Guenther, A. B., Jiang, X., Heald, C. L., Sakulyanontvittaya, T., Duhl, T., Emmons, L. K., & Wang, X. (2012). The model of emissions of gases and aerosols from nature version 2.1 (MEGAN2.1): An extended and updated framework for modeling biogenic emissions. *Geoscientific Model Development*, *5*(6), 1471–1492. https://doi.org/10.5194/gmd-5-1471-2012

Hersbach, H., Bell, B., Berrisford, P., Hirahara, S., Horányi, A., Muñoz-Sabater, J., et al. (2020). The ERA5 global reanalysis. *Quarterly Journal of the Royal Meteorological Society*, *146*(730), 1999–2049. https://doi.org/10.1002/qj.3803

Holloway, T., Harkey, M., Kim, E., Johnson, J., Yarwood, G., & Goldberg, D. L. (2021). *New Satellite Tools to Evaluate Emission Inventories: Is a 3-D Model Necessary? rAQRP Project 20-020*.

Janz, S., Kowalewski, M. G., Lamsal, L. N., Nowlan, C., & Judd, L. M. (2019). Airborne hyperspectral trace gas sensors as testbeds for geostationary air quality missions. In S. P. Neeck, T. Kimura, & P. Martimort (Eds.), *Sensors, Systems, and Next-Generation Satellites XXIII* (Vol. 11151, p. 86). SPIE. https://doi.org/10.1117/12.2533765

Johnson, J., Shah, T., & Yarwood, G. (2020). *Near-Real Time Exceptional Event Modeling Final Report*. Retrieved from https://ramboll.com

Kuhlmann, G., Chan, K. L., Donner, S., Zhu, Y., Schwaerzel, M., Dörner, S., et al. (2022). Mapping the spatial distribution of NO2 with in situ and remote sensing instruments during the Munich NO2 imaging campaign. *Atmospheric Measurement Techniques*, *15*(6), 1609–1629. https://doi.org/10.5194/AMT-15-1609-2022

Lu, Z., Streets, D. G., de Foy, B., Lamsal, L. N., Duncan, B. N., & Xing, J. (2015). Emissions of nitrogen oxides from US urban areas: Estimation from Ozone Monitoring Instrument retrievals for 2005-2014. *Atmospheric Chemistry and Physics*, *15*(18), 10367–10383. https://doi.org/10.5194/acp-15-10367-2015

McDonald, B. C., Dallmann, T. R., Martin, E. W., & Harley, R. A. (2012). Long-term trends in nitrogen oxide emissions from motor vehicles at national, state, and air basin scales. *Journal of Geophysical Research: Atmospheres*, *117*(D21), n/a-n/a. https://doi.org/10.1029/2012JD018304

McDonald, B. C., Gentner, D. R., Goldstein, A. H., & Harley, R. A. (2013). Long-Term Trends in Motor Vehicle Emissions in U.S. Urban Areas. *Environmental Science & Technology*, *47*(17), 10022–10031. https://doi.org/10.1021/es401034z

Meier, A. C., Schönhardt, A., Bösch, T., Richter, A., Seyler, A., Ruhtz, T., et al. (2017). High-resolution airborne imaging DOAS measurements of NO<sub>2</sub> above Bucharest during AROMAT. *Atmospheric Measurement Techniques*, *10*(5), 1831–1857. https://doi.org/10.5194/amt-10-1831-2017

Nowlan, C. R., Liu, X., Janz, S. J., Kowalewski, M. G., Chance, K. V., Follette-Cook, M. B., et al. (2018). Nitrogen dioxide and formaldehyde measurements from the GEOstationary Coastal and Air Pollution Events (GEO-CAPE) Airborne Simulator over Houston, Texas. *Atmospheric Measurement Techniques*, *11*(11), 5941–5964. https://doi.org/10.5194/amt-11-5941-2018

Skamarock, W. C., Klemp, J. B., Dudhia, J., Gill, D. O., Barker, D. M., Wang, W., & Powers, J. G. (2005). *A Description of the Advanced Research WRF Version 2*.

Skamarock, W. C., Klemp, J. B., Dudhia, J., Gill, D. O., Barker, D. M., Duda, M. G., et al. (2008). *A Description of the Advanced Research WRF Version 3*.

Skamarock, W. C., Klemp, J. B., Dudhia, J., Gill, D. O., Liu, Z., Berner, J., et al. (2021). *A Description of the Advanced Research WRF Model Version 4*. Retrieved from http://library.ucar.edu/research/publish-technote

Souri, A. H., Choi, Y., Pan, S., Curci, G., Nowlan, C. R., Janz, S. J., et al. (2018). First Top-Down Estimates of Anthropogenic NOx Emissions Using High-Resolution Airborne Remote Sensing Observations. *Journal of Geophysical Research: Atmospheres*, *123*(6), 3269–3284. https://doi.org/10.1002/2017JD028009

Sun, K. (2022). Derivation of Emissions from Satellite-Observed Column Amounts and Its Application to TROPOMI NO2 and CO Observations. *Geophysical Research Letters*, e2022GL101102. https://doi.org/10.1029/2022GL101102

Verstraeten, W. W., Boersma, K. F., Douros, J., Williams, J. E., Eskes, H., Liu, F., et al. (2018). Top-Down NOX Emissions of European Cities Based on the Downwind Plume of Modelled and Space-Borne Tropospheric NO2 Columns. *Sensors*, *18*(9), 2893. https://doi.org/10.3390/s18092893

Wiedinmyer, C., Akagi, S. K., Yokelson, R. J., Emmons, L. K., Al-Saadi, J. A., Orlando, J. J., & Soja, A. J. (2011). The Fire INventory from NCAR (FINN): A high resolution global model to estimate the emissions from open burning. *Geoscientific Model Development*, *4*(3), 625–641. https://doi.org/10.5194/gmd-4-625-2011

# Appendix A. GCAS vs. CAMx daily comparisons

## Sept 1, 2021: Wednesday

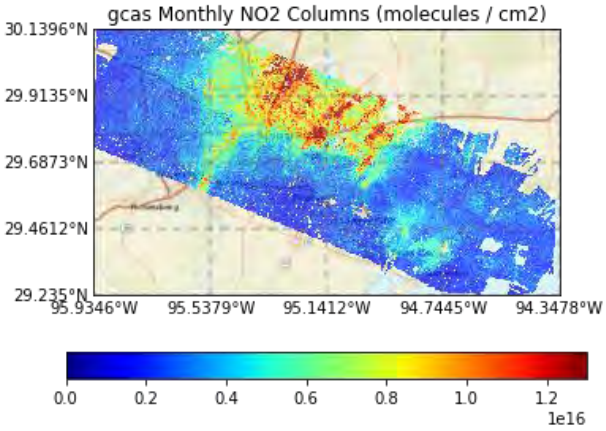


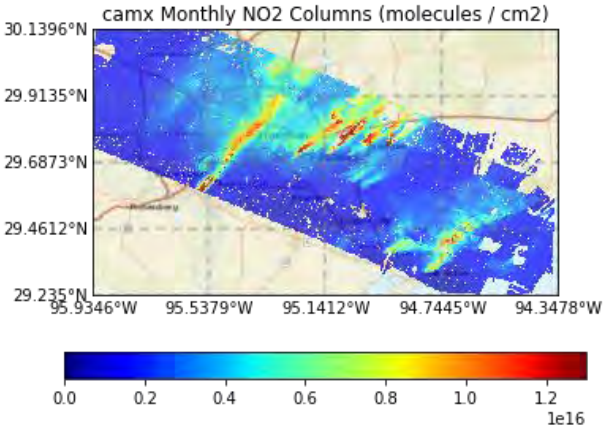


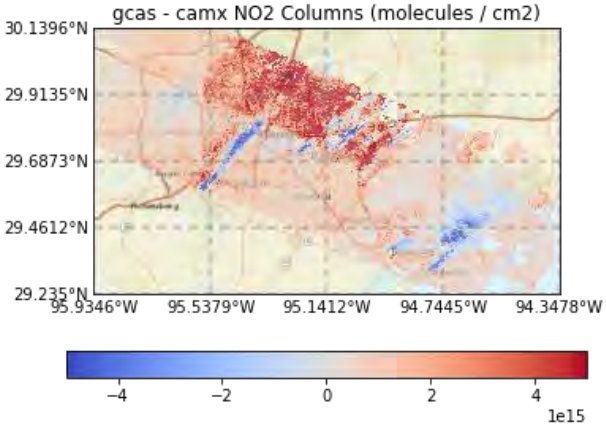


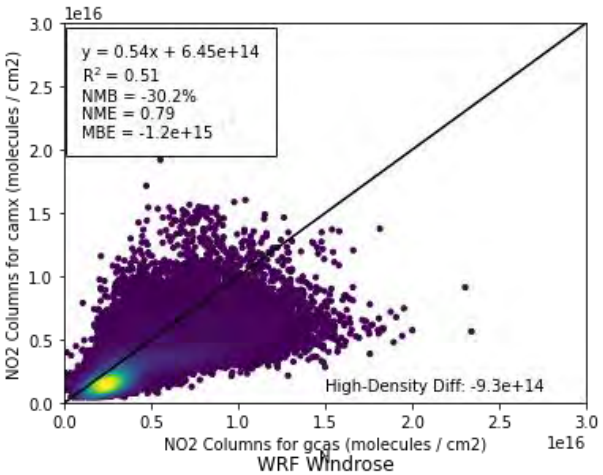


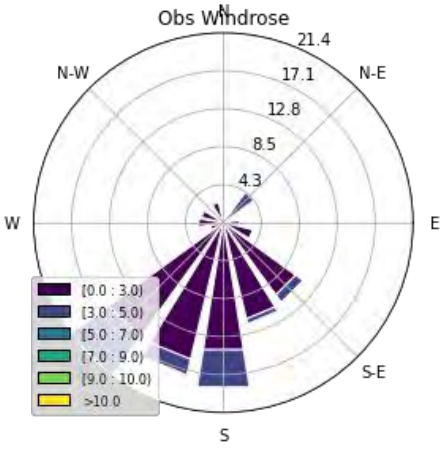


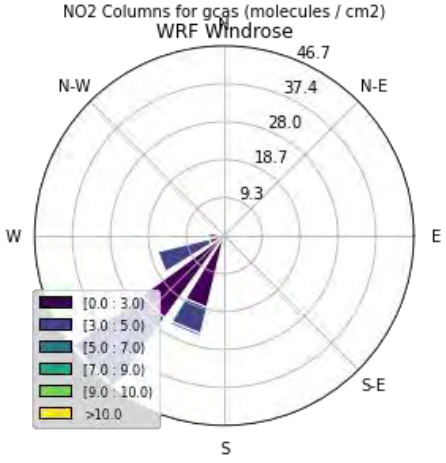

**Sept 3, 2021: Friday**

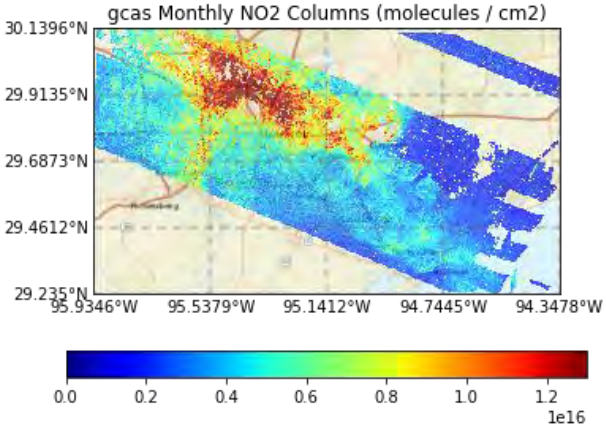


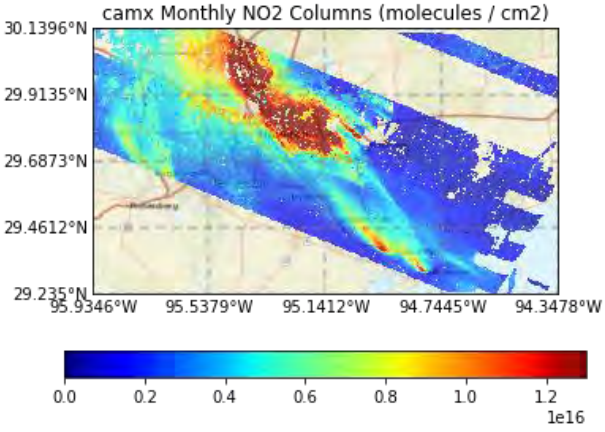


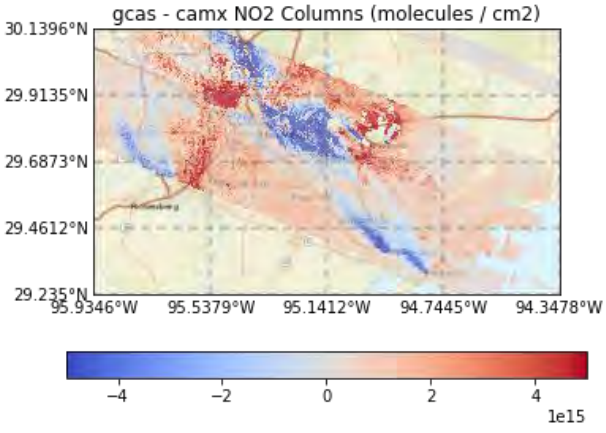


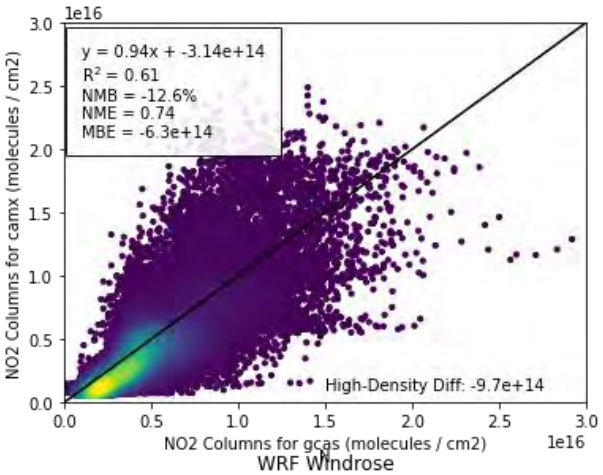


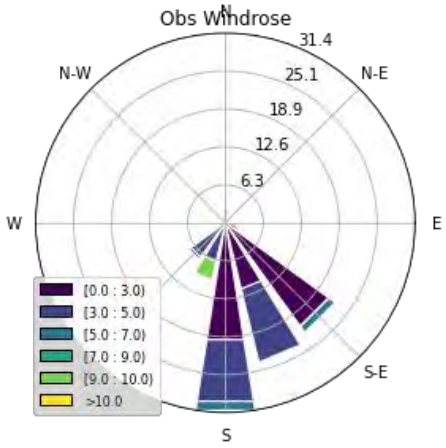


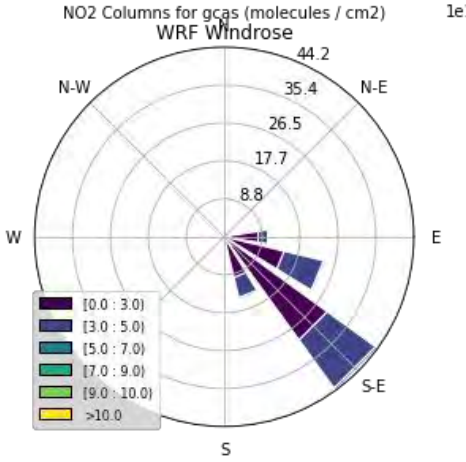

**Sept 8, 2021: Wednesday**

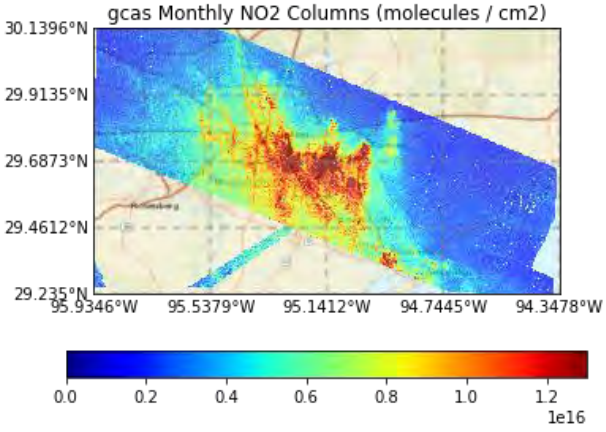


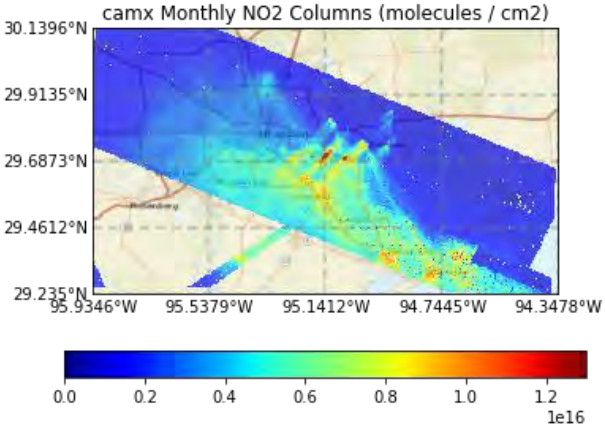


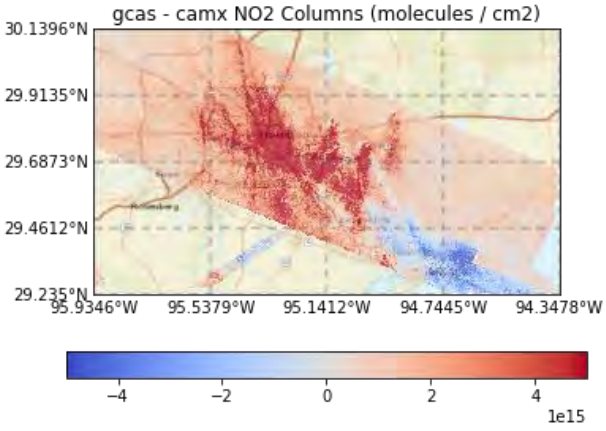


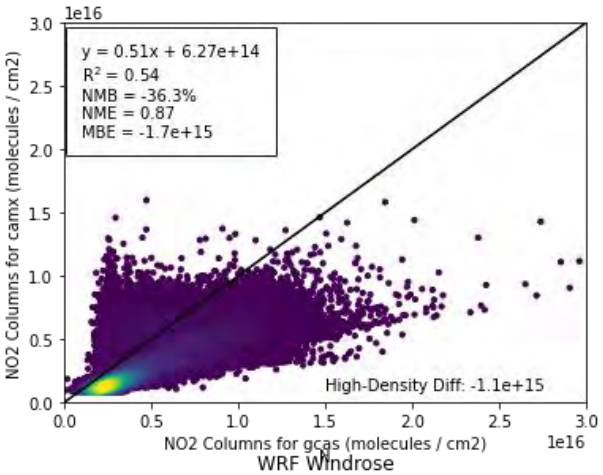


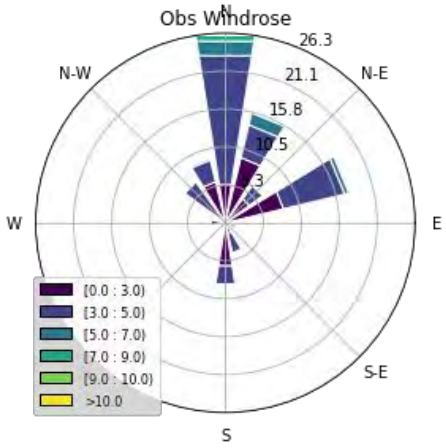


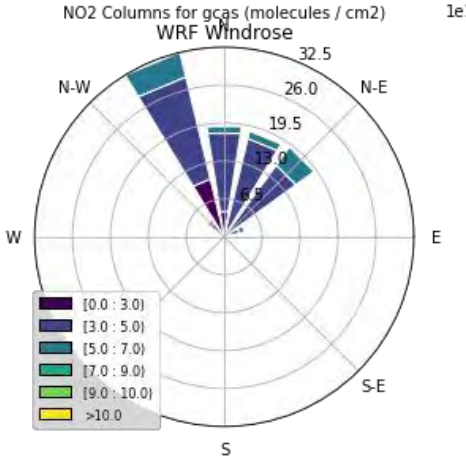

**Sep 9, 2021: Thursday**

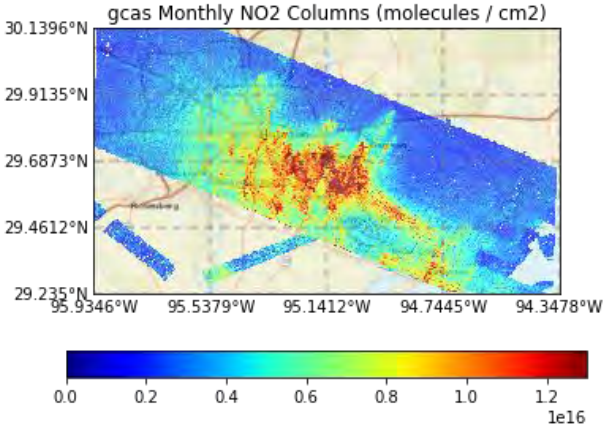


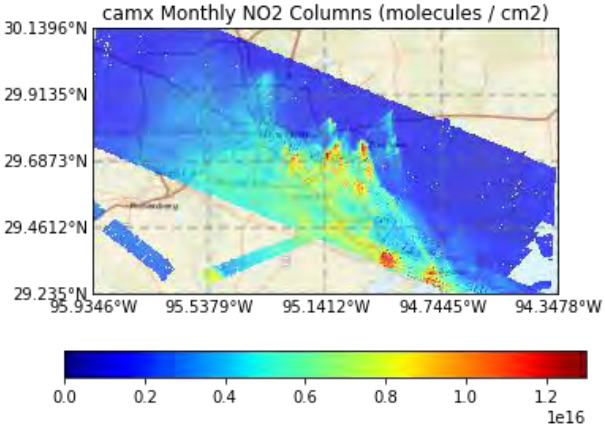


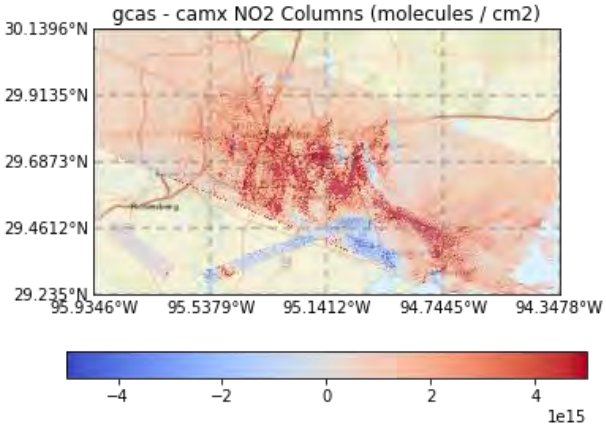


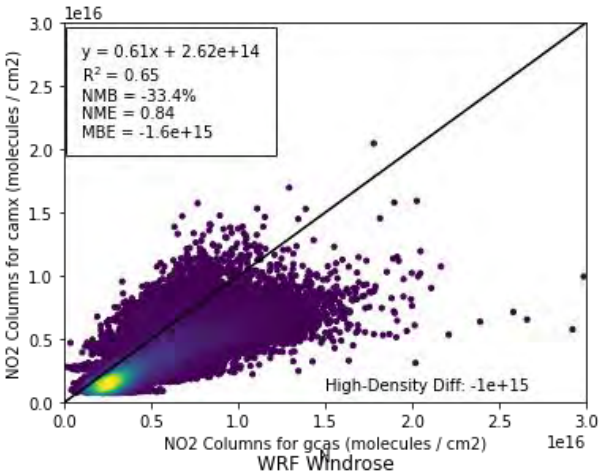


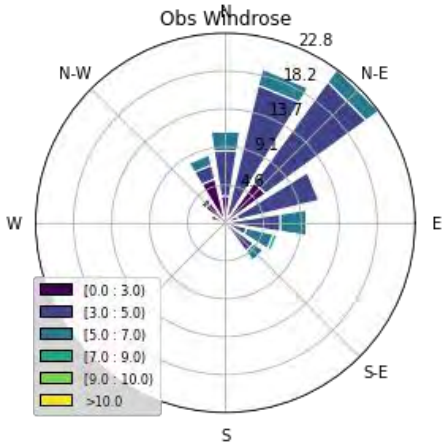


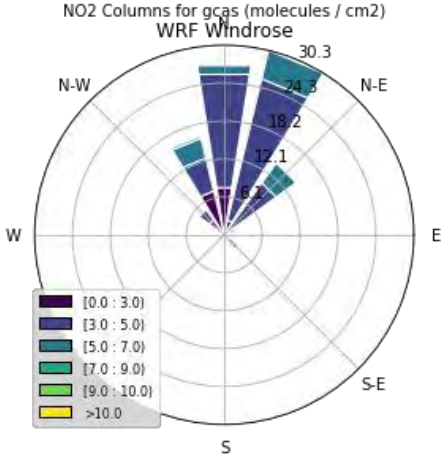

**Sept 10, 2021: Friday**

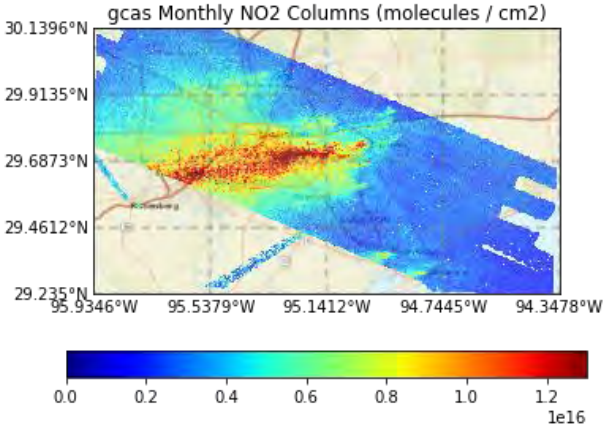


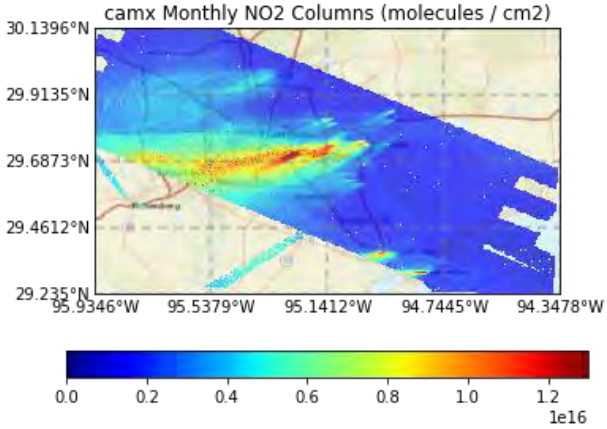


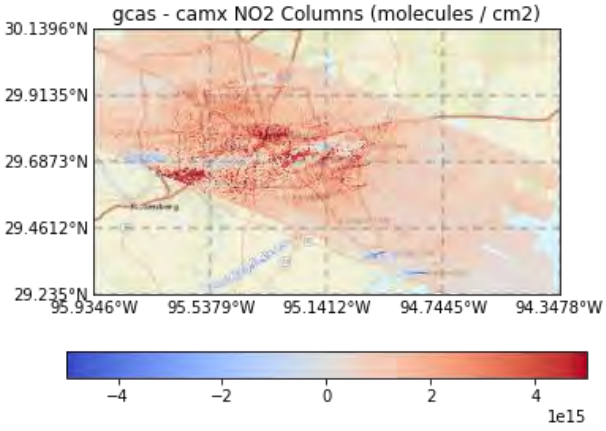


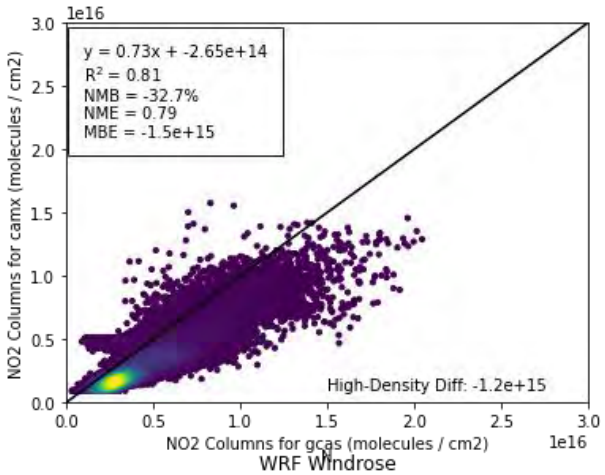


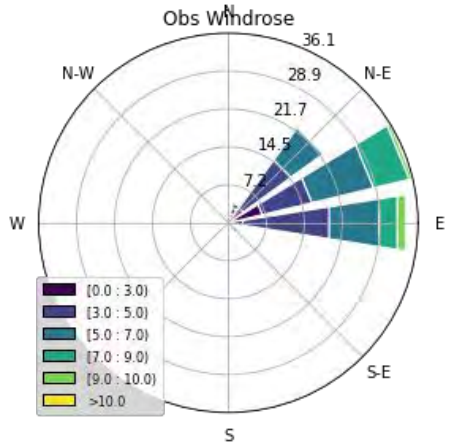


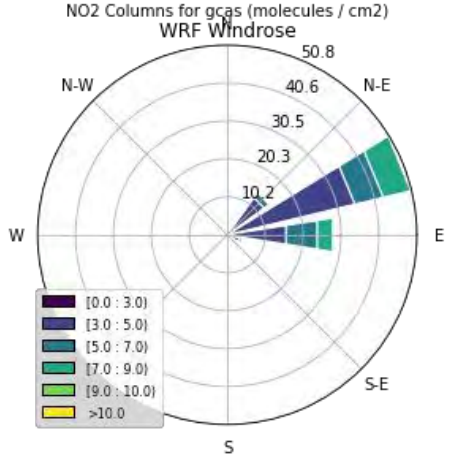

**Sept 11, 2021: Saturday**

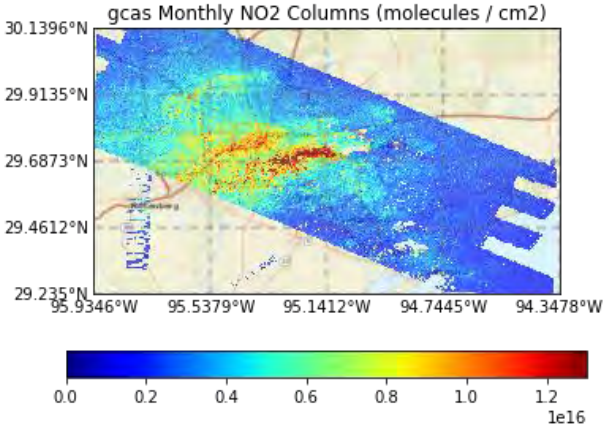


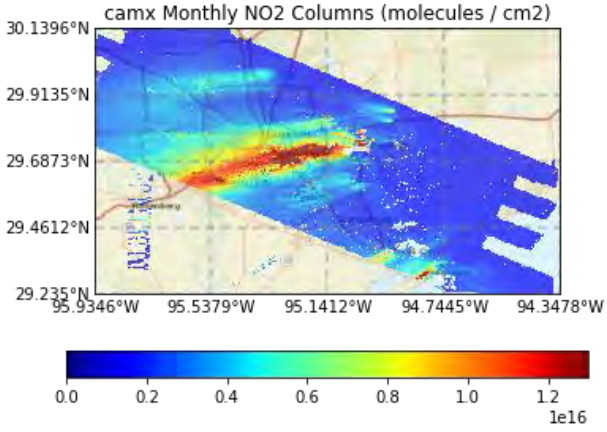


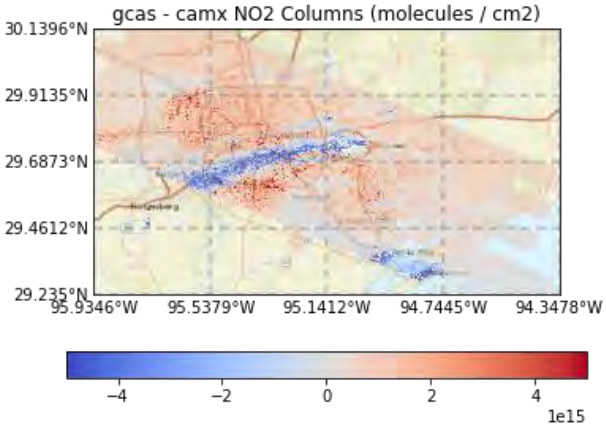


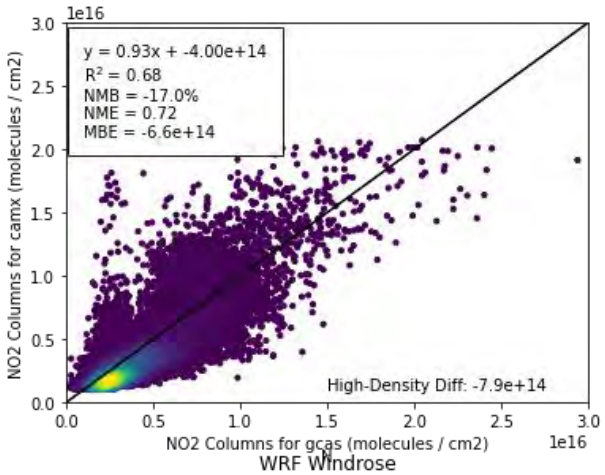


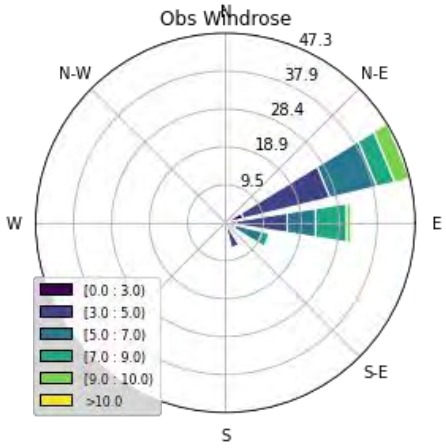


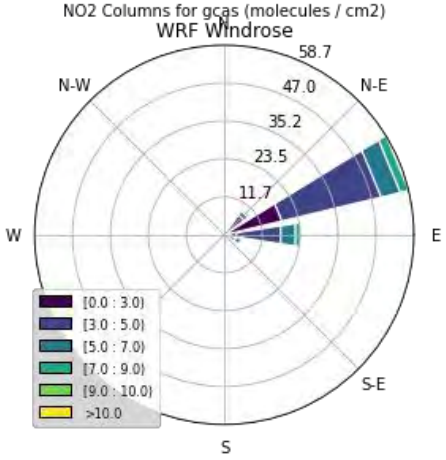

**Sept 23, 2021: Thursday**

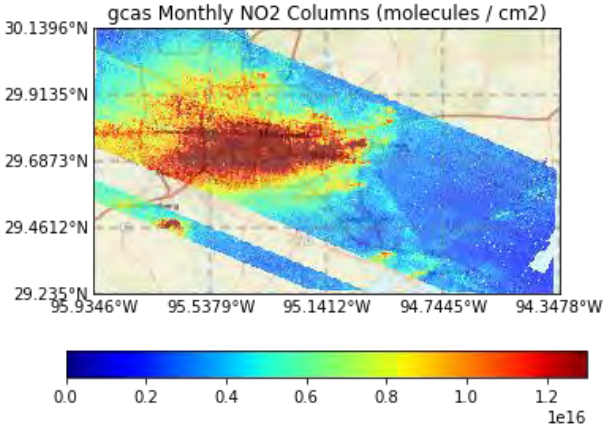


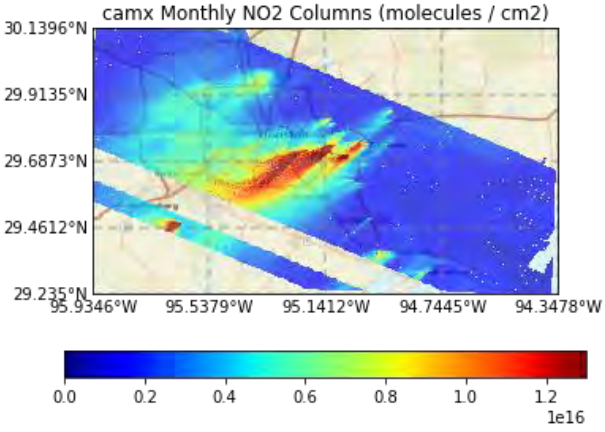


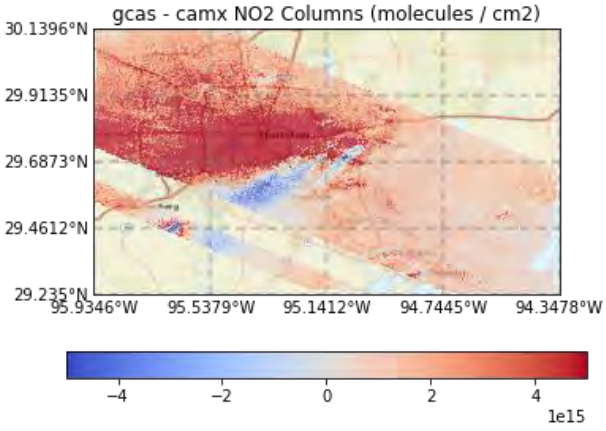


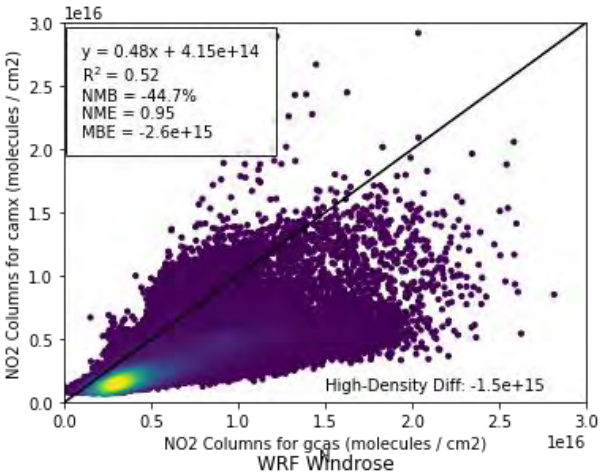


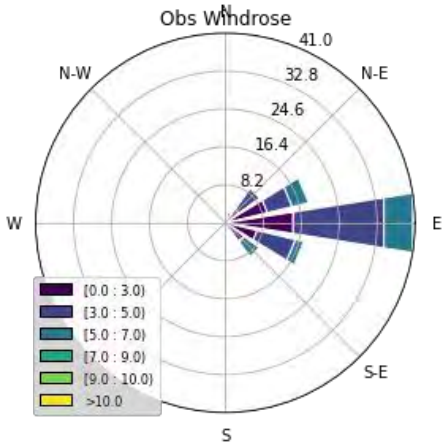


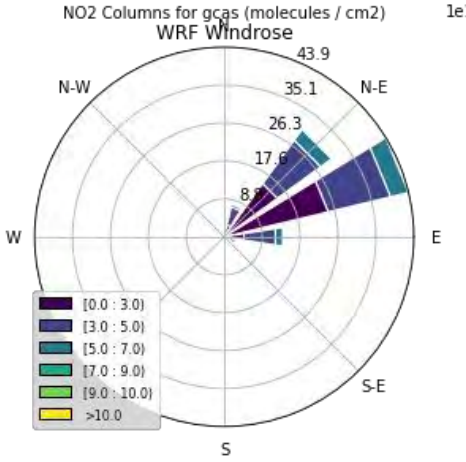

**Sept 24, 2021: Friday**

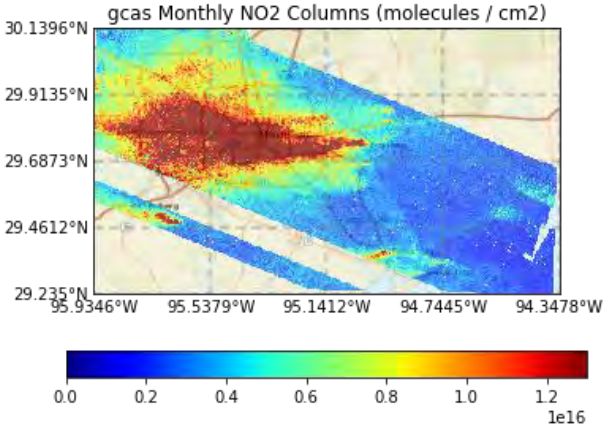


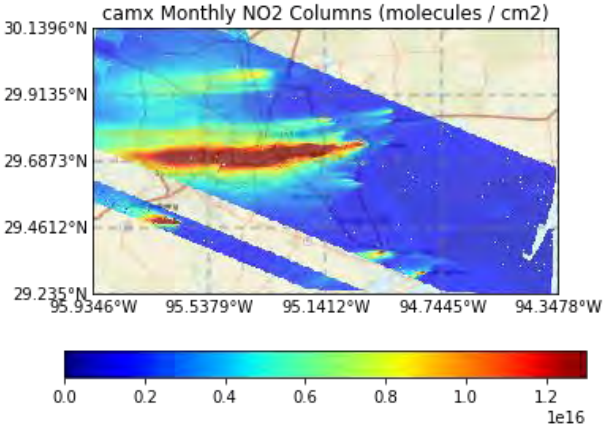


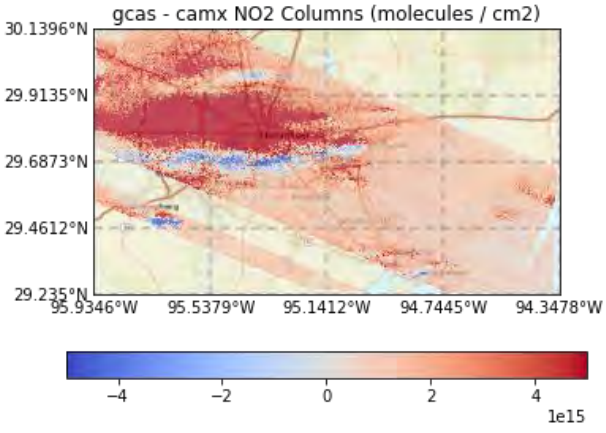


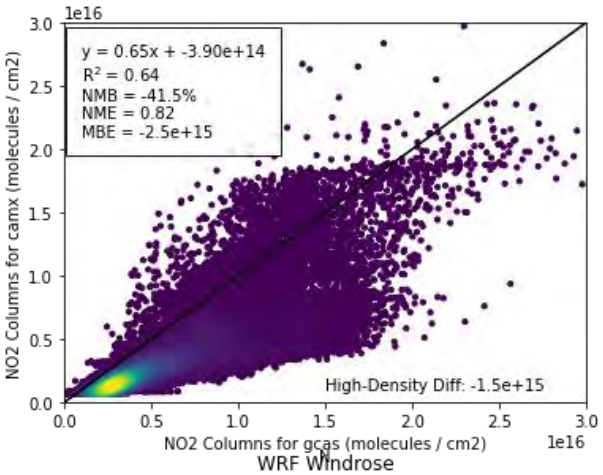


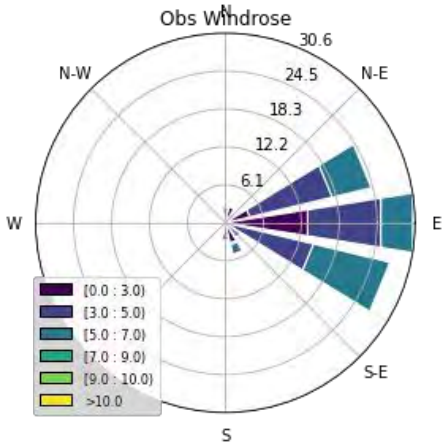


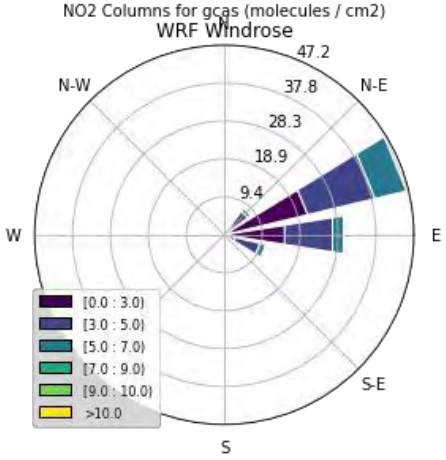

**Sept 25, 2021: Saturday**

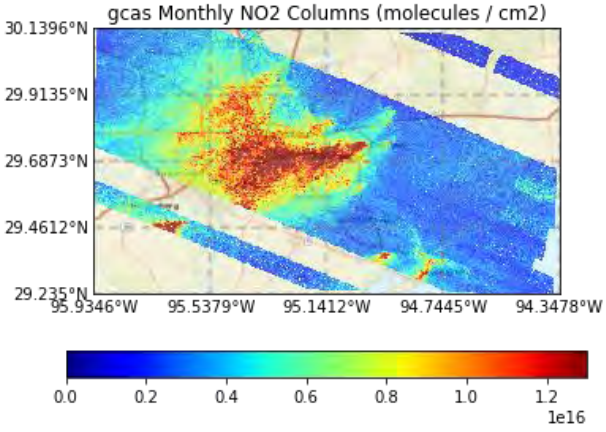


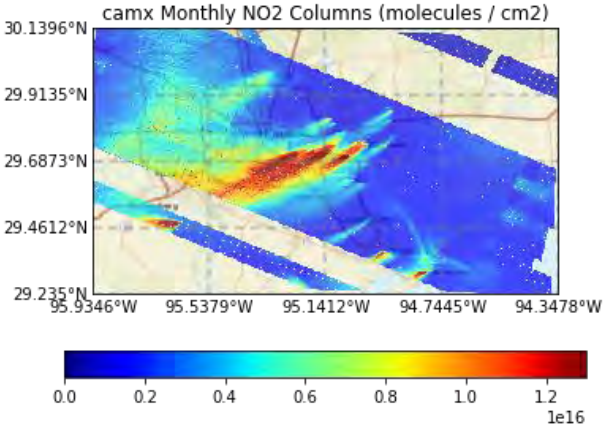


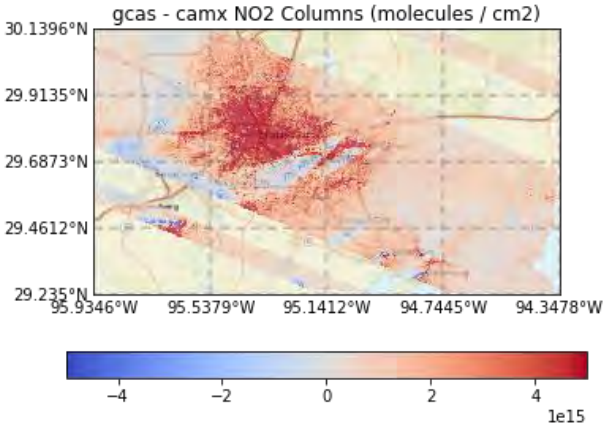


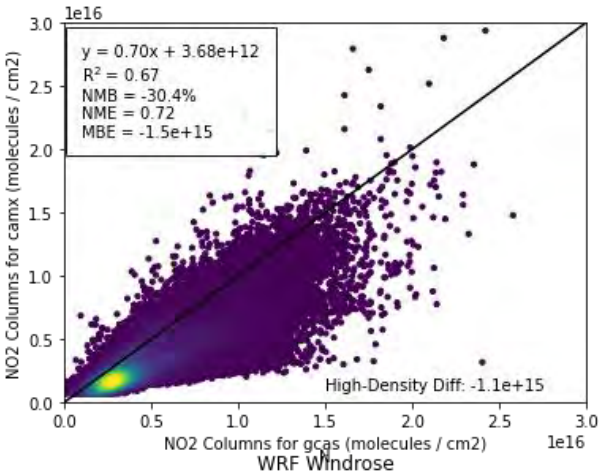


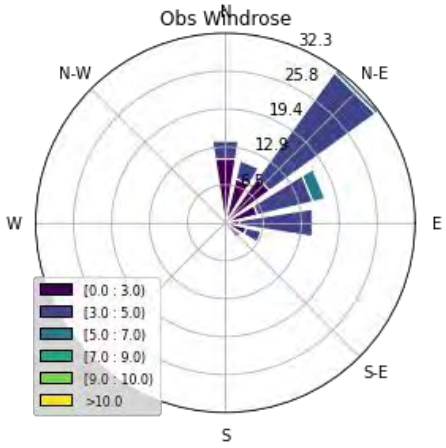


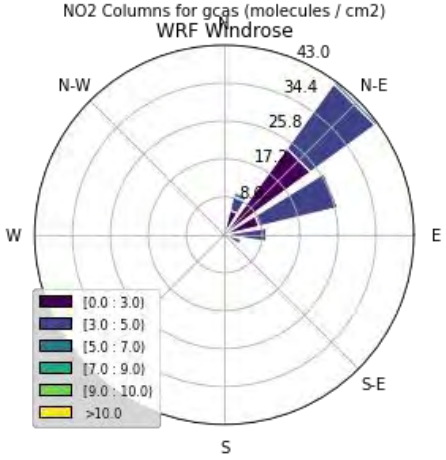

**Sept 26, 2021: Sunday**